On the Role of Zirconium Hydrides and Hydride Rim Features in Causing Low Strain Ruptures in Stress Relieved Zirconium Alloy Cladding Tubes in Pulse Reactor Tests

A Dissertation

Presented in Partial Fulfillment of the Requirements for the

Degree of Doctor of Philosophy

with a

Major in Nuclear Engineering

in the

College of Graduate Studies

University of Idaho

by

David W. Kamerman

Approved by:

Major Professor: Indrajit Charit, Ph.D.

Committee Members: Robert Borrelli, Ph.D.; Matthew Swenson, Ph.D.; Haiyan Zhao, Ph.D.

Department Administrator: Indrajit Charit, Ph.D.

August 2023

Abstract

Stress relieved zirconium alloys are the most widely used material to construct light water reactor fuel cladding tubes. Circumferential zirconium hydride features form in the metal matrix because of waterside corrosion, and at high exposures thick, 'rim' like features form on the cladding outer surface. During transient reactor pulse tests on high exposure fuel rods, they are prone to rupture at low cladding strain via a mechanism that is independent of the boiling crisis that had been previously thought to be required to cause cladding failures in overpower transients. These low strain ruptures are currently the most limiting failure mode for light water reactor fuel in dictating plant safety limits in reactivity-initiated accidents. The objective of this dissertation work is to better quantify the role of circumferential hydrides and hydride rim structures in causing these low strain ruptures. A careful review of the publicly available transient reactor pulse test database showed that the prevalence of these kinds of low strain failures is certainly related to the concentration and distribution of circumferential hydrides in the metal matrix. In pulse tests with the cladding temperature initially at room temperature, low strain cladding failures begin at relatively low cladding hydrogen concentrations of 132 ppm. While the database with initial cladding temperatures in the 250 °C – 280 °C range is significantly more limited, the data points that do exist suggest that this hydrogen threshold increases to at least 400 ppm and is more than likely above 500 ppm.

While it is impossible to replicate all the phenomena that occur in a reactor pulse test in a separate effects test, key features of the test to low strain rupture can be replicated. A review of previous separate effects studies seems to suggest similar hydrogen concentration thresholds only when the tests involve cladding materials with a prototypic hydride rim. A novel way of artificially creating these prototypic hydride structures is developed and described as part of this work. Apart from a prototypic hydride rim, key separate effects test features chosen for study in this work included the ability to create a uniform bi-axial load in the cladding tube that would be strain controlled such that flow stresses during plastic deformation could be determined. This was achieved by measuring the hoop strain in-situ and programming the value into a feedback loop with a high-pressure pneumatic regulator on an internal pressure test. In-situ measurement of the hoop and axial strain during testing with fresh nuclear grade Zircaloy-4 cladding tubes allowed for the determination of Hill yield coefficients and an anisotropic yield loci.

When the strain-controlled pressure tests were conducted on cladding tubes with hydride rims at low cladding temperatures, less than 150 °C, the stress relieved zirconium alloy cladding tubes begin rupturing at very low strain with even modest concentrations of cladding hydrogen, less than

189ppm in the present study. However, at higher temperatures of 150 °C and above cladding ductility is remarkably improved and only cladding tubes with ~500 ppm of hydrogen or higher experience low strain ruptures. Given the low strain rates and lack of irradiation damage in the cladding tubes the recreation of these thresholds in a separate effects test is rather remarkable and confirms that the primary variables effecting cladding rupture are the quantity and distribution of the hydrides, the temperature of the cladding, and the bi-axial nature of the cladding loading path. Another significant finding from the strain-controlled pressure testing is that the hydride rims always fractured at hoop stress levels below that which would have caused cladding yielding in a non hydrided sample. The fracture that forms in the rim region of the cladding tube is a Mode-1 crack that is arrested at the metal hydride interface. Following formation of these Mode-1 cracks in the hydride rim, the bulk stress-strain behavior of the cladding tubes follow a path that is often similar to fresh cladding tubes with a quick hardening shoulder and the nearly perfectly plastic deformation albeit at a typically much lower flow stress. In cladding tubes which are undergoing low temperature deformation at the hoop stress fields and thus stress intensity factors at these crack tips is quite high and is likely causing the formation of circumferential voids on the circumferential hydrides beneath the rim in front of the crack tips. The formation and linkage of these voids to the primary mode-I crack and each other via 45° shear bands in the metal between the hydrides causes a zig-zag pattern of fracture at low overall cladding hoop strain. Above 150 °C no evidence of these circumferential voids is seen and the cladding tubes which rupture at low overall hoop strain only do so when a very large Mode-I crack is formed in a very thick hydride rim or blister and the stress intensity factors are sufficiently high in this region to propagate the crack through the thickness by a ductile shearing mechanism alone.

Acknowledgments

Dedication

This dissertation is dedicated to my daughters Chloe and Addison. May your curiosity and sense of wonder be surpassed only by your kindness and compassion. May you always look at the world before you and challenge what you see and be ready to learn from every experience life brings you.

Table of Contents

List of Tables

List of Figures

Statement of Contribution

This dissertation includes material from three co-authored publications. The author of this dissertation is the lead author in each publication and bore the primary intellectual contribution in each case. In "*A review of cladding failure thresholds in RIA conditions based on transient reactor test data and the need for continued testing*" co-authers Colby Jensen, Charles Folsom, Nicolas Woolstenhulme, and Daniel Wachs provided technical review and participated in discussions on the interpretation of test results from the reviewed literature sources. In *"Multi-Axial Plastic Deformation of Zircaloy-4 Nuclear Fuel Cladding Tubes"* co-author Malachi Nelson helped to conduct some of the internal pressure tests and performed a peer review and technical check of the calculations performed. In *"Formation and Characterization of Hydride Rim Structures in Zircaloy-4 Nuclear Fuel Cladding"* coauthors Mukesh Bachhav, Tiankai Yao, Xiaofei Pu, and Jatuporn Burns performed some of the microstructural characterization reported with provided direction from the lead author of the study and this dissertation.

Chapter 1: Introduction

1.1   Dissertation Objectives and Structure

The objective of this dissertation work is to better quantify the role of circumferential hydrides and hydride rims, which form in stress relieved Zircaloy-4 nuclear fuel cladding tubes during service in light water reactors, in causing low strain cladding ruptures prior to the boiling crisis during transient pulse reactor tests.

This dissertation is organized in a paper format and contains four separate manuscripts which are complete individual studies which seek to address part of the above stated objective. These studies are presented in their complete and unaltered form in Chapter 2, Chapter 3, Chapter 4, and Chapter 5. A comprehensive background section on the motivation for pulse reactor testing and the properties of zirconium alloy cladding materials is included in this chapter in the subsequent section headings. Smaller background and introduction sections at the beginning of each paper restate parts of this material most relevant to those manuscripts.

Important new insights into the role of circumferential hydrides and hydride rims in causing low strain cladding ruptures are presented in this work. Pulse reactor tests are very complex and impossible to replicate in laboratory conditions. The author has carefully studied the available public database of pulse reactor tests particularly those where low strain ruptures occur and surveyed many of the previous separate effects test intended to replicate them and presented this review in *Chapter 2: A review of cladding failure thresholds in RIA conditions based on transient reactor test data and the need for continued testing*. The author then decided on the most important aspects of the pulse test to replicate a simple yet novel pressure test stand is described and validated in *Chapter 3: Multi-Axial Plastic Deformation of Zircaloy-4 Nuclear Fuel Cladding Tubes*. The ability to recreate representative circumferential hydride rim structures through a novel method is described in *Chapter 4: Formation and Characterization of Hydride Rim Structures in Zircaloy-4 Nuclear Fuel Cladding Tubes*. Finally, a systematic series of tests using the novel pressure test stand with zirconium alloy cladding tubes containing the representative circumferential hydride rim features is presented in *Chapter 5: The Deformation and Burst Behavior of Zircaloy-4 Cladding Tubes with Hydride Rim Features Subject to Internal Pressure Loads.* Concluding this dissertation is a brief chapter drawing some conclusions from the integration of the four separate studies and describing opportunities for future research in this area.

1.2   The Motivation for Pulse Reactor Testing

Pulse reactor tests have been conducted since the beginning of the nuclear era. The principal aim of such tests has been and continues to be the development of safety criteria which can be used to govern the design and operation of nuclear power systems. In November of 1993 during a transient reactor test at the CABRI reactor in Caderache, France, it was discovered that fuel cladding ruptures could occur independently from the boiling crisis at low temperature (< 300 °C and at much lower peak enthalpies than had been observed previously [1]). Previous tests on LWR fuel had generally shown that the fuel rods failed due to either oxidation or high temperature bursting due to the boiling crisis in the surrounding light water coolant [2]. The CABRI test was unique in that it was conducted with a light water reactor (LWR) fuel rod, but the test environment was that of flowing sodium at 280 °C and 0.3MPa. The sodium environment of the CABRI test would preclude a boiling crisis from occurring. Upon completion of the test, it was discovered that the test rod (CABRI RepNa-1) experienced a dramatic cladding rupture early in the power excursion. The result shocked the nuclear power community at the time and has motivated many subsequent research endeavors as well as the development of new and generally more conservative safety criteria to be applied to the analysis of overpower transient safety analysis.

1.2.1 Reactor Design and Safety Criteria

Design and safety criteria for nuclear reactors and nuclear reactor control systems can be derived from how the reactor responds to unintended changes in its reactivity and/or unintended disruptions to its coolant supply. These disruptions are generally referred to as reactor transients. The most fundamental idea in the development of reactor design or nuclear safety criteria is that the consequences of postulated events (transients) should be inversely proportional to the probability of those events [3]. During transients with higher probabilities, typical of operating nuclear power plants, safety criteria generally allow for no increase in the release of radioactive material. This is achieved by requiring that no damage to the reactor's fuel take place. For events with lower probabilities some release of radioactive material is tolerated provided it has minimum impact on the environment and general public safety. The Nuclear Regulatory Commission standard review plan (SRP) codifies this philosophy through the establishment of generally accepted safety criteria for the nuclear fuel system found in NUREG 0800 chapter 4.2 [4]. This standard review plan establishes four objectives for fuel safety criteria which are to ensure that:

1. The nuclear fuel system is not damaged as part of normal operations including anticipated transients.

2. The fuel system damage is never so severe as to prevent control rod insertion when it is required.
3. The number of fuel rod failures is not underestimated.
4. Coolability is always maintained.

The first objective that the fuel system is not damaged as the result of normal operations and anticipated transients stems from General Design Criterion (GDC) 10, within Appendix A to 10 CFR Part 50 which requires that the reactors be designed to prevent fuel damage in both normal operations and anticipated transients. In this context "not damaged" means that the fuel rods do not fail, that the fuel system dimensions remain within operational tolerances, and that the functional capabilities of the fuel system are not reduced below those assumed in the safety analysis. Objectives (2) and (4) stem from requirements in 10 CFR Part 50 Appendix A, GDC 27 and 35 for the reactivity control system (RCS) and emergency core cooling system (ECCS), respectively. GDC 27 requires that the RCS be designed to be capable of controlling reactivity in postulated accidents. GDC 35 requires that the ECCS be capable of transferring heat from the reactor core following a loss of active cooling. In this context, "coolability" means that the fuel assembly retains a rod bundle like geometry with adequate cooling channels to permit removal of residual heat.

The limiting low probability events plant designers must consider are referred to as design basis accidents (DBAs). In DBAs some damage to the reactor core and nuclear fuel is expected as part of the accident sequence. Objective (3) stems from requirements in 10 CFR Part 50.67 and Part 100 which require dose consequence analysis for all DBAs. Thus, the release fraction from failed fuel must be accounted for in those scenarios. In this context, "fuel failure" is defined as a loss in fuel rod hermeticity or fuel rod cladding breach. It is worth noting that it is not required that all fuel failures be prevented, even in normal operations. Indeed, the presence of cleanup systems in nuclear power plant designs presume that a small number of leaking rods may exist from time to time. However, to meet the requirements of GDC 10 (Objective 1) and to support dose consequence analysis as part of DBAs (Objective 3), the SRP states that fuel failure criteria should be provided for all known fuel rod failure mechanisms. These criteria are used to demonstrate the "no damage" requirement in normal operations and Anticipated Operational Occurrences (AOOs) and to meet the dose consequence requirement in DBAs. Thus, to meet these four objectives, fuel safety criteria are generally identified at three damage levels. These levels include (1) fuel damage criteria, (2) fuel failure criteria, and (3) fuel coolability criteria.

1.2.2 Behavior of Light Water Reactor Fuel in Overpower Transients

Reactivity initiated accidents (RIA) are a class of DBA that occur as the result of a sudden increase in the reactor's reactivity due to sudden changes in the core configuration resulting in a scenario where the reactor is no longer reliant on delayed neutrons to maintain a 1:1 criticality ratio. In PWRs, the design basis RIA is the control rod ejection accident (CREA). In BWRs the design basis RIA accident is the control rod drop accident (CRDA). In both cases, the transient is most severe when the reactor is at a zero-power condition. CREAs and CRDAs result in the insertion of reactivity, as the reactor core is no longer dependent on the delayed neutrons to maintain its criticality ratio. These transients send the reactor on a rapid positive power period; however, the transient is terminated as the fuel heats up. As the uranium atoms in the fuel increase in temperature they are more likely to absorb or scatter the neutrons than to experience fission. This effect is known as doppler broadening in the fuel and results in a rapid decrease in reactivity. The resulting power pulse is nominally Gaussian in shape, the width of which can be characterized by a full width at half maximum (FWHM) or pulse width. For PWRs at hot coolant conditions and zero or low reactor power (such as the case just prior to startup), termed hot zero power (HZP), pulse widths range from 20 – 65 milliseconds (ms). For BWRs at cold zero power (CZP), the pulse widths range from 45 – 80 ms. The prompt part of the transient is followed by a decaying exponential tail which is the result of delayed neutron fissions. The point which divides the prompt Gaussian phase from the later decaying exponential phase of the transient is generally taken as one FWHM past peak power. Nuclear fuel safety criteria in RIAs must be established to ensure that radiological releases from failed fuel elements are quantified and that the nuclear fuel maintains a geometry that is amenable to long term cooling to limit the amount of long-term exposure and release of radioactive material. Fuel failure criteria need to be established to determine the conditions upon which hermiticity of the fuel rods can no longer be maintained, and fuel coolability criteria need to be established to preclude events such as reactor coolant channel blockage, fuel rod fragmentation, fuel cladding embrittlement, damage to the reactor system pressure boundary and/or generalized fuel melting [5].

For RIAs, safety criteria have historically been expressed as limits on the peak radial average enthalpy of the fuel pins. The energy released during the transient is initially deposited into the reactor's fuel and then subsequently transferred to the reactor cooling system. In LWR design basis RIAs, the rate of energy injection in the fuel can be much greater than the thermal response time of the fuel. Initially, the heat up in the fuel is so rapid that it happens nearly adiabatically with little sensitivity to the fuel's thermal conductivity or the cladding coolant heat transfer coefficient. In this early part of the transient, the fuel's enthalpy rise is nearly equivalent to the energy deposited in the

fuel. However, as the power level in the transient begins to decrease and heat begins to be transferred from the fuel to the environment, the enthalpy increase in the fuel begins to diverge from the total energy deposited and, eventually, the fuel enthalpy begins to decrease as shown in Figure 1-1. These conditions can most closely be replicated in transient reactor pulse tests. These tests are used to develop the safety criteria for light water reactor fuel pins in RIA transients.
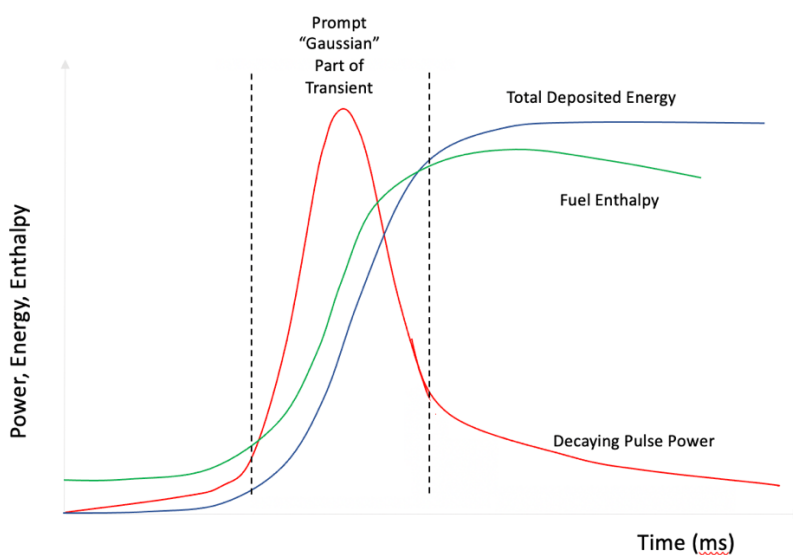
Figure 1-1 LWR Fuel Rod Power, Energy, and Enthalpy Response during an RIA Transient.

1.3 Properties and Characteristics of Zirconium Alloy Fuel Cladding Tubes

To better understand and determine the mechanistic conditions which lead to early failure of high burnup LWR fuel rods in pulse reactor tests it is necessary to develop an understanding of the zirconium alloys which make up the fuel cladding as well as their principal in service degradation modes. Zirconium alloys have been widely adopted in the nuclear power industry, principally due to their low neutron absorption cross section (0.18 barns). Their primary usage is as nuclear fuel cladding tubes, however other structural components in the reactor also make use of zirconium alloy materials. Apart from their neutronic properties the two most important features of these materials which have driven their alloy design for their use in light water reactors (LWRs) are their mechanical strength and their corrosion resistance.

Zirconium alloys can be generally divided into three categories. The first being the zirconium plus tin series also commonly referred to as the Zircaloys, developed mostly in the United States. The

second is the zirconium plus niobium series which underwent initial development in Canada and the USSR. The third being quaternary alloys which incorporate both tin and niobium with lower oxygen concentrations chiefly developed by the Westinghouse Electric Corporation with the trademark of Zirlo[TM] [6]. All three classes of alloys contain some small amounts iron, chromium, oxygen, hydrogen, nitrogen, sulfur, and in some cases nickel. The impact of the metallurgical fabrication methods and alloy composition have significant effects on both the mechanical properties and the corrosion resistance to water and steam. Zirconium has a hexagonal close packed (HCP) crystal structure at room temperature making it relatively unique compared to other structural materials which typically have face centered cubic (FCC) or body centered cubic structures (BCC). This room temperature phase of zirconium is referred to as the alpha (α) phase. At 865°C zirconium undergoes an allomorphic phase transformation to a BCC crystal structure known as the beta (β) phase. The metal retains this structure up to its melting point of 1860°C. In the room temperature HCP phase, the metal has a near ideal c/a ratio of 1.593. The room temperature lattice constants of a=0.323nm and c=0.515nm. The HCP structure leads to anisotropy in the grain's modulus and thermal expansion constants. For polycrystalline materials these values are typically around 96 GPa and $5.2 * 10^{-6}$ e-6 K^{-1} at room temperature [7].

Oxygen, nitrogen, and tin are all highly soluble in the α-phase of zirconium and occupy octahedral interstitial sites in the crystal lattice. Oxygen is added in low concentrations as an alloying element to solution strengthen the alloy. Nitrogen and carbon can also solution strengthen the alloy, but they have an extremely penalizing effect on the alloy's corrosion resistance, so their concentration is minimized as much as possible. Tin (Sn) is added in low concentrations to counter the effect of nitrogen and carbon on the corrosion properties. These elements have the effect of stabilizing the α-phase at high temperatures and increasing the phase transition temperature as their concentration in the metal increases. When oxygen is present in β-zirconium at high concentrations it has the tendency to precipitate out as a new oxygen saturated α-Zr phase and with increasing concentration transforms to one of several zirconium-oxide phases.

The elements of iron, chromium, and nickel were initially added inadvertently due to a contamination of zirconium with stainless steel [8]. These elements all have low solubility in α-Zr and generally exist as precipitates with a $Zr(Fe,Cr,Ni)_2$ structure. In low concentrations these precipitates aid in both the mechanical and corrosion properties of the alloy. They have the effect of decreasing the α-β phase transition temperature with increasing concentrations. Niobium likewise has limited solubility in α-Zr. In most Zr-Nb alloys, the niobium tends to segregate to the grain

boundaries. There it initially precipitates out as new β-Zr grains with a high Nb content. These grains further decompose into α-Zr and a BCC niobium crystal called β-Nb. As with Fe, Cr, and Ni, these Nb precipitates have both strengthening and corrosion resistance properties [7].

1.3.1 Deformation Behavior

Deformation of α-Zr happens as result of both slip and twinning. Because of the HCP crystal structure, the number of slip systems is more limited than in FCC or BCP metals. Slip happens primarily in the [$\bar{2}110$] direction on the prism planes {$01\bar{1}0$}, and to a lesser extent basal planes {0001}, and first order pyramidal planes {$0\bar{1}11$}. An example of this primary slip system on the prism plane is shown below in Figure 1-2. Slip on this primary system is easily activated and high deformation rates can be achieved at low stress. Slip in the <c> direction can be accomplished on second order pyramidal planes such as {$11\bar{2}1$} in the [$\bar{2}113$] direction. Slip with a <c> direction component requires both high stresses and high temperatures for these slip systems to activate. Deformation in the <c> direction can also be accomplished as the result of twinning. Under tensile load, twin boundaries are formed with the basal poles of the twinned region being rotated 35° and/or 85° from the original crystal. Under compressive loads twin boundaries with 57° and 64° angles are formed. Other higher order slip systems can be activated at higher temperature, most of these are diffusion activated or controlled systems giving most zirconium alloys significant creep properties at higher temperature. Slip results in small grain rotations even at high deformation, although significant flattening of the otherwise equiaxed grains can occur. Slip on the basal planes results in the rotation of the basal pole about its axis but does not change its orientation [8]. As opposed to slip, twinning results in large crystal rotations even at small deformations. New crystallographic orientations in the twinned regions allow primary slip systems to activate due to the orientation change. The result of these deformation modes is that during the forming of the material the basal poles become aligned to the direction of greatest compressive stress. [9].
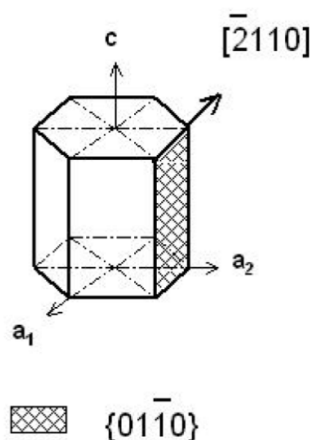
Figure 1-2 Primary Prism Slip in a Zirconium HCP Crystal [9].

A series of cold working and annealing steps are employed during the manufacture of cladding tubes to reduce the thickness and diameter to that of the nuclear fuel cladding (outer diameter 9.5mm, wall thickness 0.57mm). If the final reduction steps are sequenced such as to primarily reduce the tube diameter and maintain the wall thickness, compressive stresses are applied principally in the hoop direction resulting in a grain texture with basal poles aligned circumferentially around the cladding. If, however the final reduction principally reduces the wall thickness and leaves the diameter mostly constant, then the basal poles will align themselves in the radial direction. The latter is what is typically employed in most tubes that will be used as nuclear fuel cladding [10]. The consequences of the final cold working steps on the texture is shown below in Figure 1-3.
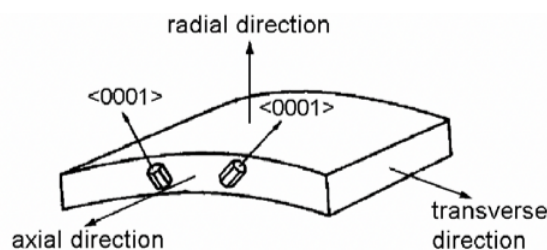
Figure 1-3 Texture in a Cold Rolled Zirconium Alloy Tube [10].

The resulting microstructure from the numerous cold working and annealing steps is one of pancake shaped grains extending axially and circumferentially around the cladding tube with basal planes preferentially oriented +/-30° off the radial direction. This resulting structure is strongly anisotropic and is strongest in the radial direction and weakest in the axial direction. In this way the

cladding tubes resist wall thinning during deformation. In response to an internal pressure load, the cladding seeks to deform in the hoop direction by axial material flow shortening the cladding tube [11]. Bi-axial loading with tensile stress in both the hoop and axial directions causes the primary slip systems to compete and thus very high stresses are seen prior to yield [12]. This same mechanism however results in low ductility when biaxial loads are experienced at low temperature and at high deformation rates [13] when higher order slip systems or twinning is not activated. Biaxial loading on zirconium alloy cladding tubes can be applied by interaction with a rapidly thermally expanding pellet such as in the case of RIA transients with previously irradiated fuel where the pellet and cladding have come into intimate contact prior to the transient. Additional embrittling features such as irradiation damage and waterside corrosion will further reduce the ductility of the cladding making it even more vulnerable to failures in RIAs.

1.3.2 Irradiation Damage

While the cross sections for zirconium interaction with fast neutrons is low these interactions do occur in an LWR environment where the neutron flux is substantial. Accounting for the interaction cross section, the displacement energy and transfer energy of zirconium, Shishov et al [14] evaluated that the damage rate of in zirconium metal to be 1 displacement per atom (dpa) for $6 * 10^{24}$ neutrons per meter squared with energy greater than 1 MeV. The average fast flux in a PWR is $5 * 10^{17}$ n/m^2-s leading to a damage rate of 2-2.5 dpa per year. Molecular dynamic simulations show that a displacement cascade results in an initial core of vacancies with a halo of self-interstitials. At ~320°C (approximate cladding temperature in LWRs) about 20% of these defects survive after the recombination phase [15]. The surviving vacancies have a lower rate of diffusion than the surviving interstitials. Additionally, while diffusion of vacancies in zirconium is isotropic, computational simulations have shown that diffusion of interstitials is strongly anisotropic with diffusion occurring at much higher rates in the basal <c> plane of the metal. This phenomenon is referred to as diffusion anisotropy difference (DAD) [16]. This is a notable distinction from FCC or BCC metals where SIAs are biased toward edge dislocations and grain boundaries are neutral sinks. As SIAs preferentially migrate toward the prism grain boundaries dislocation loops begin forming on the grain boundary surfaces. These <a> loops are the dominant microstructural feature occurring from irradiation damage up to fast fluence levels of 5e25 n/m^2 (~10dpa) for irradiations occurring between 250 C and 400 C [17]. The diameter of these loops is between 5 nm to 20 nm and they have a density of 5e21 m^{-3} and 5e22 m^{-3}. Above 5e25 n/m^2 (10 dpa) vacancy loops begin to appear on the basal plane. These vacancy <c> loops are larger than their <a> loop cousins with diameters of 120 nm but have lower densities 6e20 m^{-3}. The formation of vacancy loops is not intuitive as these edge dislocations are typically

annihilated by migrating SIAs. However, due to the DAD phenomena in zirconium these loops can nucleate in the basal planes as migration of SIAs in the <c> direction is low [18]. The formation of interstitial loops on prism planes and vacancy loops on basal planes explains the irradiation growth phenomena that occurs in zirconium metals. Irradiation growth is a volume conserving deformation where cladding tubes grow in the axial direction and shrink in the radial direction [19].

The accumulated irradiation damage increases the yield stress of zirconium metals and lowers the metal's ductility. These changes in mechanical properties are known to occur and then saturate relatively early during irradiation. The presence of <a> loops in prism planes initially decreases dislocation motion along this primary slip system until stress are reach appreciably high levels. Initial dislocation motion along the prism plane will sweep the <a> loops all at once making subsequent dislocation motion much easier. The dislocation channels that form following the sweeping of <a> loops lead to high yielding in these areas and rapid void nucleation and subsequent ductile failure. While the failure mode is ductile the highly localized nature of these failures in irradiated zirconium metal results in very low uniform elongation often less than 1% at room temperature [20]. Irradiation damage also affects the precipitate structure in zirconium alloys. The $Zr(FeCr)_2$ precipitates amorphize at very low fluences and the neutron damage has the tendency to accelerate Nb precipitation in the metal matrix [21]. The irradiation damage is also known to minimize the extent of the anisotropy between the axial and hoop loading directions with uniaxial tensile data from axial and ring tension tests providing more similar yield and tensile data due to a buildup of <a> loops on prism planes. While difficult to determine experimentally, it is theorized that yield and tensile properties in the radial (through thickness) direction remains notably higher especially at low temperature as irradiation damage is not known to alter or shift the grain orientations.

1.3.3 Waterside Corrosion; Hydrogen Pickup and Embrittlement

In addition to material degradation through irradiation damage, the zirconium metal cladding experiences environmental degradation through waterside corrosion during its service in LWRs. Zirconium reacts with the water in the aqueous coolant according to the following reaction:

$$Zr + 2H_2O \rightarrow ZrO_2 + 2H_2 \tag{1.1}$$

The process results in the formation of a dense oxide layer on the outer surface of the material in contact with the aqueous environment. This oxide is the tetragonal form and is initially adherent to the outer surface. The different density of the oxide and metal results in a pilling-bedworth ratio of 1.56 putting the oxide phase in a compressive stress state upon formation. For these reasons the oxide layer is protective and has the effect of slowing of further oxidation as it grows. Subsequent oxidation

is diffusion-controlled that takes place on the metal oxide interface. The water molecules first must dissociate on the surface of the oxide and then the oxygen atoms must diffuse through the oxide to the metal interface. The dissociation of the water molecules is accomplished from electron diffusion from the oxidation reaction and electron migration to the oxide surface. These processes are shown schematically in Figure 1-4. It is generally accepted that oxygen diffusion happens slower than electron diffusion and is thus the rate limiting process in the oxidation reaction.
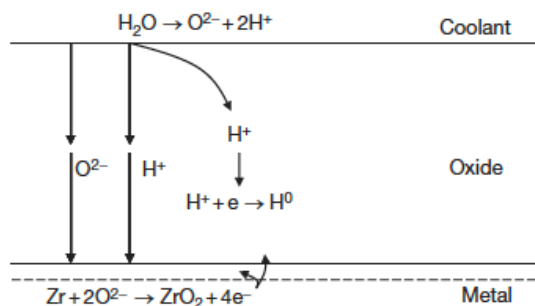
Figure 1-4 Corrosion Processes of Zirconium metal in Aqueous Environment by Ion Diffusion [22].

The oxide that forms has a columnar grain structure, however as oxidation progresses the tetragonal phase transitions to a monoclinic phase with an additional 5% volume expansion and equiaxed grain structure. The formation of this phase adds additional stress to the oxide layer, which eventually results in cracking of the oxide. While the oxidation reaction is diffusion controlled, the kinetics follow a cubic rate growth law. However, upon cracking of the oxide and an acceleration of the kinetics to a linear growth rate law occur. Following this brief period of accelerated corrosion, a new protective layer is formed on the metal oxide interface which again becomes protective. These cyclic oxidation cycles repeat as long the oxide remains adherent. A condition known as breakaway oxidation can occur when the cracking is so severe as to cause complete delamination and spallation of the oxide layer as it is formed resulting in very rapid oxidation rates as water is exposed to bare metal. This breakaway behavior was first seen unalloyed zirconium [22]. The cause of breakaway oxidation is still a subject of investigation; however, it is likely due to uneven oxidation on the cladding surface resulting in a wave like oxide which in turn develops a significant shear stress along the oxide metal interface resulting in oxide spallation.

Controlling the oxidation reaction by preventing breakaway and limiting overall oxide growth is achieved through controlling the impurities and adding alloying elements. The first zirconium alloys to be developed were the zirconium plus tin series known as Zircaloy. It has been discovered

that tin stabilizes the tetragonal oxide phase slowing the transition to monoclinic phase allowing for a thicker denser oxide to form prior to cracking. In this way it can offset the penalizing behavior of elements like nitrogen or carbon [22]. However, it has also been seen that further increases of tin result in increased oxidation kinetics. Thick tetragonal layers begin to grow unevenly and may result in highly localized stresses around grains with different oxidation rates. This leads to more severe cracking of the protective oxide and perhaps even spallation as described above. The iron, chromium, and nickel precipitates present in the zirconium matrix oxidize much slower than the zirconium and enter the oxide as an intermetallic metal. It is generally accepted that these result in an earlier transition to linear oxidation behavior in slowly oxidizing grains thus resulting in a more uniform oxide that is less prone to severe shear stresses and spallation. Thus, in controlling the oxidation of zirconium alloys it is desirable to provide some delay to the tetragonal to monoclinic phase transition, however too great of a delay in this transition results in non-uniform oxides that are not protective. Thus, there is a need to balance tin additions with iron, chromium, and nickel additions to achieve an optimum corrosion behavior. This has generally been the goal in the development of the Zircaloy series [23].

Another strategy for managing the corrosion of zirconium has been the addition of Niobium. Niobium is metastable in α-Zr, so its mechanism for improving corrosion is dependent on how it exists in the underlying microstructure. The β-Nb grains present in aged (and irradiated) metals act like the precipitates of iron, chromium, and nickel by accelerating the breakdown of the tetragonal oxide in slow growing oxide layers allowing them to catch up with faster growing regions resulting in a more uniform oxide [24]. However, while in solution with the α-Zr (as is the case in quenched microstructure) the niobium has the effect of stabilizing the tetragonal phase slowing the transition to monoclinic phase which is generally associated with the breakdown of the protective layer [25]. In this way its behavior is like that of tin. As such, the corrosion characteristics of zirconium niobium alloys can depend greatly on the heat treatments used in the manufacturing process as well as the in-service environment as this affects where the niobium exists in the metal matrix. Also balancing the niobium additions with those of iron and chromium can impact the corrosion behavior as different precipitates form with different sizes during the aging process [25][26].

A chief consequence of zirconium cladding oxidation is the absorption or pickup of liberated hydrogen ions in the zircaloy cladding. The terminal solid solubility before precipitation (TSS$_p$) of hydrogen in Zircaloy is a strong function of the metal temperature. Values were first reported by Kearns and are still widely used and discussed in literature [27]. While the solubility of hydrogen in Zircaloy is low, the hydrogen mobility in Zircaloy is high and diffusion occurs down the

concentration gradient according to Fick's law [28] and down the temperature gradient due to the Soret effect [29]. As the (TSS_p) of hydrogen in the Zircaloy is reached brittle delta phase zirconium hydrides will begin to precipitate out of the zirconium solution. The most common precipitate is the delta phase Zirconium Hydride. Due to the high mobility of hydrogen down the temperature gradient and low TSS_p at low temperatures, hydrides are most likely to precipitate out on the waterside edge of the cladding near the oxide layer. The morphology of the hydrides that form in the cladding depends on the crystallographic texture of the cladding. In RXA claddings hydrides can have a random orientation with precipitating in the radial direction and some precipitating in the circumferential (hoop) direction. Many RXA claddings employ a pure zirconium inner metal liner which result in a dense saturation of hydrides in the liner, followed by a hydride depleted zone and then an area of randomly oriented hydrides near the cladding outer surface as shown in Figure 1-5. The crystallographic texture of SRA Zircaloy causes these hydrides to plate out with a circumferential orientation, although the stress state of the cladding at the time of precipitation can play a major role in the morphology of the hydride precipitation [30]. Principally in SRA claddings dense clusters of circumferentially oriented hydrides often form near the waterside edge of the cladding which is referred to as the hydride rim and can grow to depths approaching 200 μm. Figure 1-6 shows two examples of this hydride morphology [31]. A comprehensive treatment on the issues of hydrogen absorption, diffusion, and solubility, as well as hydride orientation and morphology in Zircaloy claddings is given by Puls in *"The Effect of Hydrogen and Hydrides on the Integrity of Zirconium Alloy Components"* [32].
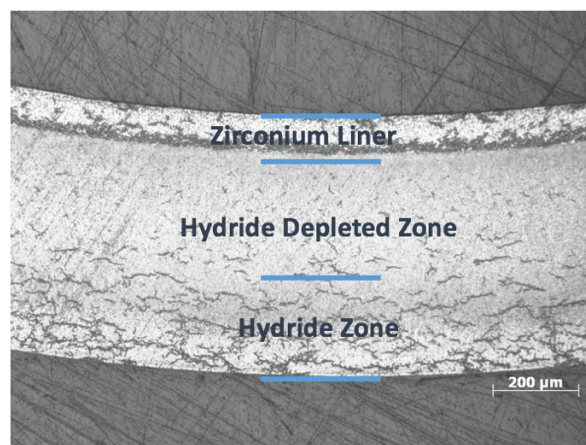
Figure 1-5 Hydride Morphology in Zr-2 RXA Cladding with Liner.
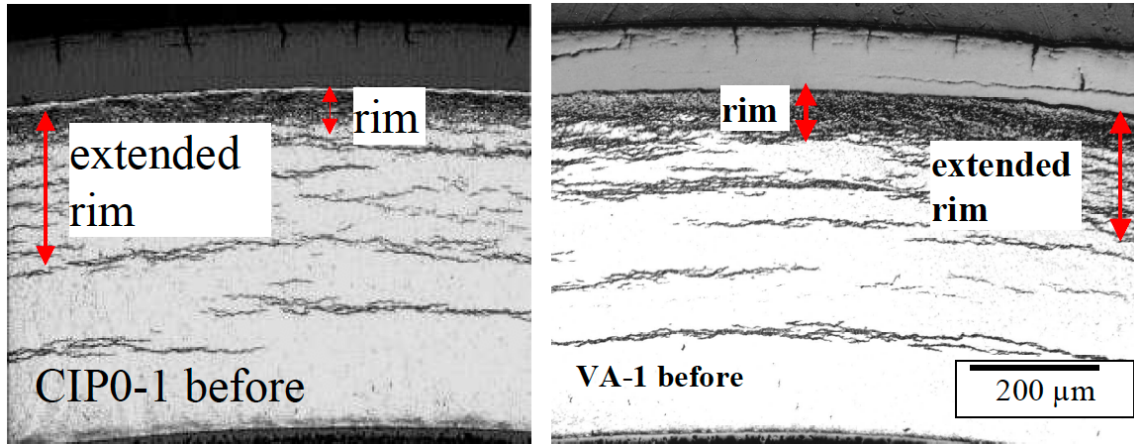
Figure 1-6 Circumferential Hydrides and Hydride Rims in Irradiated Stress Relieved Zirconium Alloy Claddings [31].

1.4 References

1 Papin J., Cazalis B., Frizonnet M., Desquines J., Lemoine F., Geogenthum V., Lamare F., Petit M., "Summary and interpretation of the CABRI REP-Na program," *Nuclear Technology*, Vol 157, No 3 (2017).

2 Fujishira T., Johnson R.L., MacDonald P.E., McCardell R.K. *Light Water Reactor Fuel Response During Reactivity Initiated Accident Experiments,* NUREG/CR-0269 (1978)

3 Nuclear Energy Agency, *Nuclear Fuel Safety Criteria Technical Review Second Edition,* NEA No. 7072 (2012)

4 Nuclear Regulatory Comission, NUREG 0800, Ch. 4.2, Rev. 3 no. 301, pp. 33–36, (2007)

5 Nuclear Energy Agency, *Nuclear Fuel Behavior Under Reactivity-initiated Accident Conditions State of the Art Report*, NEA No. 6847 (2010)

6 Z. Duan et al., "Current status of materials development of nuclear fuel cladding tubes for light water reactors," Nuclear Engineering and. Design, Vol. 316, (2017).

7 C. Lemaignan, "Zirconium Alloys Properties and Characteristics" Comprehensive Nuclear Materials (2012)

8 S. Banerjee "Nuclear Applications: Zirconium Alloys" Encyclopedia of Materials: Science and Technology (2001)

9 E. Tenckhoff, "Review of Deformation Mechanisms , Texture , and Mechanical Anisotropy in Zirconium and Zirconium Base Alloys," ASTM Int., Vol. 2, (2005).

10 R. Adamson, Zirconium Alloys - LWR Fuel Performance Seminar, July, 2015.

11 Hardy, D.G., "High temperature expansion and rupture behavior of Zircaloy tubing", Topical Meeting on Water Reactor Safety, Salt Lake City, USA, (1973).

12 Murty K.L., Seok C.S., Kombaiah B., "Burst and Biaxial Creep of Thin-Walled Tubing of Low c/a-Ratio HCP Metals" 6th International Conference on Creep, Fatigue and Creep-Fatigue Interaction (2013)

13 R. Daum, S. Majundar, H. Tsai, and T. Bray, "Mechanical Property Testing of Irradiated Zircaloy Cladding Under Reactor Transient Conditions," Small Specim. Test Tech. Fourth Vol. ASTM STP 1418, Vol. 4 (2002)

14 Shishov V., Peregud M.M., Nikulina A.V., et al "Influence of Structure-Phase State of Nb Containing Zr Alloys on Irradiation-Induced Growth" Journal of ASTM International Vol 2. (2005)

15 Wooding, S. J.; Howe, L. M.; Gao, F.; Calder, A. F.; Bacon, D., "A molecular dynamics study of high energy displacement cascades in alpha-zirconium" Journal of Nuclear Materials Vol 254 (1998)

16   Woo C.H., "Theory of irradiation deformation in non-cubic metals: Effects of anisotropic diffusion" Journal of Nuclear Materials Vol 159 (1988)

17   Northwood, D. O., Gilbert, R. W., Bahlen, L. E., et al. "Characterization of neutron irradiation damage in zirconium alloys – an international "round-robin" experiment" Journal of Nuclear Materials Vol 79 (1979)

18   Griffiths M. "A review of microstructure evolution in zirconium alloys during irradiation" Journal of Nuclear Materials Vol 159 (1988)

19   Holt R.A. "Mechanisms of irradiation growth of alpha-zirconium alloys" Journal of Nuclear Materials Vol 159 (1988)

20   Higgy H.R. Hammad F.H. "Effect of Neutron Irradiation on the tensile properties of zircaloy-2 and zircaloy-4" Journal of Nuclear Materials Vol 44 (1972)

21   Onimus F., Bechade J.L., "Radiation Effects in Zirconium Alloys" Comprehensive Nuclear Materials 4.01 (2012)

22   T. R. Allen, R. J. M. Konings, and A. T. Motta, "Corrosion of Zirconium Alloys" Comprehensive Nuclear Materials 5.03 (2012)

23   J. Wei, P. Frankel, E. Polatidis, M. Blat, A. Ambard, and R. J. Comstock, "The effect of Sn on autoclave corrosion performance and corrosion mechanisms in Zr – Sn – Nb alloys," Acta Mater., Vol. 61, (2013)

24   S. Kass, "THE DEVELOPMENT OF THE ZIRCALOYS," ASTM Int., 1964

25   B. A. Cheadle and S. A. Aldridge, "The Transformation and Age Hardening Behavior of Zr-19 WT% Nb," Journal of Nuclear Materials., vol. 47, (1973)

26   Y. H. Jeong, H. G. Kim, and T. H. Kim, "Effect of b phase , precipitate and Nb-concentration in matrix on corrosion and oxide characteristics of Zr – x Nb alloys," Journal of Nuclear Materials vol. 317, (2003)

27   J. Kearns, "Terminal solubility and partitioning of hydrogen in the alpha phase of zirconium, Zircaloy-2 and Zircaloy-4," Journal of Nuclear Materials vol, Vol. 22, (1967)

28   O. Courty, A. T. Motta, and J. D. Hales, "Modeling and simulation of hydrogen behavior in Zircaloy-4 fuel cladding," Journal of Nuclear Materials, Vol. 452, (2014)

29   D. S. Stafford, "Multidimensional simulations of hydrides during fuel rod lifecycle," Journal of Nuclear Materials Vol. 466 (2015).

30   M. N. Cinbiz, "The Effect of Stress State on Zirconium Hydride Reorientation," Pennsylvaia State University, (2015).

31   Georgenthum V., Sugiayam T., Udagawa Y., Fuketa T., Desquines J., "Fracture Mechanics Approach for Failure Mode Analysis in CABRI and NSRR RIA Tests" 2008 Water Reactor Fuel Performance Meeting, Seoul Korea (2008)

32   M. Puls, The Effect of Hydrogen and Hydrides on the Integrity of Zirconium Alloy Components. (2012)

Chapter 2: A review of cladding failure thresholds in RIA conditions based on transient reactor test data and the need for continued testing.

David Kamerman, Colby Jensen, Charles Folsom, Nicolas Woolstenhulme, Daniel Wachs

Abstract

Transient reactor experiments on light water reactor (LWR) fuel pins had been conducted since the beginning of the nuclear era to help determine core coolability and cladding failure thresholds. During one such test in November of 1993 at the CABRI transient test reactor on a test involving a high burnup fuel rod with a corroded Zircaloy-4 cladding it was first observed that cladding failures could occur prior to a departure from nucleate boiling (pre-DNB) at lower-than-expected peak radial average enthalpies. Thirteen additional tests would be performed in the CABRI reactor over the next decade on fuel rods with higher burnups. Additionally, a larger testing program at the NSRR reactor in Japan with high burnup fuel would uncover a similar trend of pre-DNB ruptures in high burnup test rods at lower-than-expected peak enthalpies. Numerous out of pile testing programs involving a variety of innovative mechanical testing techniques have been employed in an attempt to better quantify the failure thresholds of corroded zirconium alloy cladding in these rapid heating and loading conditions. While previously interim guidance had been issued, in June of 2020 the NRC officially published updated regulatory guidance to account of these pre-DNB failures in Regulatory Guide 1.236.

This paper will present an independent review of the publicly available transient reactor test database on higher burnup LWR pins conducted at the CABRI and NSRR reactors as well as review of a selection of published out of pile mechanical testing methods. The purpose of the review is to determine how well the new regulatory limits are supported by experimental data. The review will identify if additional transient reactor tests could provide additional support for the NRC guidance or identify the need for revisions. The evaluation will consider how far the existing database can be extrapolated when considering low hydrogen zirconium alloy claddings (with and without protective coatings) containing very high burnup (> 70 MWd/kgU) UO_2 fuel pellets. Finally, the authors will suggest how out of pile mechanical tests can be used in conjunction with a limited number of transient reactor tests to develop cladding specific failure thresholds in RIA type transients.

2.1   Introduction

Transient reactor experiments on light water reactor (LWR) fuel pins have been conducted since the beginning of the nuclear era to help determine core coolability and cladding failure thresholds. During one such test in November of 1993, at the CABRI transient test reactor, it was discovered that cladding failures could occur independent of a departure from nucleate boiling (pre-DNB) event. The test involved a fuel rod at high burnup with corroded, and subsequently hydrided, Zircaloy-4 cladding. Thirteen additional tests would be performed in the CABRI reactor over the next decade on fuel rods with higher burnups [1]. The initial CARBI tests were unusual in that they tested LWR fuel pins but in flowing sodium environment. However, a larger testing program at the NSRR reactor in Japan with high burnup fuel in static water capsules would uncover a similar trend of pre-DNB ruptures in high burnup test rods at lower-than-expected peak enthalpies [2]. The generally accepted mode of failure associated with these pre-DNB ruptures is a through thickness crack initiation and propagation in hydrided cladding as the result of tensile loads generated from pellet cladding interaction [3]. The term PCMI (pellet cladding mechanical interaction) is thus often used to describe these failures. In addition to the transient reactor tests, numerous out of pile testing programs involving a variety of innovative mechanical testing techniques have been employed in an attempt to better understand the failure mechanism and quantify the failure thresholds of hydrided zirconium alloy cladding in these rapid heating and loading conditions [4][5][6][7].

While previously interim guidance had been issued, in June of 2020 the NRC officially published updated regulatory guidance to account for these pre-DNB failures in Regulatory Guide 1.236 [8]. This paper presents an independent review of the publicly available transient reactor test database on higher burnup LWR pins conducted at the CABRI and NSRR reactors. The purpose of the review is to determine how well the new regulatory limits are supported by transient test data. The review will identify if additional transient reactor tests could provide additional support for the NRC guidance or identify the need for revisions. The evaluation will consider how far the existing database can be extrapolated when considering newer zirconium alloy claddings (with and without protective coatings) with low hydrogen pickup, but which contain very high burnup (> 70 MWd/kgU) UO2 fuel pellets. Additionally, a review of a selection of published out of pile mechanical testing methods will be conducted and the authors will suggest how out of pile mechanical tests can be used in conjunction with a limited number of transient reactor tests to develop cladding specific failure thresholds in RIA type transients.

2.2 Analysis of Transient Reactor Tests

A database of 82 transient reactor tests on moderate to high burnup LWR fuel pins tested in the CABRI and NSRR reactors was developed through consultation of a variety of open literature sources [1][2][9][10][11][12][13][14][15][16][17][18]. The peak fuel enthalpy, failure enthalpy (in the case of tests resulting in cladding rupture), transient pulse width, test coolant initial temperature, fuel type, fuel burnup, cladding type, cladding diameter, and thickness, observed oxide layer thickness, evaluated hydrogen content, and post transient permanent hoop strain were all documented. The value of each of these variables could not always be found for every test from primary sources however a similar effort by Beyer and Geelhood provided additional information to fill in most blanks [19]. Cladding hydrogen measurements are often calculated from oxide thickness measurements and assumed hydrogen pickup fractions for that cladding type adding some uncertainty to this parameter. Consultation of a paper by Georgenthum et al. allowed for the thickness of the hydride rim and extended hydride rim for 25 of the transient reactor tests to be included in the analysis [20]. Finally, 12 transient reactor tests at NSRR on unirradiated test rods that were artificially hydrided and filled with oversized UO2 pellets were added to the database as it was shown that rods in this condition similarly experienced 'pre-DNB' failures [21]. Inclusion of these tests brings the size of the database up to 94 transient reactor tests.

Regulatory Guide 1.236 provides different PCMI failure limits based on initial coolant temperature and cladding type. The cut off temperature between the different limits is 500 °F (260 °C). These limits are all expressed as a peak radial average enthalpy rise. Limits start at 630 J/g (officially 150 cal/g) and begin to decrease exponentially at a specified cladding excess hydrogen threshold which differs by cladding type in addition to initial temperature. The 630 J/g enthalpy rise limit is near that of the 711 J/g (officially 170 cal/g) total enthalpy limit which corresponds to a post DNB failure mode when one accounts for the starting enthalpy of the fuel particularly in hot coolant conditions.

Cladding types are grouped into stress relieved zirconium alloys (SRA) and fully recrystallized zirconium alloys (RXA). The logic for the differentiation is the morphology of hydrides commonly seen in zirconium alloys with different heat treatments. The SRA cladding types generally form hydrides with a dominate circumferential orientation, while RXA cladding types form hydrides with a random orientation [22]. For RXA claddings the guide makes a small distinction between those with inner liners and those without. Cladding types in the developed database considered to fit into the SRA category include Zircaloy-4, low tin Zircaloy-4, stress relieved Mitsubishi Developed Alloy (MDA), stress relieved New Developed Alloy (NDA), Zirlo, and low tin Zirlo. Cladding types in the

database considered to fit into the RXA category include Zircaloy-2, recrystallized MDA, and M5. 64 tests in the database consist of tests with SRA cladding while 30 consist of tests with RXA cladding.

2.2.1 Analysis of SRA Cladding Failure Limits

Of the 64 tests conducted with SRA cladding most of them, 47, took place at the NSRR reactor in a room temperature (cold) water capsule. Regulatory Guide 1.236 specifies a cladding excess hydrogen threshold of ~132 ppm after which the enthalpy rise limit begins to decrease exponentially to 209 J/g. Figure 2-1 below shows this limit with the 47 supporting transient reactor tests. The tests with unirradiated pre-hydrided cladding are shown in lighter blue. Tests that failed are plotted against their enthalpy rise at failure while tests that did not fail are plotted against their total enthalpy rise.
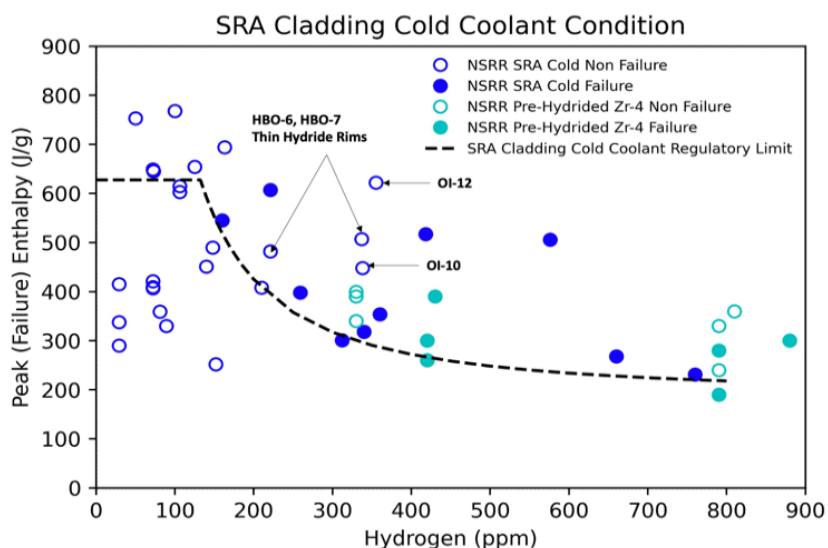
Figure 2-1 Low Temperature SRA Failure Limit with supporting transient reactor tests.

The proposed failure limit above the hydrogen threshold of 132 ppm seems well supported by the database. Tests HBO-6, HBO-7, OI-10, and OI-12 are anomalous as they have higher hydrogen contents (> 300 ppm) and do not fail even at substantial enthalpy rises. Consultation of the rim thickness by Georgenthum et al. [20] provides a useful explanation for two of these tests. HBO-6 and HBO-7 have thinner hydride rims than would be expected for cladding excess hydrogen reported. The more uniform distribution of hydrides in these test samples explains their added resilience. The rim structure of OI-10 is reported as being between 50 μm and 100 μm so it is more difficult to explain why this test rod survived. No additional information on test OI-12's hydrogen structure is available

but it is the only test in the database with the NDA cladding type so it is possible that an a-typical hydride structure exists in this cladding making it more resilient.

In these transient tests, instrumentation such as water pressure sensors, water column velocity detectors, and acoustic sensors are used to determine the time of failure. Enthalpy rise at failure is a calculated value that requires data from the reactor power, energy conversion factors, and heat transfer properties to be input into a thermos mechanical fuel performance code. Thus, while it is conventional to use the enthalpy rise at the time of failure values to support the development of cladding rupture limits it must be acknowledge that there is inherent uncertainty in the reported values. Using this convention, the NRC limit which primarily exists between ~300 J/g and ~200 J/g after ~300 ppm hydrogen seems to be well supported. In the pre-hydrided transients by Tomiyasu [21], tests of similarly hydrided cladding are shown to survive transients with peak enthalpy rises of 400 J/g but when subjected to a transient with a peak enthalpy rise of 550 J/g failure occurs at 260 J/g. These tests strongly imply that it would be incorrect to assume that because the test rod in the 550 J/g transient failed at 260 J/g, that such a rod would fail when subjected to a transient with a total enthalpy rise of 260 J/g. When the cladding failure cases presented in Figure 2-1. are plotted with respect to their peak enthalpy rise instead of their enthalpy rise at failure much greater separation of the failure and non-failure cases is seen. This plot is shown in Figure 2-2. While the observed hydrogen threshold (130 ppm - 300 ppm) does not change the failure limit would increase to around 400 J/g - 500 J/g.

Of the 17 tests that took place at elevated temperature, 5 took place in a heated version of the NSRR capsule, and the remaining 12 took place in the CABRI sodium loop. Regulatory Guide 1.236 specifies a cladding excess hydrogen threshold of ~160 ppm after which the enthalpy rise limit begins to decrease exponentially to 251 J/g. Figure 2-3. below shows this limit with the 17 supporting transient reactor tests. While the convention of plotting failed test pins at their enthalpy rise at the time of failure is held, annotations are added to the figure to show the peak enthalpy rise of these transients.
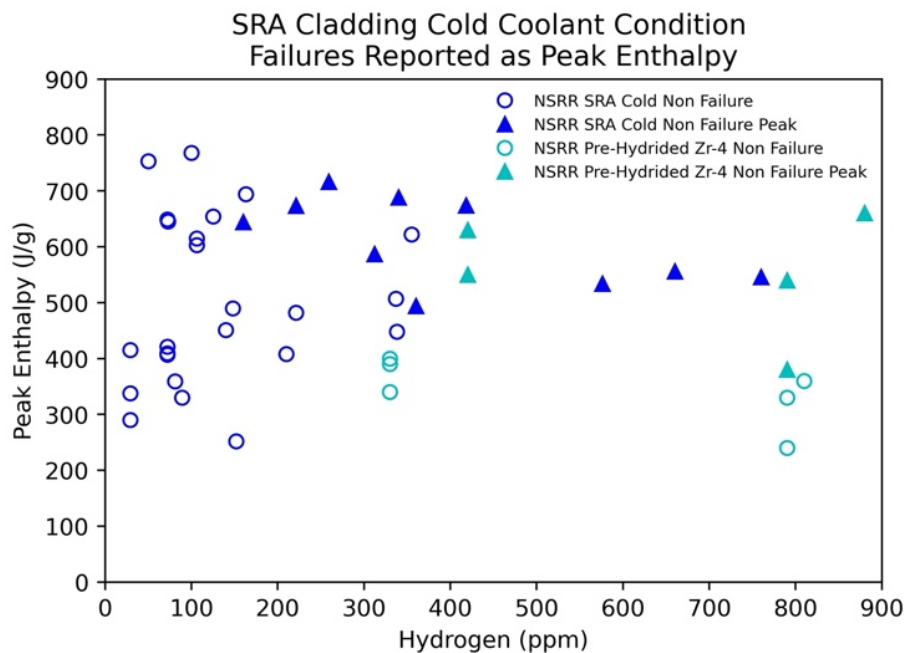
Figure 2-2 Low Temperature SRA Tests with Failure Cases plotted with Respect to Peak Enthalpy.
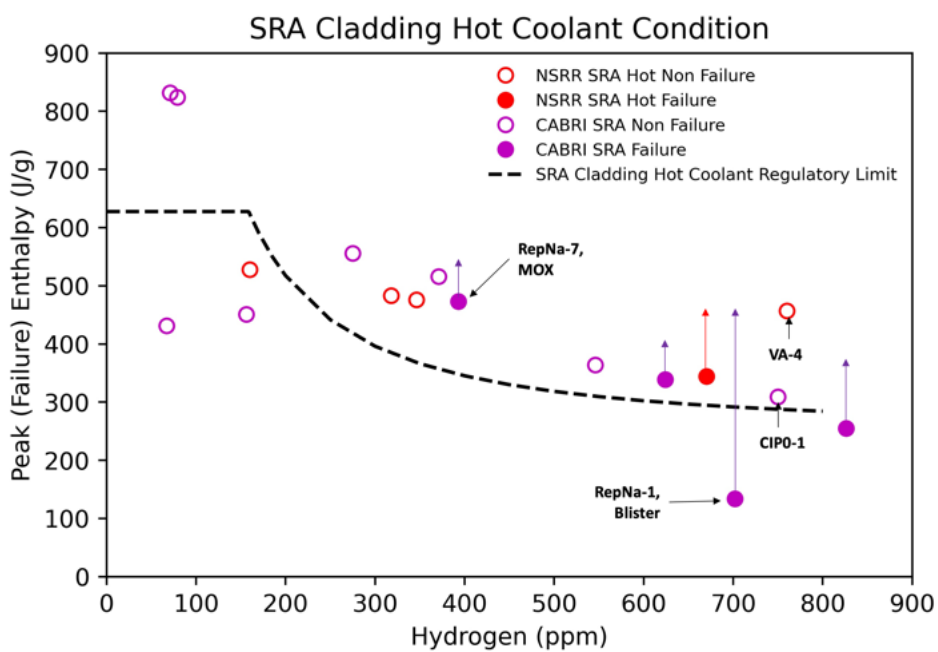
Figure 2-3 High Temperature SRA Failure Limit with supporting transient reactor tests.

The contrast of the high temperature test database when compared to the low temperature test database is striking. In addition to there being dramatically fewer tests, failures are rarely seen below 500 ppm – 600 ppm cladding hydrogen with only one test pin RepNa-7, a MOX rod, failing below this threshold. The enthalpy rise limit above 500 ppm – 600 ppm appears to be supported at around 300 J/g, when considering the enthalpy rise at time of failure. However, this limit would increase to between 400 J/g – 500 J/g range if the total peak enthalpy rise were to be considered. The survival of VA-4 and CIP0-1 provide additional, albeit limited, support for the higher limit.

The high temperature dataset itself provides some initial evidence for the consideration of rate affects, as intuitively slower transients allow for more time for cladding temperature to increase at a given PCMI load and it is obvious from the data set that warmer cladding is less prone to PCMI failure at a given hydrogen level. This observation has led many to wonder if the transient pulse width is an important factor which could influence the failure limit. While all the NSRR tests take place at very narrow pulse widths between 5 ms and 10 ms, CABRI testing took place at a larger variety of pulse widths between 9 ms and 75 ms. However, there is no clear distinction in failure limit when comparing tests of similar hydrogen content, irradiated in transients with different pulse widths. There are cases of failure at pulse widths greater than 30ms (RepNa-7, RepNa-8, and RepNa-10) and many cases of survival at pulse widths less than 30ms with cladding hydrogen level being the common differentiator affecting failure or survival. Due to the efficient cooling of the Na coolant in the CABRI RepNA tests pulse width effects maybe more muted than in PWR water [23]. There are no tests of comparable hydrogen content irradiated at different pulse widths which could be used to more conclusively justify or defend a pulse width effect on the failure limit.

The NRC failure limits for SRA cladding at cold temperature are well supported by the database, although higher (less conservative) limits could be justified if peak enthalpy rise rather than enthalpy rise at the time of failure were used. Therefore, the NRC failure limits for SRA cladding at high temperature may be too conservative particularly in the range of cladding excess hydrogen levels between 160 ppm and 500 ppm. However, it is admitted that the database is particularly sparse in this region and so a conservative limit may be justified. Thus, when considering the current regulatory limits, the most useful transient tests for SRA cladding types would be tests with cladding hydrogen contents between 100 ppm and 600 ppm in a hot water capsule with peak enthalpy rises greater than 450 J/g.

2.2.2 Analysis of RXA Cladding Failures

Of the 30 tests conducted with RXA cladding most of them (24 total) took place at the NSRR reactor in a room temperature (cold) water capsule. Regulatory Guide 1.236 specifies a cladding

excess hydrogen threshold of ~62 ppm for regular cladding types and ~77 ppm for claddings with a zirconium liner after which the enthalpy rise limit begins to decrease to 138 J/g. Figure 2-4 shows this limit with the 24 supporting transient reactor tests.

The proposed limit seems conservative for cladding with excess hydrogen contents between 62 ppm and 159 ppm as no failure data exists below 159 ppm hydrogen (test FK-9). Additionally, most of the non-failure data is at peak enthalpies below the failure limit. However, only one test with cladding hydrogen content greater that 159 ppm does not fail, test OS-2. The lack of transient reactor tests which survive even small enthalpy rises above this threshold may lead some to wonder if the proposed limit is too generous in this region. In fact, test OS-1 fails below the NRC limit. This test and OS-2, which conversely does not fail above the limit are the subject of much discussion in the community due to the use of pellet dopants in these fuel rods which may affect the test outcomes. Tests FK-10 and FK-12 were unique in that they were tested at ~80 °C to simulate warming that would occur in longer pulse widths. While the failure enthalpies for these tests is slightly higher than parallel tests FK-6 and FK-7 the difference is marginal. Thus, these tests would seem to indicate that the small amount of additional heating provided to the cladding in longer pulse width tests is insufficient to provide a notable change in the failure limit and that temperatures above 100 °C are needed for ductility recovery to become meaningful.
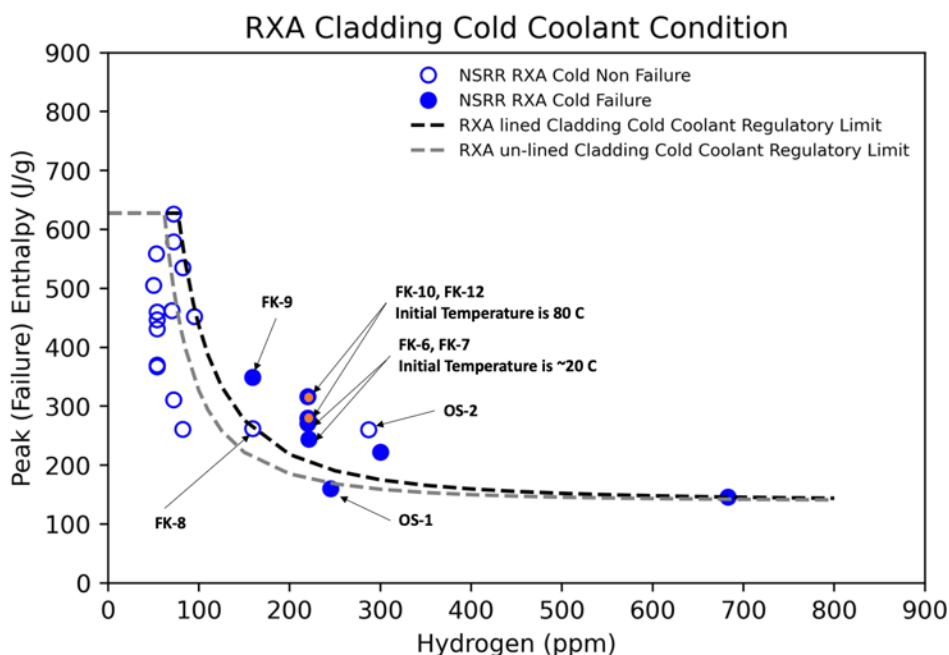
Figure 2-4 Low Temperature RXA Failure Limit with supporting transient reactor tests.

Only 6 tests have taken place on RXA claddings at elevated temperatures which simulate hot zero power conditions. Four of these tests are in the NSRR hot water capsule and 2 are in the CABRI Na loop. Regulatory Guide 1.236 specifies a cladding excess hydrogen threshold of ~74 ppm for regular cladding types and ~93 ppm for claddings with a zirconium liner after which the enthalpy rise limit begins to exponentially decrease to 209 J/g. Figure 2-5 shows this limit with the supporting tests. Due to the very limited number of tests at this condition it is very difficult to say that the proposed limit is either supported or not. A few tests in the NSRR hot capsule, LS2 and LS3 would seem to indicate that the limit is conservative particularly for claddings with excess hydrogen contents less than 300 ppm.

When considering the current regulatory limits, the most useful transient tests for RXA cladding types would be tests with cladding hydrogen contents between 100 ppm and 300 ppm in a hot water capsule, although more tests in the cold-water capsule would also be useful, with peak enthalpies greater than 450 J/g at a variety of pulse widths.
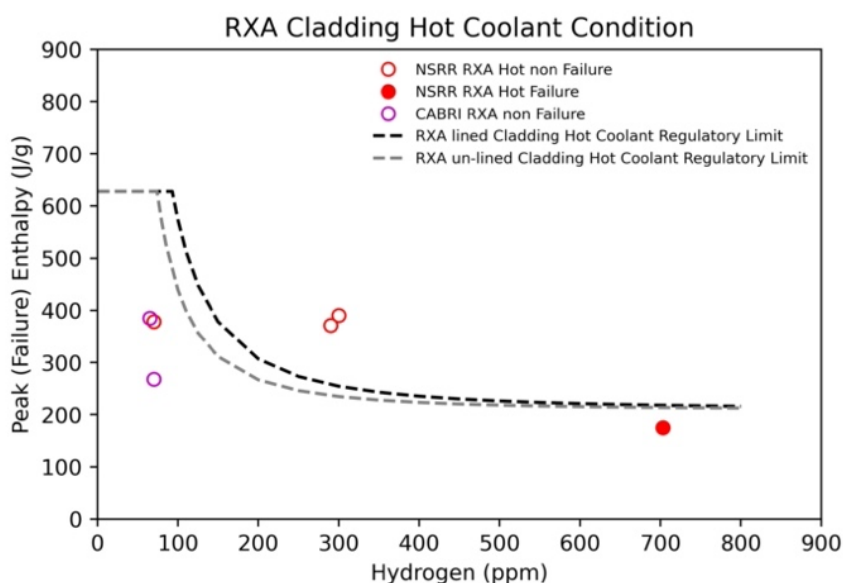
Figure 2-5 High Temperature RXA Failure Limit with supporting transient reactor tests.

2.3   High Burnup UO$_2$ Fuel with Low Hydrogen Cladding

Efforts are underway in the U.S. to develop accident tolerant fuel rod claddings that incorporate a coating on the zirconium alloy which dramatically reduce in-pile corrosion and hydrogen pickup [24]. Even without these novel coatings, modern alloys such as M5 and Axiom products produced by Framatome, and Westinghouse dramatically reduce hydrogen pickup from the

Zr-2 and Zr-4 test rods which dominate the transient RIA database [25]. The ambitions of the U.S. industry are to use such claddings to support longer cycle lengths and higher rod average discharge burnups (75 GWd/MTU) to improve the fuel cycle economics of the current LWR operating fleet. Such a quest poses the question of whether the use of a low hydrogen PCMI failure limit is appropriate for fuel rods which contain advanced, low hydrogen claddings, but may have very high burnup (>85 GWd/MTU peak pellet) UO2 fuel pellets. Research on the performance of high burnup fuel in Loss of Coolant Accidents (LOCA) suggest that high burnup UO2 is prone to significant fragmentation and pulverization when heated at rate of 5 °C/s with a threshold of ~700 °C [26]. The ramp rates and terminal fuel temperature in even moderate RIA transients are much more severe than those of LOCA transients, although the transients occur at high pressures, which impose a hydrostatic constraint on the fuel. Hydrostatic constraint has been shown to limit the extent of fuel pulverization in high temperature transients [27]. If fuel pellets fragment finely prior to cladding rupture during an RIA transient, they could cause a greater load on the cladding than that imposed by a (mostly) thermally expanding solid fuel pellet. Additionally, the high accumulation of Plutonium in the pellet rim region leads to non-uniform heating of the fuel pellet and volumetric expansion associated with potential melting of the fuel in the pellet rim region. While cladding strength and ductility will be improved due to the low hydrogen content, a cladding rupture with finely fragmented or molten fuel presents a greater safety concern to the reactor pressure vessel upon potential cladding breach than does solid pellets. It is therefore suitable to assess whether the current transient reactor testing database is sufficient to allow for the extrapolation of the low hydrogen limits to fuel rods with very high burnup UO2 fuels.

Figure 2-6 shows a plot of all the transient reactor tests with moderate and high burnup UO2 tests (MOX tests removed). There are several tests with very high burnup UO2 pellets that failed due to their cladding's high hydrogen content and so far, no evidence of finely fragmented or molten fuel coolant interactions have been reported with the test results although the transient enthalpy rises in these tests are generally below 600 J/g. Figure 2-7 below shows the transient reactor test database with all the high hydrogen claddings removed and plotted against their fuel burnup. Hydrogen thresholds of 300 ppm for SRA claddings and 150 ppm for RXA claddings are used in selecting the tests to be displayed. There are very few tests above the current U.S. burnup limit of 62 GWd/MTU rod average burnup and only one test above the current U.S. industry desired limit of 75 GWd/MTU rod average burnup (also assume rod average burnup is ~6% lower than the segment values displayed).

NRC has conducted its own review of the current transient reactor database and concluded that while the current database is sufficient up to 68 GWd/MTU rod average, more testing would be required to justify the extrapolation of the current limits beyond this burnup level [28]. Conclusions from this review mirror that of the NRC review suggesting that more testing should be performed for fuels with high local burnups with peak enthalpy rises around and above the current low hydrogen limit of 627 J/g to not only assess for suitability of the failure limit but also to assess impacts of pulverized or molten fuel coolant interaction in regard to pressure boundary integrity, which may challenge the core coolability limit. This document also underscores the need for more testing at higher enthalpies for low hydrogen alloys, most of which are of the RXA type, particularly at high temperature.

While integral testing of irradiated fuel segments requires unique resources, several opportunities have been identified that will add significant value to the nuclear community. Test campaigns are recommended to focus on samples with RXA cladding types with high and very high burnup UO2 fuel pellets. Recommended test conditions are elevated initial water temperatures (> 260 °C) and target peak enthalpy rises of 627 J/g or greater. If possible, testing should target a range of pulse widths between 5 ms and 100 ms to better understand any effects of pulse width on failure limit.
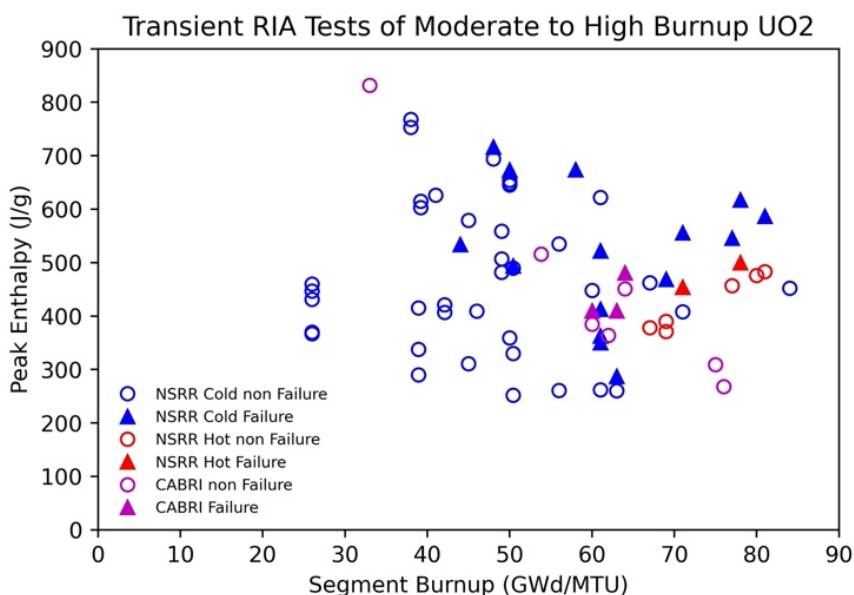
Figure 2-6 Transient reactor tests with moderate to high burnup UO2 fuel plotted as function of burnup.
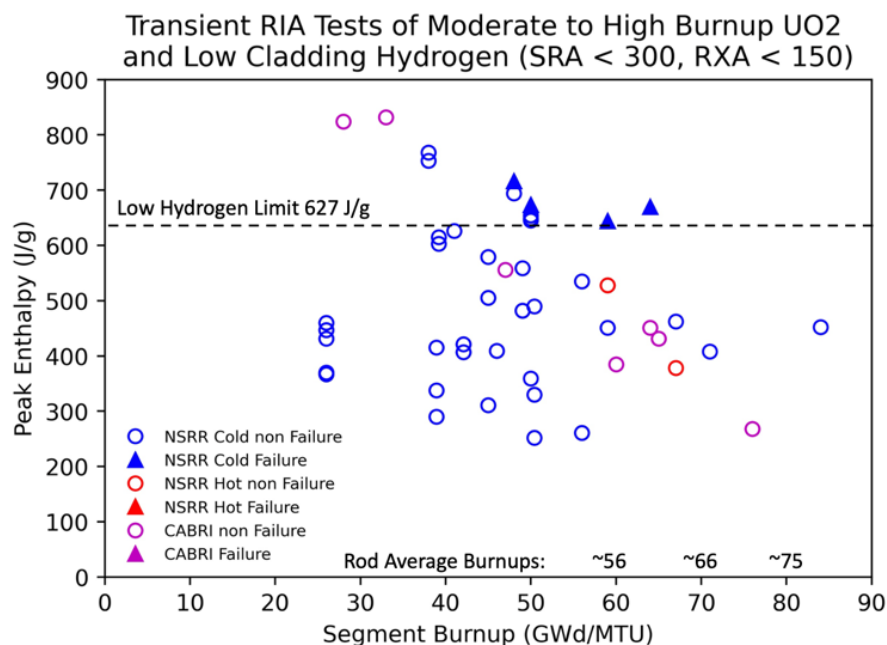
Figure 2-7 Transient reactor tests with low hydrogen claddings plotted as a function of burnup.

2.4 Proposing Cladding Hoop Strain Limits

If the dominate loading mechanism causing pre-DNB rupture is PCMI then the specification of cladding specific strain limits could potentially be used in place of fuel peak radial average enthalpy rise limits for assessing failure thresholds. Figure 2-8 shows the residual or permanent hoop strains of transient reactor tests which did not fail, along with the maximum strain which could be imposed by a thermally expanding UO2 fuel pellet. Tests with hoop strains below the UO2 expansion strain likely had some amount of a pellet cladding gap or experienced a significant amount of elastic hoop strain which was recovered upon unloading. Test rods with hoop strains at or greater than the UO2 thermal expansion strain are potentially explained by either additional loadings to the cladding such as fuel pellet gaseous expansion or transient fission gas release. Exceptionally high hoop strains may be achieved only if a boiling crisis occurs on the cladding coolant surface which is likely to have occurred in several of the NSRR tests with higher enthalpy targets. TK-1, TK-6, and TK-9 all have residual hoop strains greater than 10% and are thus not plotted in Figure 2-8 and likely expanded during a boiling crisis which occurred during those tests. The RepNa-9 test was a MOX rod and saw a 7.2% residual hoop strain. Other MOX rods often see higher hoop strains than similar UO2 rods indicating additional loading terms, other than thermal expansion, are more prevalent in MOX rods particularly when subjected to high enthalpies. Tests with UO2 rods do not have residual hoop strains

notably larger than the thermal expansion strain until ~500 J/g in the case of the hot NSRR capsule or ~600 J/g in the case of the cold NSRR capsule.
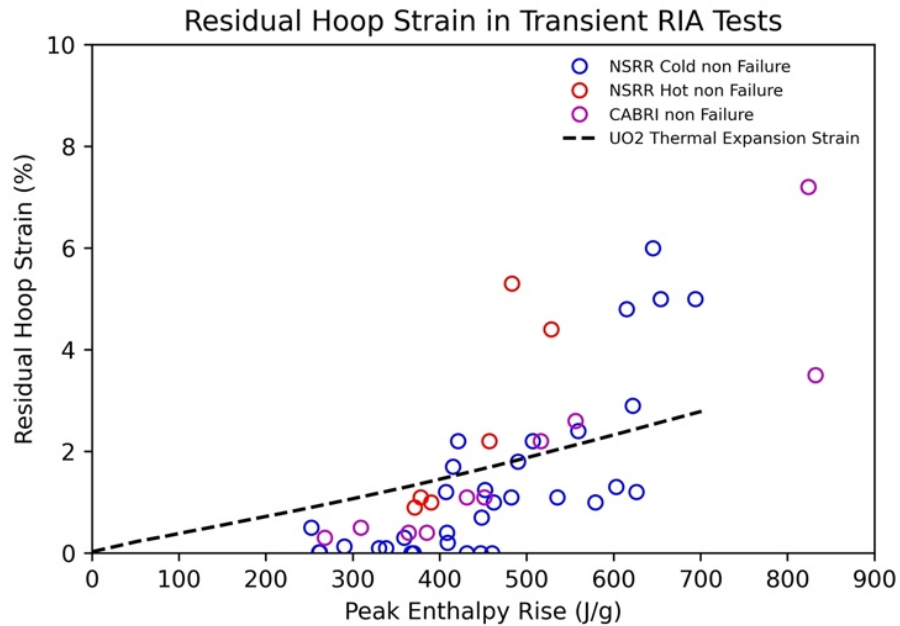
Figure 2-8 Permanent hoop strain in transient reactor tests which did not fail.

2.4.1 Analysis of Separate Effects Tests

Four separate effects test techniques are discussed below. The review of separate effects, mechanical testing presented herein is not intended to be an exhaustive review of cladding mechanical testing campaigns but rather to present an overview of available techniques and to compare the developed strain thresholds to the transient reactor test database. Three of the test campaigns discussed all involve Zr-4 (SRA) cladding with artificially hydrided cladding tubes. The modified burst test results use irradiated cladding tubes with the fuel removed.

Daum et al. [4] conducted ring tensile tests using a small gauge region designed to induce a bi-axial plane strain stress state during loading as shown in Figure 2-9 These kinds of tests are referred to as plane strain tension (PST) tests. Fracture strain was measured using a series of notches in the gauge region which are examined upon failure. Tests were conducted at room temperature and at 300 °C. Several of the drawbacks of the PST tests include non-uniformity of the stress state over a very localized area of the cladding. Highly local stresses often lead to early failure.
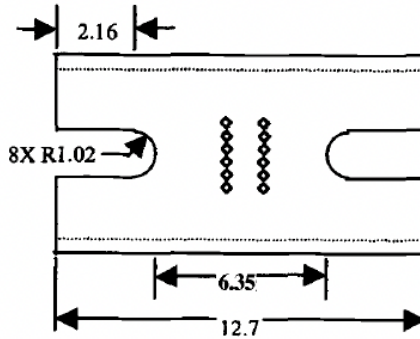
Figure 2-9 Plane Strain Tension Geometry used by Daum et al. [4].

Expansion due to compression (EDC) tests seek to remedy this shortcoming by imposing the hoop strain uniformly across the entire circumference of the cladding tube. Menibus et al. [5] conducted a campaign of EDC tests with hydrided cladding. The EDC tests attempted to create a bi-axial stress state like an expanding pellet by restraining the cladding in the axial direction as shown in Figure 2-10 Fracture strains reported by Menibus et al. are much larger than those reported by Daum et al. A principal drawback of the EDC test is that the expanding media begins to impose a bending moment on the cladding at relatively low hoop strains. The imposed shear stresses in the cladding allow for higher deformations than in a true bi-axial stress state as the shear stresses promote plastic flow. The fracture strains reported by Menibus et al. are likely to overestimate the hoop strain available to cladding during a transient reactor test with high principal stresses with no bending or shear terms.
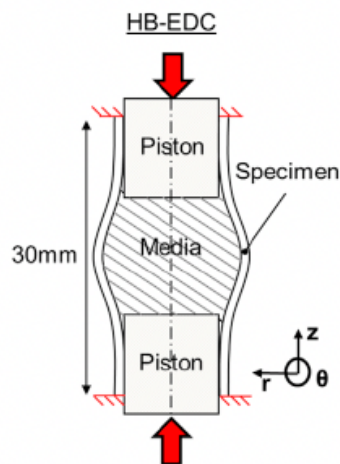
Figure 2-10 Expansion due to compression tests conducted by Menibus et al. [5].

Simple burst tests do perhaps the best job of simulating a highly uniform and constrained bi-axial principal stress state in thin wall cladding tubes. Such testing has been performed by Nagase and Fuketa [6]. Nagase and Fuketa use a fluid medium to achieve very high pressurization rates like transient reactor loading rates. To achieve high temperature a nonflammable silicon oil is used. Yueh et al. [7] designed a modified burst test where the pressurizing fluid expands an Inconel 718 driver tube which is placed inside the Zircaloy-4 test sample. The modified burst test has many practical advantages on traditional burst tests when conducted in a hot cell environment as the fluid pressure boundary never ruptures and pressure fittings do not need to affix to test samples. However, in modified burst tests it is much more difficult to relate the driving pressure to sample wall stresses.
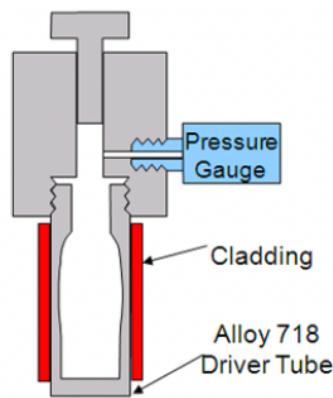
Figure 2-11 Modified burst test used by Yeuh et al. [7].

Figure 2-12 and Figure 2-13 show the residual hoop strains of un-failed transient reactor tests with SRA cladding plotted along with the fracture strains identified in separate effects tests. The fracture hoop strain data displays notable scatter due to the varying test methods employed. Often the residual hoop strain in transient reactor RIA tests is larger than the predicted fracture strain in separate effects tests. The discrepancy is likely since the separate effects tests take place in isothermal conditions while the transient reactors tests result in a rapid heating in addition to a rapid loading of the cladding. Additionally, the condition of the hydrides in the pre-hydrided test samples used in separate effects tests do not always mirror those present from typically irradiated fuel rods (e.g. hydride blisters in the Menibus [5] study vs more common hydride rims). In very few of the separate effects tests are strain measurements performed in-situ and only in traditional burst tests is it possible to quantify the cladding wall stresses during the tests.
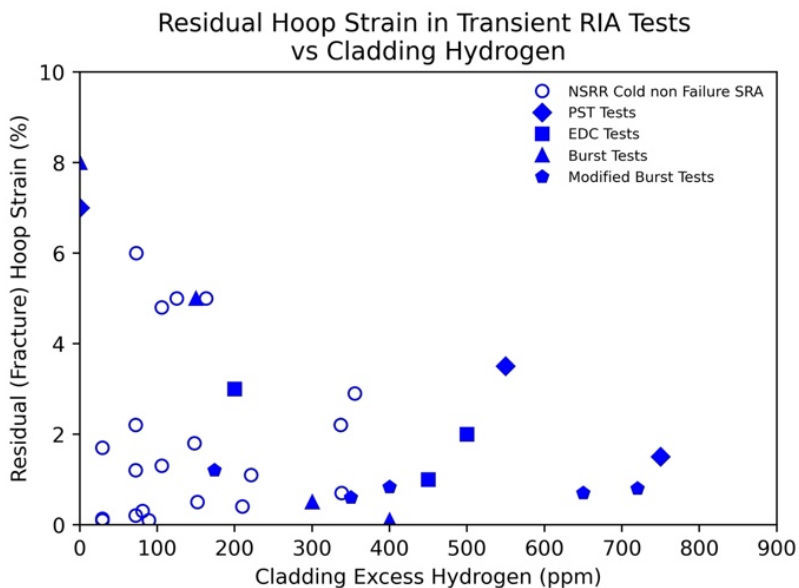
Figure 2-12 Residual hoop strain in cold transient reactor tests with fracture strains developed from separate effects test data.
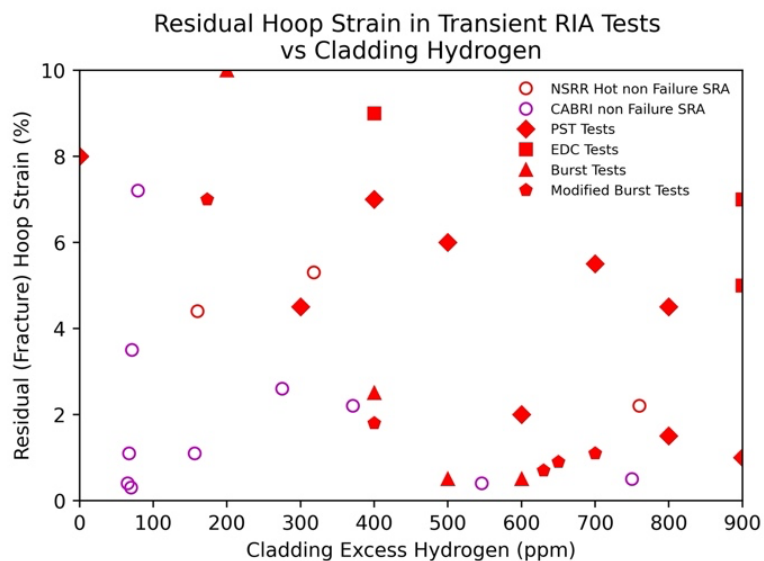
Figure 2-13 Residual hoop strain in hot transient reactor tests with fracture strains developed from separate effects test data.

2.4.2 Design Requirements for an Ideal Separate Effects Test

Brittle fractures are the result of stored energy in the material matrix while ductile fractures are the result of void formation and coalescence when available ductility is exhausted. In an ideal separate effect test, one would not only aim to simulate the loading conditions but also quantify both

the amount of elastic strain energy stored in the cladding and the amount of equivalent plastic strain the sample experienced prior to rupture (brittle failure) or necking (ductile failure). While these values can be computed for the tests in question given an appropriate stress/strain constitutive relationship, available stress/strain correlations are often built upon uni-axial test data and many times do not account for the effect of hydrogen present in the cladding. Simple burst tests offer a straightforward way of creating a quantifiable bi-axial stress state in semi-thin-walled cladding tubes. Both the axial and hoop stress can be determined from knowledge of the internal pressure value. If the burst test is incorporated into a mechanical load frame, then an independent axial constraint term can be added which is necessary when isotropic yielding cannot be assumed as is often the case in textured zirconium alloys. Both the axial and hoop strain should be measured in-situ so that stress strain correlations can be developed. The use of strain gauges, extensometers, or digital image correlation equipment can be used for this application given a suitable temperature for the measurement devices.

2.5 Conclusions

This review concludes that the regulatory guidance for cladding failure due to PCMI during transient RIA analysis is well supported for SRA and RXA cladding types at low temperature. For SRA cladding types at high temperature the limits are supported at high cladding hydrogen levels but may be conservative at moderate and low hydrogen levels. Data for RXA claddings at high temperature is insufficient to make a conclusion. The need for more in-pile transient RIA testing of irradiated fuel rods with RXA claddings with low to moderate excess hydrogen levels and high to very high burnup UO2 pellets in a hot water capsule is underscored by this review.

For cladding hoop strain evaluation, several out-of-pile separate effects testing techniques were evaluated in relation to existing data. The goal of such testing should be to develop cladding-specific failure limits. While simply determining a hoop strain limit would be convenient, it may be more appropriate to express cladding failure limits in terms of maximum equivalent plastic strain for ductile failures or an elastic strain energy density limit for brittle failure. Separate effects tests should, if possible, make use of irradiated cladding materials. As a lesser alternative, artificial hydride structures can be used, with careful consideration in their creation to ensure hydride structures are prototypic of those that form in the cladding type in question. The controlled loading conditions of the burst test method, where cladding hoop and axial strain are measured concurrently, are argued to be the most effective for analyzing material behavior and aiding in determining a relevant failure limit. Data of this kind should serve in interpreting the limited number of in-pile transient reactor RIA tests that can be performed.

2.6 References

1   Papin J., Cazalis B., Frizonnet M., Desquines J., Lemoine F., Geogenthum V., Lamare F., Petit M., "Summary and interpretation of the CABRI REP-Na program," *Nuclear Technology*, Vol 157, No 3 (2017).

2   Udagawa, Yutaka., Sugiyama, Tomoyuki., Amaya, Masaki., "Thresholds for failure of high-burnup LWR fuels by Pellet Cladding mechanical interaction under reactivity-initiated accident conditions" *Journal of Nuclear Science and Technology* Vol 56:12 (2019)

3   Fuketa T. "Transient Response of LWR Fuels (RIA)" *Comprehensive Nuclear Materials* 2.22 (2012)

4   Daum R.S., Majumdar S., Bates D.W., Motta A.T., Koss D.A., Billone M.C. "On the Embrittlement of Zircaloy-4 Under RIA Relevant Conditions" *Zirconium in the Nuclear Industry: Thirteenth International Symposium, ASTM STP 1423* (2002) pp 702-719

5   Hellouin de Menibus A., Auzoux Q., Monagabure P., Macdonald V., Le Jolu T., Besson J., Crepin J., "Fracture of Zircaloy-4 cladding tubes with or without hydride blisters in uniaxial to plane strain conditions with standard and optimized expansion due to compression tests" *Materials Science and Engineering* Vol 604 (2014)

6   Nagase F., Toyoshi F., "Investigation of Hydride Rim Effect on Failure of Zircaloy-4 Cladding with Tube Burst Test" Journal of Nuclear Science and Technology Vol 42 (2005)

7   Yueh K., Karlsson J., Stjarnsater J., Schirire D., Ledergerber G., Munoz-reja C., Hallstadius L., "Fuel cladding behavior under rapid loading conditions" *Journal of Nuclear Materials* Vol. 469 (2016)

8   Clifford, P. *Pressurized-Water Reactor Control Rod Ejection and Boiling Water Reactor Control Rod Drop Accidents* U.S. Nuclear Regulatory Commission Regulatory Guide RG 1.236, June 2020

9   Romano A., Wallin H., Zimmermann M.A., Chawla R., "Modelling the CABRI high-burnup RIA test CIP0-1 using an extended version of the FALCON code" *Nuclear Engineering and Design* 236 (2006) pp 284-294

10 Fuketa, Toyoshi., Mori, Yukihide., Sasajima., Hido., Ishijima Kiyomi., Fujishiro, Toshio., "Behavior of High Burnup PWR Fuel Under a Simulated RIA Condition in the NSRR" *Specialist Meeting on Transient Behavior of High Burnup Fuel*; Cadarache France (1995)

11 Fuketa, Toyoshi., Sasajima Hideo., Sugiyama, Tomoyuki., "Behavior of High Burnup PWR Fules with Low-Tin Zircaloy-4 Cladding under Reactivity-Initiated Accident Conditions" *Nuclear Technology* Vol 133:1 (2001)

12 Fuketa, Toyoshi., Sugiyama, Tomoyuki., Nagase, Fumihisa., "Behavior of 60 to 78 MWd/kgU PWR Fuels under Reactivity-Initiated Accident Conditions " *Journal of Nuclear Science and Technology* Vol 43:9 (2006)

13 Sugiyama, Tomoyuki., Umeda, Mika., Sasajima, Hideo., Suzuki, Motoe., Fuketa, Toyoshi., "Effect of Initial Coolant Temperature on Mechanical Fuel Failure under Reactivity-Iniated Accident Conditions" *Proceedings of Topfuel 2009*; Paris France (2009)

14 Udagawa, Yutaka., Sugiyama, Tomoyuki., Amaya, Masaki., "Thresholds for failure of high-burnup LWR fuels by Pellet Cladding mechnical interaction under reactivity-initiated accident conditions" Journal of Nuclear Science and Technology Vol 56:12 (2019)

15 Nakamura, T., Kusagaya K., Fuketa T., Uetsuka H., "High Burnup BWR Fuel Behavior Under Simulated Reactivity Initiated Accident Conditions" *Nuclear Technology* 138 (2002) pp 246-259

16 Nakamura, T., Fuketa T., Sugiyama T., Sasajima H., "Failure Thresholds of High Burnup BWR Fuel Rods under RIA Conditions" *Journal of Nuclear Science and Technology* 41 (2004) pp 37-43

17 Nakamura, T., Yoshinaga M., Sobajima M., Ishijima K., Fujishiro T., "Boiling Water Reactor Fuel Behavior at Burnup of 26 GWd/tonne U Under Reactivity-Initiated Accident Conditions" *Nuclear Technology* 108 (1994) PP 45-60

18 Mihara T., Kakiuchi K., Taniguchi Y., Udagawa Y., "Follow-up Experimental Study on the Causes of the Low-Enthalpy Failure Observed in the Reactivity-Initiated Accident-Simulated Test on LWR Additive Fuels" *Proceedings TopFuel 2021*: Santander Spain (2021)

19 Beyer C.E., Geelhood K.J., *Pellet Cladding Mechanical Interaction Failure Threshold for Reactivity Initiated Accidents for Pressurized Water Reactors and Boiling Water Reactors* PNNL-22549 (2013)

20 Georgenthum, V., Sugiyama T., Udagawa Y., Fuketa T., Desquines J., "Fracture Mechanics Approach for Failure Mode Analysis on CABRI and NSRR RIA Tests" *Proceedings 2008 Water Reactor Fuel Performance Meeting*; Seoul Korea (2008)

21 Tomiyasu K., Sugiyama T., Fuketa T., "Influence of Cladding-Peripheral Hydride on Mechanical Fuel Failure under Reactivity-Initiated Accident Conditions" *Journal of Nuclear Science and Technology* Vol. 44 No. 5 (2007) pp. 733-742

22 Clifford P. *Memorandum to Timothy J. McGinty: Technical and Reulatory Basis for the Reactivity-Initiated Accident Acceptance Criteria and Guidance, Revision 1.*, ML 14188C423 (2015)

23 Ozer et al. "Assessment of Reactivity Transient Experiments with High Burnup Fuel," *proc 23rd water reactor safety information meeting* Oct 23-25, 1995, in NUREG/CP-0149 Vol 1

24 *Roadmap: Development of Light Water Reactor Fuels with Enhanced Accident Tolerance,* Idaho National Laboratory unpublished report 2012, INL/EXT-12-25305.

25 Daun Z., Yang H., Satoh Y., Murakami K., Kano S., Zhao Z., Shen J., Abe H., "Current status of materials development of nuclear fuel cladding tubes for light water reactors" *Nuclear Engineering and Design* Vol 316 (2017) pp 131-150

26 Bales M., Chung A., Corson J., Kyriazidis L., *Interpretation of Research on Fuel Fragmentation, Relocation, and Dispersal at High Burnup* RIL 2021-13 (2021)

27 Turnbull J.A., Yagnik S.K., Hirai M., Staicu D.M., Walker C.T., "An assessment of the Fuel Pulverization Threshold During LOCA-Type Temperature Transients" *Nuclear Science and Engineering* 179:4 (2015) pp 477-485

28 Clifford P. *Memorandum to Joseph E Donoghue: Regulatory Guide 1.236 Fuel Rod Burnup Range of Applicability* ML20090A308 (2020)

Chapter 3: Multi-Axial Plastic Deformation of Zircaloy-4 Nuclear Fuel Cladding Tubes

David Kamerman, Malachi Nelson

Abstract

The following work is motivated by the desire to devise an internal pressure test that can mimic a displacement-controlled loading scenario and demonstrate how to apply the multi-axial stress and strain data from the test to develop an elastic/plastic constitutive model for a thin-walled tubular component. This is achieved by conducting simultaneous measurements of tangential and axial strain during the pressure test and integrating these strain measures into a feedback loop with the pressure controller. It is shown how data from such a test can be used to develop a large mechanical property data set relevant to biaxial loading conditions. The data obtained have high confidence evidenced by their low variability and alignment with other literature studies. Additionally, data from these internal pressure tests combined with full-tube axial tensile tests allows for the derivation of the Hill anisotropic yield function. The developed Hill yield function is validated by comparing the plastic strain ratios from the full tube tension tests and by comparing the predicted yield stress in the tangential direction with measured values from ring tension tests in a previous study.

3.1 Background and Motivation

During reactor overpower transients, light-water reactor (LWR) fuel cladding is subjected to a multi-axial tensile loading from increasing rod internal pressure due to fission gas and as the result of pellet cladding interaction (PCI). These loads can exceed the cladding yield limits resulting in plastic deformation at high wall stresses. These high, multi-axial stress fields have the potential to cause stress fractures in the cladding. An evaluation of cladding performance in these transients requires development of a stress/strain constitutive model in both the elastic and plastic deformation regimes, which is valid for multi-axial loadings. Zirconium alloy cladding tubes commonly used in the LWRs display anisotropic yield behavior because of their unique crystallographic texture in which hexagonal close packed (HCP) basal poles in HCP crystals are aligned in the radial direction [1]. This texture is one that resists wall thinning [2] often resulting in axial deformation to accommodate changes in diameter. Constitutive models based on data from uniaxial tension tests have the potential to under predict the wall stresses during displacement controlled multi-axial yielding. In uniaxial tension tests, crystal slip can occur early on the most favorable crystallographic planes. In multi-axial loading scenarios, plastic deformation along these favorable slip planes may be inhibited due to an orthogonal constraining force. For thin-walled cladding tubes subjected to loading from either internal pressure or an expanding ceramic pellet, the principal loads are in the tangential and axial directions with an axial to tangential loading ratio of 0.5 (for internal pressure loadings), and between 0.5 and 1 (for PCI loadings depending on the degree of surface slip) [3]. This multi-axial stress state requires plastic deformation to occur principally through a reduction in wall thickness that is resisted by the crystallographic texture of the cladding. The scenario underscores the need to develop an elastic/plastic, stress/strain constitutive model for zirconium alloy cladding tubes based on data from multi-axial loading.

Displacement-controlled tensile loads from PCI are generally theorized to be the dominant loading mechanism early during an overpower transient [4][5]. This has led to many mechanical studies of cladding deformation using an expanding mandrel experiment where the displacement can be finely controlled. The resulting cladding strain can be measured through a variety of mechanical and optical means. Thus often, the goal of such studies is to find a strain-based failure criteria depending on cladding hydrogen content and temperature. A common way of achieving displacement-controlled tangential loading is through an expansion due to compression test where the displacing mandrel's radial expansion is achieved through its axial compression [6][7]. While the radial displacement can be precisely controlled in this manner, the transferred force is not multi-axial. While additional constraining loads can be added to achieve a multi-axial condition, this leads to a

complicated testing setup. Additionally, such tests can also produce a bending moment in the cladding around the edge of the compressed mandrel. In an alternative testing arrangement known as "modified burst tests" (MBT), radial expansion is achieved through internal pressurization of a driver tube [8][9]. This enables the MBT to transfer a multi-axial load that is displacement controlled. Calculation of stresses in both testing arrangements requires knowledge of mandrel cladding interaction as well as a high-confidence mechanical model of the mandrel to determine the magnitude of the translated force. While these tests provide useful data to assess ductility changes, the inability to measure cladding wall stresses limits the ability of these studies to evaluate stress strain correlations. Simple internal pressure tests offer the advantage of easily determining the cladding stresses, in the axial (σ_z), tangential ((σ_θ), and radial (σ_Z) directions from the internal pressure (P) using the tube internal radius (R_i) and wall thickness (t) from Equations (3.1), (3.2), and (3.3), based on thin wall approximation [10]. The von Mises effective stress ((σ_e) under internal pressure (plane stress) is also easily deduced as shown in Equation (3.4) [11].

$$\sigma_z = P \frac{R_i}{t} \tag{3.1}$$

$$\sigma_\theta = 2 * \sigma_z \tag{3.2}$$

$$\sigma_R = 0 \tag{3.3}$$

$$\sigma_e = \sqrt{0.5 * \left[(\sigma_\theta - \sigma_z)^2 + \sigma_\theta^2 + \sigma_z^2 \right]} \tag{3.4}$$

However, traditional pressure/burst tests are load controlled making determination of the ultimate tensile stress and uniform elongation limit difficult as the load is always increasing. Load controlled pressure burst tests have been performed to study the performance of Zircaloy and hydrided Zircaloy cladding tubes in this manner by Nagase and Fuketa [12][13]. These experiments clearly show the decreased in pressure capability and elongation at burst for tests with unfavorable hydride orientations. Load controlled pressures tests have also been performed to measure constant load creep properties such as work done by Lan et al [14] and Seok et al [15]. Tests by Nguyen et al incorporated a constraining biaxial tensile load and numerous instrumentations to determine the cracking behavior of coated Zircaloy claddings under varying stress biaxiality ratios at room temperature [16].

The following work is motivated by the desire to devise an internal pressure test that can mimic a displacement-controlled loading scenario and demonstrate how to apply the multi-axial stress and strain data from the test to develop an elastic/plastic constitutive model for the thin-walled structural component at prototypic temperatures.

3.2 Model Formulation

The coordinate system used in the elastic/plastic constitutive models below is the most convenient for thin-walled tubing. The coordinate system is Cartesian when one examines a differential element of cladding material with the first direction aligned with the tube's circumference (tangential or hoop direction), the second direction aligned with the tube's axial length, and the third direction aligned with the tube's radius (Figure 3-1). Throughout this work these directions will be referred to as the tangential (θ), axial (Z), and radial (R) directions, respectively. The tangential coordinate (θ) is a linear expression of the tube circumference or diameter and should not be confused with the common angular direction used in cylindrical coordinate systems. The models utilize the variable (σ) for the true stress and the variable (ε) for the true strain.
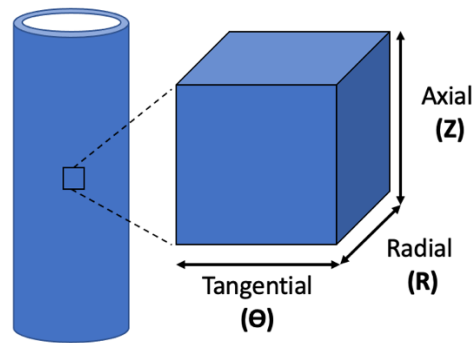
Figure 3-1 Coordinate System for Cladding Deformation Analysis.

In the elastic regime the multi-axial constitutive law can take a generalized form of Hooke's law where the shear stresses and shear strains are equal to zero. While yielding of thin-walled zirconium alloy tubing is known to be anisotropic, the elastic behavior is treated as isotropic. The stiffness matrix (S) can be expressed in terms of a Young's modulus (E) and Poisson's ratio (ν) as shown in Equation (3.5).

$$\begin{bmatrix} \sigma_\theta \\ \sigma_Z \\ \sigma_R \end{bmatrix} = \frac{E}{(1+\nu)(1-2\nu)} \begin{bmatrix} 1-\nu & \nu & \nu \\ \nu & 1-\nu & \nu \\ \nu & \nu & 1-\nu \end{bmatrix} \begin{bmatrix} \varepsilon_\theta \\ \varepsilon_Z \\ \varepsilon_R \end{bmatrix} \tag{3.5}$$

Strictly speaking, the strain vector (ε) in Equation (3.5) is an elastic strain vector. In the plastic regime, the plastic strain components must be subtracted from the total strains so that only the elastic components of strain are multiplied by the stiffness matrix. Determination of the plastic strain vector (ε^p) requires the formulation of a multi-axial anisotropic yield function and an associated

hardening law. The direction of the plastic strain vector comes from application of the plastic flow rule by taking the gradient of the yield function, and the magnitude of the plastic strain vector comes from the hardening law. The yield function will take a simplified form of Hill's anisotropic yield criterion neglecting the shear components, as shown in Equation (3.6) [17]. So that the Hill coefficients (F, G, and H) are purely directional in nature, the function is normalized by a value of $(\sigma_{e,p})^2$. The coefficient ($\sigma_{e,p}$), called the flow stress, is equal to the von Mises effective stress after yielding under an internal pressure loading. A simple power law hardening relationship is assumed, which is valid only for monotonically increasing loads and is shown in Equation (3.7). The equation applies the consistency condition for plastic flow and updates the flow stress ($\sigma_{e,p}$) from the yield stress ($\sigma_{e,p,yield}$) by a hardening coefficient (K) and the equivalent plastic strain (ε_{eq}^p) raised to a strain exponent (n)

$$F(\sigma_Z - \sigma_R)^2 + G(\sigma_R - \sigma_\theta)^2 + H(\sigma_\theta - \sigma_Z)^2 = {\sigma_{e,p}}^2 \tag{3.6}$$

$$\sigma_{e,p} = \sigma_{e,p,yield} + K\left(\varepsilon_{eq}^p\right)^n \tag{3.7}$$

Three independent equations are needed to solve for the Hill coefficients. Solutions for the Hill coefficients are traditionally found by conducting uniaxial tensile tests in each of the principal orthogonal directions (θ, Z, and R). However, this presents experimental challenges with thin-walled tubing and conflicts with the aim of evaluating material performance under multi-axial loading conditions. Internal pressurization provides an easily quantifiable multi-axial stress state for thin-walled tubing making this loading scenario an ideal initial selection. Substituting Equations (3.2) and (3.3) into Equation (3.6) allows one to derive Equation (3.8).

$$F + 4G + H = \frac{4\left(\sigma_{e,p}\right)^2}{(\sigma_\theta)^2} \tag{3.8}$$

A second equation can be derived from the internal pressure test through the application of the plastic flow rule which states that the direction of the plastic strains must be normal to the yield surface. Taking the gradient of Equation (3.6) and then again substituting Equations (3.2) and (3.3) allows one to equate the Hill coefficients to defined plastic strain ratios under an internal pressure load. These formulations are shown in Equations (3.9), (3.10), and (3.11). Note that these relationships are only valid under capped internal pressure loading and different correlations would need to be developed under uniaxial loading or with different multi-axial stress ratios.

$$\alpha \overset{\text{def}}{=} \frac{\epsilon_\theta^p}{\epsilon_z^p} = \frac{2G + H}{F - H} \tag{3.9}$$

$$\beta \overset{\text{def}}{=} \frac{\epsilon_\theta^p}{\epsilon_R^p} = \frac{2G + H}{-2G - F} \tag{3.10}$$

$$\gamma \overset{\text{def}}{=} \frac{\epsilon_Z^p}{\epsilon_R^p} = \frac{F - H}{-2G - F} \tag{3.11}$$

Equations (3.9), (3.10), and (3.11) are not independent thus requiring an additional equation, and the loading scenario, to fully develop the Hill coefficients. A uniaxial full-tube tension test in the axial (Z) direction makes an ideal complement to the internal pressure test as it is similarly straightforward to conduct and provides the necessary independent loading scenario. Under a uniaxial load in the axial (Z) direction, Equation (3.6) can be reduced as the principal stresses in the tangential (θ) and radial (R) direction are zero. This leads to a third independent equation (3.12) used to solve for the Hill coefficients.

$$F + H = \frac{\sigma_{e,p}^2}{(\sigma_Z)^2} \tag{3.12}$$

3.3 Test Procedure

Both full-tube axial tension tests and internal pressure tests are conducted to meet the data needs identified in the above model formulation. In both test configurations the test samples are loaded inside a custom box furnace capable of elevating the test sample temperature. The box furnace also provides the containment and safety function for the pressure tests. An argon purge line is connected to the furnace to limit sample oxidation during high-temperature testing. Epsilon Model 7675-025M and Model 7642-010M-025M high-temperature extensometers are used to monitor the tangential (θ) and axial (Z) expansion of the cladding tube during the tests. The full-tube axial tension tests are conducted using a standard Instron model 5967 universal testing machine.

For the internal pressure tests a Maxpro MTIG20-30-75-2 booster pump is used to elevate the pressure of an argon gas source up to 135 MPa. A Tescom 26-2000 pressure-reducing regulator, which is pneumatically controlled by a Tescom ER5000 controller, reduces the pressure in a downstream static pressure line to a desired set point. Pressure is monitored in an active feedback loop via a Tescom 2168 pressure transducer located behind the pressure-reducing regulator. The Tescom 26-2000 has a vent port so that pressure in the static line can be reduced if the pressure set point is lowered. Test samples are connected to the static pressure line using medium pressure

Swagelok fittings behind a bulkhead. A dead leg of medium pressure tubing is connected to the other end of the test sample and capped. The dead leg of the medium pressure tubing is axially unconstrained. An additional pressure transducer is located immediately below the bulkhead to obtain the most accurate internal pressure measurement in the sample. Between the two pressure transducers is a fast-acting nominally open Remarco solenoid valve programmed to close upon a significant pressure drop such as would occur if the test sample ruptured, limiting the amount of high-pressure compressed gas being expelled through the ruptured test sample. Figure 3-2 shows a schematic of the testing apparatus. A pseudo displacement-controlled test is achieved by programming the tangential (θ) extensometer into a proportional integral derivative feedback loop with the system pressure setpoint, using a Labview data acquisition system. Testing was terminated upon a 1 MPa drop in the pressure setpoint from its maximum value indicating that maximum uniform elongation had been achieved.
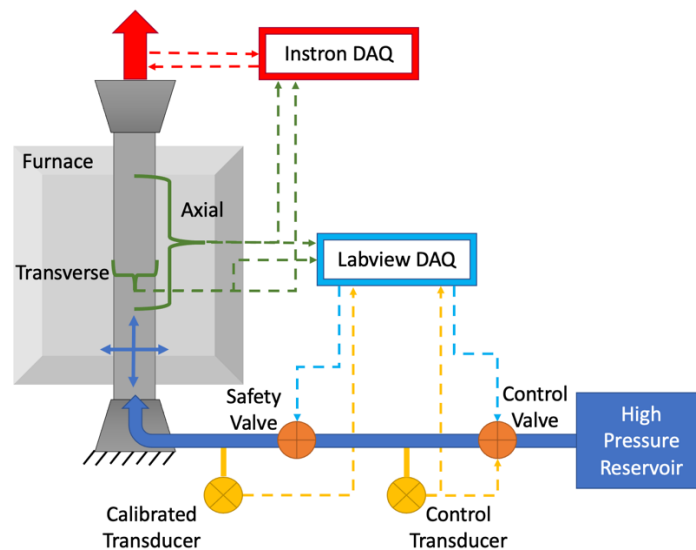
Figure 3-2 Cladding axial tension and pressure testing apparatus.

Zircaloy-4 cladding tubes with a nominal outer diameter of 9.5 mm and a wall thickness of 0.57 mm cut into 150 mm lengths are used in the present study. These tubes were commercially procured and conform to ASTM B353-12 [18]. Figure 3-2 shows a test sample with the tangential (θ) and axial (Z) extensometers connected to the testing apparatus. Tests are conducted at room temperature (~22°C), 150°C, 275°C, 400°C, and 525°C. The samples are heated for ~3 hours to reach the isothermal target temperature. The cladding was deformed at a programmed strain rate of 0.1% per

minute. The programmed strain rate corresponds to the tangential (θ) strain in the pressure test and the axial (Z) strain in the full-tube tension test. The loading rate either from internal pressurization or axial loading is not constant as these are strain controlled tests and the loading rate varies to achieve a programmed strain rate.
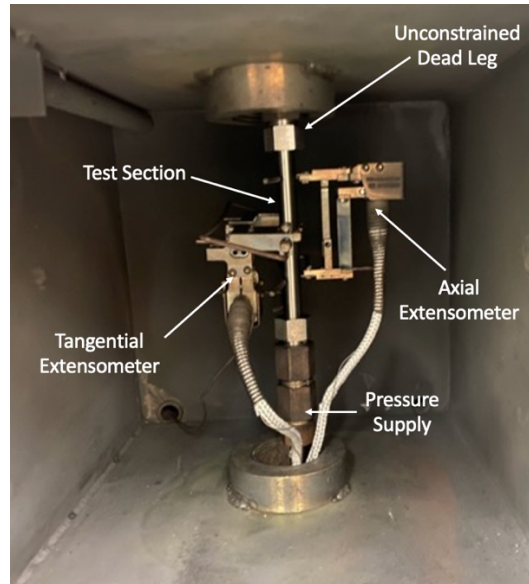
Figure 3-3 Zircaloy-4 cladding tube in pressure test apparatus.

3.4 Analysis Procedure

The first step in the data analysis is the determination of the yielding point. The yield point in both tests is determined by an offset line. The goal of the yield point determination is to determine when plastic deformation begins, and plastic strains begin to accumulate. For the pressure test, the slope of the offset line is equal to the rate of change of pressure in the elastic region. For the full-tube tension test the slope of the offset line is equal to the rate of change of the axial stress in the elastic region. The high-confidence elastic region used to develop the loading rates is determined for each temperature based on observed linearity in the data. The offset time is equal to the programmed strain rate divided by a defined strain offset of 0.02%. The yield point is the first point in the test at which the load crosses below the offset line. While it is conventional to use a 0.2% offset line to determine the yield strength, it was found that a significant deviation from linearity of the stress/strain response was observed between 0.02% and 0.2%. Thus, it was chosen to use a more stringent yield condition of 0.02% in this study. For the full-tube tension test Young's modulus (E) and Poisson's ratio (ν) can be found from an expansion and solution to equation (3.5) which are shown below in equations (3.13)

and (3.14). In these equations the variable (s) used for the engineering stress and the variable (e) used for the engineering strain. It is common engineering practice to use the measured engineering values to derive elastic constants and differences between engineering stress/strain and true stress/strain values are generally negligible in the elastic region.

$$E = \frac{s_Z}{e_Z} \tag{3.13}$$

$$\nu = \frac{e_\theta}{e_Z} \tag{3.14}$$

During the full-tube tension tests the fittings often failed after approximately 2% axial (Z) strain limiting the usefulness of these tests beyond the determination of the elastic constants and the yield stress. However, enough plastic deformation occurred to develop the plastic strain ratios. Figure 3-4 shows a plot of full-tube tension test data and the derived mechanical properties as well as the α strain ratio (change in engineering hoop plastic strain over change in engineering axial plastic strain) for the axial tension loading scenario.
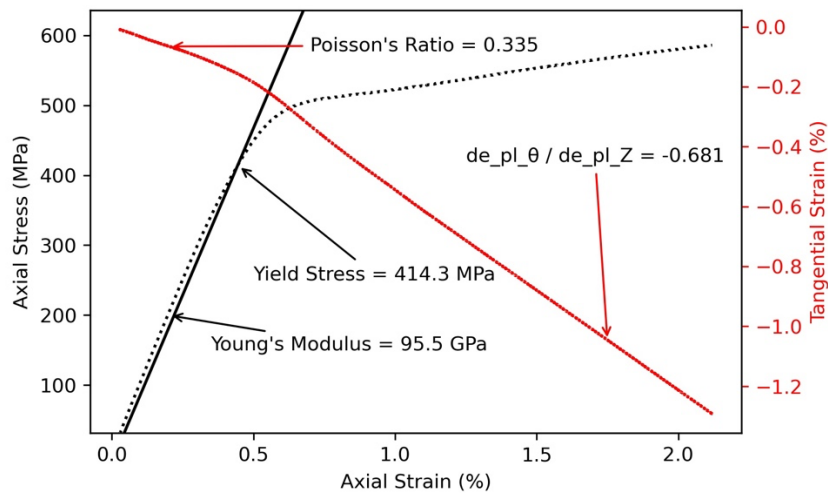
Figure 3-4 Stress strain data from a full tube tension test at room temperature.

Young's modulus (E) and Poisson's ratio (ν) are determined from pressure test data using an expansion of the multi-axial formulation of Hooke's law in Equation (3.5). These formulations are shown in Equations (3.15) and (3.16). Figure 3-5 shows a plot of internal pressure test data and the derived mechanical properties.

$$E = \frac{s_\theta}{e_\theta} - \frac{\nu s_\theta}{2e_\theta} = \frac{s_z}{e_z} - \frac{2\nu s_z}{e_z} \tag{3.15}$$

$$\nu = \frac{\left(\frac{s_z}{e_z} - \frac{s_\theta}{e_\theta}\right)}{\left(\frac{2s_z}{e_z} - \frac{s_\theta}{2e_\theta}\right)} \tag{3.16}$$
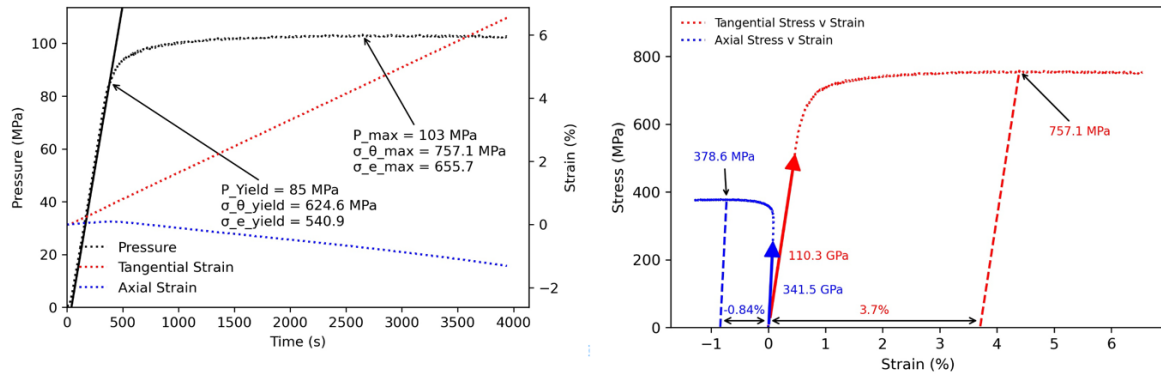
Figure 3-5 Stress strain data from an internal pressure test at room temperature; Young's Modulus was equal to 90 GPa and Poisson's Ratio was equal to 0.368 in this test.

3.4.1 Strain Decomposition

Determination of the true plastic strain ratios in the internal pressure test requires a separation of the measured strains into their elastic and plastic components after yielding. The elastic components of strain can be determined from the derived elastic constants and Equation (3.5). Tangential (θ) and axial (Z) components of true plastic strain can then be determined by subtracting the elastic components from their measured engineering values and applying natural logarithms as shown in equation (3.17).

$$\epsilon_{\theta,z}^{p} = \ln\left(1 + e_{\theta,z} - e_{\theta,z}^{e}\right) \tag{3.17}$$

Determination of the radial (R) component of plastic strain requires application of the incompressibility criterion for plastic flow, which states that the true plastic strain rates along three orthogonal directions must equal zero. Integrating the incompressibility criteria for the measured data set from the yield point (assume plastic strain at the onset of yielding is equal to zero) allows one to derive Equation (3.18). Figure 3-6 shows the full decomposition of strains and the calculated strain ratios from an internal pressure test at room temperature. The negative axial (Z) plastic strain (dashed blue line) confirms the expected anisotropic nature of the tubing as the volume conservation during

tangential expansion of the tubing is accomplished not only by wall thinning but also by axial shrinkage.

$$\epsilon_R^p = -(\epsilon_z^p + \epsilon_\theta^p) \tag{3.18}$$
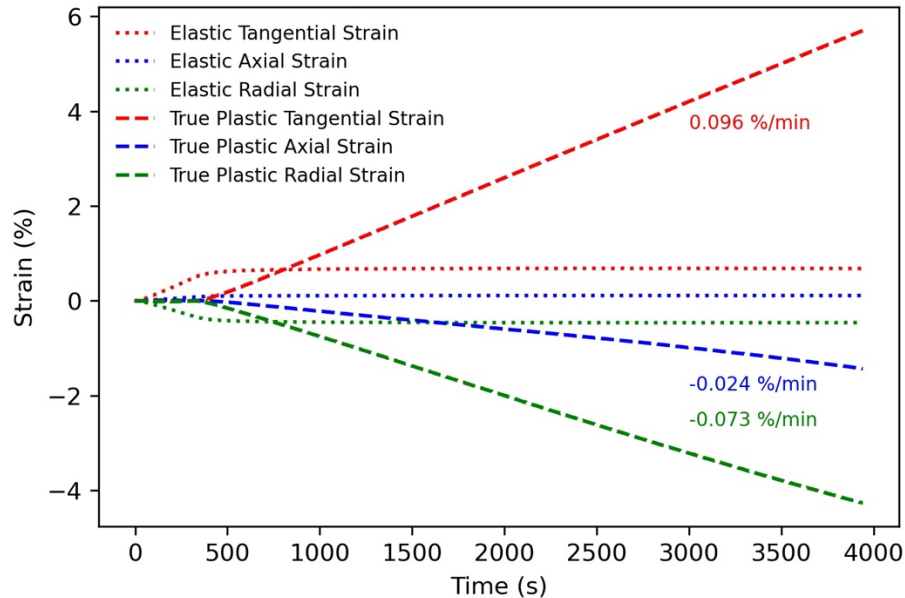
Figure 3-6 Decomposition of elastic and plastic strain components in a room temperature pressure test.

3.4.2 Power Law Hardening

It is assumed that during hardening the yield surface expands isotropically and that the degree of anisotropy does not change during hardening. This assumption is valid for monotonically increasing tensile loads with finite plastic strains. Under this assumption, a power law hardening model can be fitted to the data by relating an equivalent plastic strain to the von Mises effective true stress. The equivalent plastic strain can be determined from the plastic strain rate components derived above and then using a strain energy balance. The derived formulation is shown in Equation (3.19). Then, using the engineering tangential (θ) strain and engineering radial (R) strain to determine the true dimensions of the deformed cladding tube, the true axial (Z) stress is determined in Equation (3.20). The engineering radial strain used in Equation (3.20) is determined by re-arranging Equation (3.17) to solve for the total engineering strain for a given true plastic strain and elastic strain. True tangential (θ) stress can then be determined from Equation (3.2) and the true von Mises stress from Equation (3.4).

$$\epsilon_{eq}^p = \sqrt{\frac{2}{9}\left(\left(\epsilon_R^p - \epsilon_\theta^p\right)^2 + \left(\epsilon_\theta^p - \epsilon_z^p\right)^2 + \left(\epsilon_z^p - \epsilon_R^p\right)^2\right)} \tag{3.19}$$

$$\sigma_z = s_z \frac{(1 + e_\theta)}{(1 + e_r)} \tag{3.20}$$

The hardening coefficient (*K*) and the strain exponent (*n*) are determined by taking natural logarithms of Equation (3.7) and performing a linear regression where the slope of the regression line is equal to the strain exponent (*n*) and the intercept of the regression line is equal to the natural logarithm of the hardening coefficient (*K*). Figure 3-7 shows a comparison between the data and the derived hardening model. The blue line plots the effective mises true stress after yielding against the equivalent plastic strain calculated in equation (3.19). The orange line plots the relationship using the derived K and n for an internal pressure test at room temperature. The fit is adequate but not ideal.
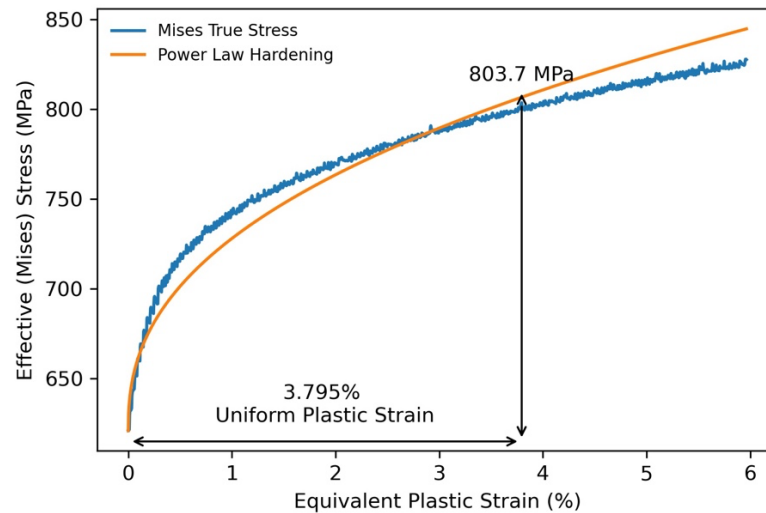
Figure 3-7 Hardening behavior from an internal pressure test at room temperature, K was equal to 716 MPa and n was equal to 0.413 in this test.

3.5 Results

Thirteen pressure tests and five full-tube tension tests were conducted according to the procedures described in section III with results shown in Table 3-1 and Table 3-2. Of the five full tube tension tests three were conducted at room temperature and two were conducted at 400 °C. Of the 13 pressure tests four were done at room temperature, two at 150 °C, three at 275 °C, three at 400 °C and one test at 525 °C. The tangential (θ) stress and effective stress at yielding are both reported for the internal pressure tests. For the single pressure test at 525 °C, the cladding displayed a yield drop softening behavior in which most of the plastic flow occurred below the maximum load making

calculation of the plasticity variables difficult using the methods described above. It is hypothesized that at this temperature and above visco-plastic effects begin to dominate the deformation.

Results are generally consistent at a given temperature with variability between the elastic and strength properties generally varying by less than 5%. The greatest variability is seen in the hardening data with as much as 16% variability in the hardening coefficient (K) and as much as 11% variability in the strain exponent (n). The fit of the power law hardening model to the data is acceptable (R^2 >95%) although the fit regularly underestimates yield and overestimates the hardening behavior, as seen in Figure 3-7. It has been suggested by other authors that there is an inherent randomness in the onset of plastic instabilities in unirradiated zirconium alloys [19][20]. This is explained by the anisotropic microstructure of the cladding tubes. The geometrically favored deformation system of the cladding's microstructure resists microplasticity until the critically resolved shear stress (CRSS) of a system is achieved, at which point plastic deformation may occur on all similar systems. The sudden activation of many similar slip systems will display a sharper yield shoulder than observed in more isotropic materials as well which can also be seen in Figure 3-7. More refined hardening models may be needed to account for this behavior and will be explored as part of future work.

Yield stress and ultimate tensile stress consistently decrease with temperature. Other mechanical property changes are most notable between 275 °C and 400 °C. Over this temperature range Young's modulus decreases from an average value of 84.5 GPa to an average value of 68.4 GPa. This is consistent with the expected 5% drop per 100 °C expected in HCP metals of the IV-B row in the periodic table [21]. The hardening coefficient likewise decreases from an average value of 655.3 MPa to 426 MPa. The decrease in the hardening coefficient with temperature is consistent with other correlations [20]. The ductility also begins to dramatically drop off in this temperature region with engineering uniform elongation in the tangential (θ) direction decreasing from 3.8% to 1.9%. For internal pressure loadings the uniform elongation in the tangential (θ) direction is very close to the true equivalent plastic strain, which is convenient for interpreting the results from these tests. However, care should be taken as this is not generically true. Under other stress ratios significantly higher contributions to the equivalent plastic strain can come from other strain components resulting in higher plastic strains (and thus higher wall stresses) at a similar tangential (θ) elongation.

Young's modulus, Poisson's ratio, yield stress, and ultimate tensile stress from the developed data set were compared with a variety of literature sources. Plots are shown in Figure 3-8, Figure 3-9, Figure 3-10, and Figure 3-11. When shown in these figures, data from axial tension tests are plotted as squares, data from ring tension tests are plotted as triangles, and data are plotted as dots when only

effective stresses are listed with no additional information on testing direction. For Young's modulus the data from both internal pressure and axial tension tests is in good agreement with literature from a large variety of sources [19][20][22][23][24][25][26][27][28] [29][30][31] [32][33][34][35], up to 400 °C. At 525 °C creep loci are likely being encountered very early in the internal pressure test and biasing the measurement of Young's modulus low. The data for Poisson's ratio is likewise in good agreement with a variety of sources at room temperature [19][23][24][25][33][26] and closely tracks data from Schwenk [36] up to 400 °C. Data is notably lower than values reported by Scott [31]. Few sources provide measured data points above 400 °C for comparison.
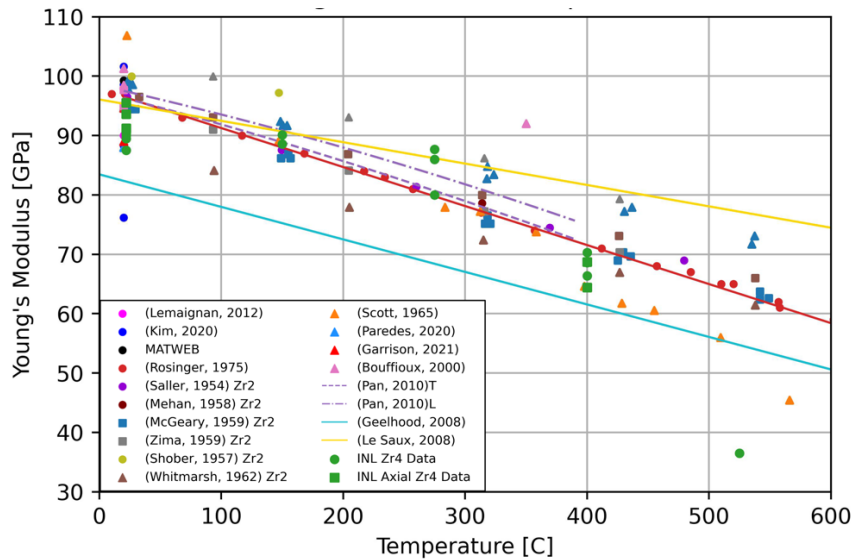
Figure 3-8 Comparison of Young's modulus data with literature.
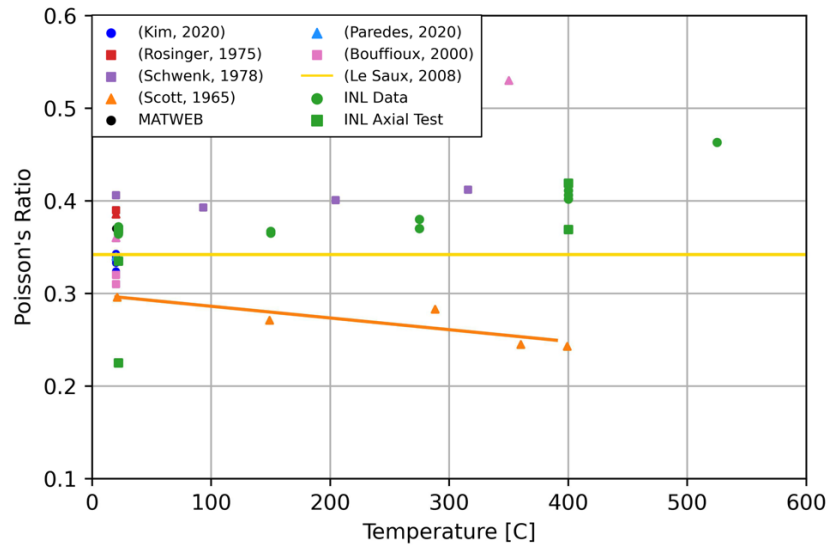
Figure 3-9 Comparison of poisson's ratio data with literature.

There is much greater variability among literature sources regarding measured yield stresses and ultimate tensile stresses. These strength values are much more sensitive to material processing parameters, such as the degree of cold work and final heat treatment as well as differing among the specific zirconium alloy being tested. With respect to yield stress, the values derived in this study fall within the wide range of reported values from room temperature studies [19][20][24][37][38][39][40] [41][42][43]. They also track well with data from Huang [44] and Tung [45] up to 400 °C. The ultimate tensile stress (UTS) values derived from this study tended to be generally higher than literature. It is unclear from many of the references if engineering or true stresses were used for the UTS which may account for some of the differences. Bouffioux et al. [33] explicitly use the true stress value corresponding to their UTS data which best matches the data in this study. Mozzani et al. [41] explicitly use engineering values for the yield stress and UTS data which agree well with other sources transposed by a constant stress factor from the true stress data at significant plastic strain.
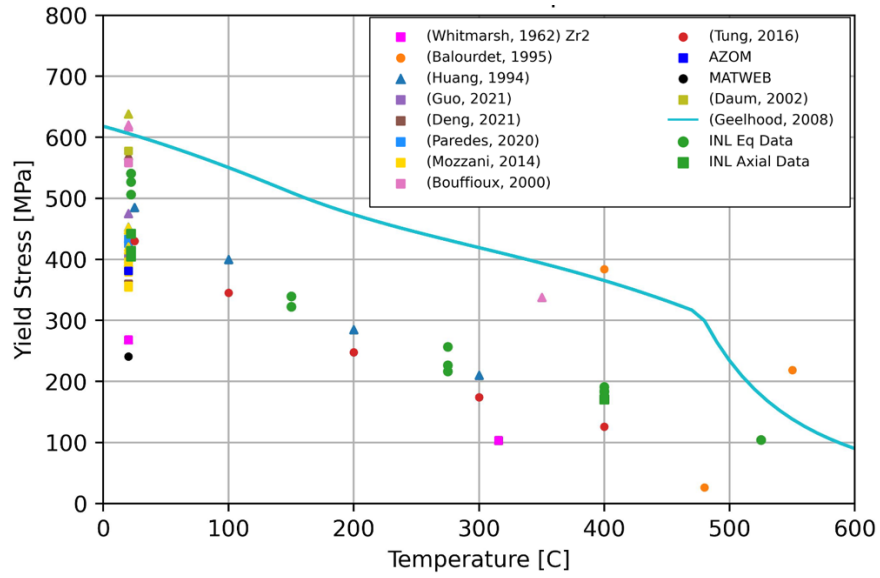
Figure 3-10 Comparison of yield stress data with literature.
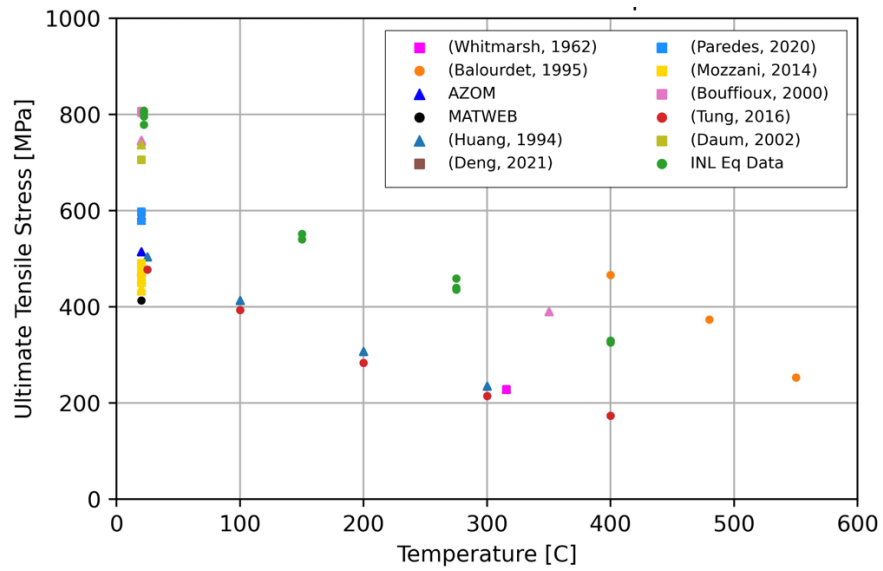
Figure 3-11 Comparison of ultimate tensile stress data with literature.

Table 3-1. Results from pressure tests

Stress at Yielding		Elastic Properties		Plastic Strain Ratios			Hardening Constants		Ductility Measures		Ultimate True Stress
$\sigma_{\theta,yield}$ (MPa)	$\sigma_{e,p,yield}$ (MPa)	E (GPa)	v	α	β	γ	K (MPa)	n	θ-UE (%)	Max ε^p (%)	Max σ_e (Mpa)
Room Temperature (~20 °C)											
624.5	540.8	89.5	0.366	-3.708	-1.369	0.369	559.2	0.392	4.58	4.631	795.5
608.5	526.9	87.5	0.372	-4.161	-1.316	0.316	758.7	0.412	4.54	4.661	808
624.6	540.9	90	0.368	-4.062	-1.327	0.327	716.7	0.413	3.7	3.795	803.7
584.4	506.1	90.4	0.364	-3.67	-1.375	0.375	595	0.373	5.05	5.102	778.6
150 °C											
372.4	322.5	90.1	0.365	-2.478	-1.677	0.677	579.6	0.386	4.4	4.331	540.3
391.9	339.4	88.6	0.367	-2.649	-1.607	0.607	589.4	0.383	2.79	2.788	551.1
275 °C											
261.8	226.8	87.7	0.37	-3.067	-1.484	0.484	736.5	0.422	4.15	4.152	435.2
250.2	216.7	80	0.38	-3.256	-1.443	0.443	691.2	0.389	3.95	3.994	439.4
296.7	256.9	86	0.37	-3.189	-1.457	0.457	538.2	0.358	3.4	3.352	458.9
400 °C											
210.9	182.7	66.4	0.411	-6.452	-1.183	0.183	428.1	0.355	1.96	2.139	328.3
213.1	184.5	68.6	0.402	-6.577	-1.179	0.179	387.5	0.322	1.89	2.057	329.7
220.3	190.8	70.3	0.406	-6.752	-1.174	0.174	463.1	0.404	1.91	2.058	325.3
525 °C											
120.5	104	36.5	0.463								

*θ-UE – Engineering Tangential Strain 'Elongation' Prior to Load Drop

**ε^p – True Equivalent Plastic Strain Prior to Load Drop

Table 3-2 Results from full tube tension tests

$\sigma_{Z,yield}$ (MPa)	E (GPa)	v	α
Room Temperature (~20 °C)			
442.1	91.2	0.369	-0.673
414.3	95.5	0.335	-0.681
404.5	93.6	0.225	-0.586
400 °C			
171.1	64.4	0.369	-0.673
170.2	68.7	0.419	-0.718

3.6 Derivation of Hill Coefficients and Yield Loci

The developed data set allow for the simultaneous solutions to Equations (3.8), (3.9), and (3.12) to calculate Hill anisotropic yield coefficients at room temperature and 400 °C. Figure 3-12 shows these coefficients along with the corresponding yield loci. The effect of the power law hardening can also be seen by the dashed blue line. For reference, the von Mises yield loci that would be calculated from a uniaxial axial tension test (green) and a ring tension test (magenta) are also shown for comparison. Data from previously conducted ring tension tests by the author is used to develop the yield loci in the figure for the tangential (θ) loading condition [46]. The derived curves show how applying data from uniaxial tests in either the tangential (θ) or axial (Z) direction would lead to an under calculation of tangential (θ) stresses and the importance of conducting multi-axial testing. Even if one does not fully develop a Hill yield criterion, using a von Mises criterion based on the effective yield stress in an internal pressure test provides a much more accurate calculation of wall stresses during multi-axial yielding as shown in the red curve.

The model predicts a maximum tangential (θ) stress when the axial (Z) to tangential (θ) stress ratio is 0.64. The derived Hill yield loci predicts a uniaxial tangential (θ) yield stress of 452.3 MPa. This closely matches the uniaxial data from ring tension testing data, which reported yield stresses of ~470 MPa [46]. The Hill yield model can be further cross validated by comparing the calculated plastic strain ratios for the axial tube tension test with those predicted by the model. Application of the plastic flow rule to Equation (3.6) and setting the radial and tangential stresses equal to zero results in Equation (3.21). Taking the derived room-temperature Hill coefficients for H and F result in a plastic strain ratio of -0.639, which is very close to the average of the measured values in the axial tension tests at room temperature of -0.647.

$$\frac{\epsilon_\theta^{p,Axial}}{\epsilon_z^{p,axial}} = \frac{-H}{F+H} \tag{3.21}$$

These numerous cross validations show that the internal pressure test is most useful in development of mechanical property data, and that it can be used to simulate PCI loading scenarios. At 400 °C, the tubing anisotropy is significantly reduced, and the Hill yield values all approach 0.5. The 400 °C Hill yield and von Mises yield loci for internal pressure and axial tensile data are shown in Figure 3-13. While axial tensile tests were not conducted at 150 °C or 275 °C, the plastic strain ratios developed from the internal pressure tests indicate that anisotropy is even higher at these intermediate temperatures than at room temperature. It is likely that the high flow stresses that develop at room temperature activate more twinning slip systems in the radially aligned basal poles. At 400 °C, slip system CRSS become more isotropic, and diffusion activated slip systems further allow for more deformation in the radial direction. However, stresses at intermediate temperatures are too low to activate twinning based systems and the temperatures too low to create any predominating diffusion processes [47]. It is theorized that at these intermediate temperatures and stresses that deformation is limited to dislocation-based slip on prismatic <a> systems and thus mechanical anisotropy due to grain texture is highest in these domains. Validating this hypothesis will be the subject of future work.
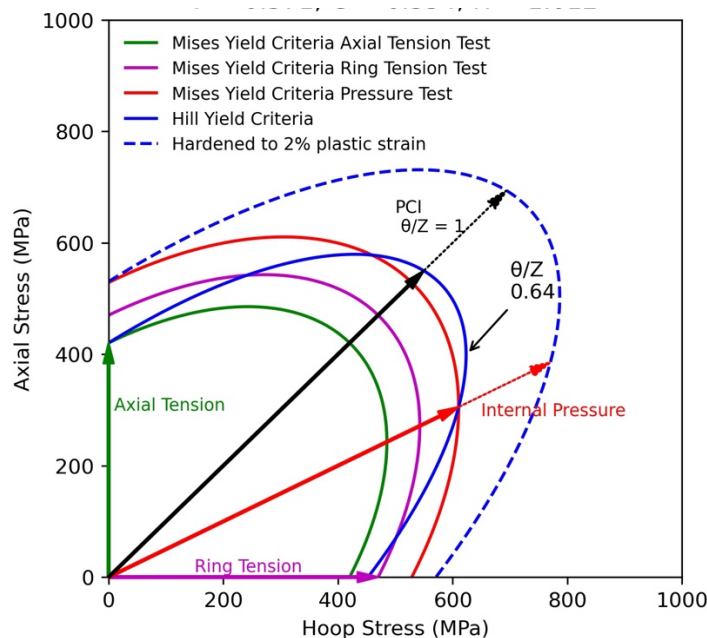
Figure 3-12 Yield loci from hill yielding criteria at room temperature; F=0.571, G=0.354, H=1.012.
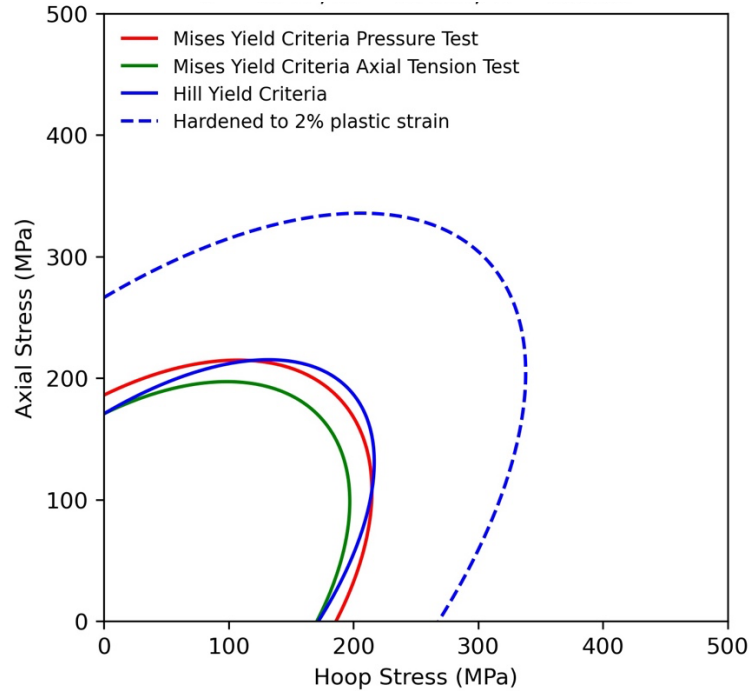
Figure 3-13 Yield loci from hill yielding criteria at 400 C; F=0.47, G=0.453, H=0.718.

The results of this study confirm that fresh, unirradiated and non-corroded (no hydrogen pickup) cladding has sufficient ductility to accommodate displacement-controlled loadings from an expanding fuel pellet. These results also indicate that if the deformation occurs at low temperature, such as in a cold zero-power transient, significant wall stresses can be generated for even modest tangential (θ) displacements. These stresses will likely be even higher if one considers strain rate [39] and irradiation hardening effects [48]. In claddings with a significant hydride flaw, these stresses may be high enough to initiate a cleavage-style crack [49]. As the cladding heats up, the stresses are relieved; however, if a flaw has already been initiated from a low-temperature stress fracture in a hydrided region, the limited amount of hardening that occurs past ~2% plastic strain in the bulk metal limits the ability of the crack to arrest. Even at low-engineering strains from PCI, local ductility can be quickly exhausted in these cases. This leads to the characteristic fracture surface seen in many fractured cladding tubes from overpower transient tests, which have a Mode I brittle crack in a heavily hydrided region, followed by a mixed Mode I/Mode II ductile crack propagating from the tip of the brittle flaw through the cladding thickness, ultimately resulting in failure [50].

3.7 Conclusions

It is concluded that the internal pressure test is capable of simulating displacement-controlled loadings and can generate a large set of useful mechanical property data on thin-walled zirconium alloy tubing up to 400 °C. When combined with full-tube axial tensile tests, the data from the internal pressure test can be used to derive Hill yield coefficients to develop a multi-axial elastic/plastic constitutive model of thin-walled tubing. The derived mechanical properties from the multi-axial loading experiments generally have low variability between tests and compare well with data derived from many literature sources. This validates the use of the test method to develop reliable data with a few tests. Texture induced mechanical anisotropy is identified at room temperature and appears to be minimized at high temperatures, in this case at 400 °C. However, the study provides some evidence that the mechanical anisotropy may be at a maximum around 150 °C or between 150 °C and 275 °C. The importance of conducting multi-axial loading experiments is emphasized as the developed yield loci showed that notably higher yield stresses are seen for thin-walled zirconium alloy metals under multi-axial loading than under uniaxial loading in either the axial (Z) or tangential (θ) directions. The developed yield loci are cross validated by comparing the plastic strain ratios from the full-tube tension tests and by comparing the predicted yield stress in the tangential di-rection with measured values from ring tension tests in a previous study.

3.8 References

1. E. Tenckhoff, "Review of Deformation Mechanisms, Texture, and Mechanical Anisotropy in Zirconium and Zirconium Base Alloys," ASTM Int., Vol. 2, (2005).

2. S. Banerjee "Nuclear Applications: Zirconium Alloys" Encyclopedia of Materials: Science and Technology, (2001).

3. M. Suzuki, H. Saitou, T. Fuketa "Analysis on pellet-clad mechanical interaction process of high burnup PWR fuel rods by RANNS code in reactivity-initiated accident conditions" Nuclear Technology, Vol. 155, (2006)

4. Nuclear Energy Agency, Nuclear Fuel Behavior Under Reactivity-initiated Accident Conditions State of the Art Report, NEA No. 6847, (2010).

5. Fuketa T. "Transient Response of LWR Fuels (RIA)" Comprehensive Nuclear Materials 2.22, (2012).

6. Hellouin de Menibus A., Auzoux Q., Monagabure P., Macdonald V., Le Jolu T., Besson J., Crepin J., "Fracture of Zircaloy-4 cladding tubes with or without hydride blisters in uniaxial to plane strain conditions with standard and optimized expansion due to compression tests" Materials Science and Engineering, Vol 604, (2014).

7. Shinozaki T., Udagawa Y., Mihara T., Sugiyama T., Amaya M., "Improved-EDC tests on the Zircaloy-4 cladding tube with an outer surface pre-crack" Journal of Nuclear Science and Technology, Vol 53, (2016).

8. Yueh K., Karlsson J., Stjarnsater J., Schirire D., Ledergerber G., Munoz-reja C., Hallstadius L., "Fuel cladding behavior under rapid loading conditions" Journal of Nuclear Materials, Vol. 469, (2016).

9. Yueh K., "Applicability of modified burst test data to reactivity initiated accident," Journal of Nuclear Materials, Vol 488, (2017).

10. Engineering ToolBox, (2005). Stress in Thin-Walled Cylinders or Tubes. [online] Available at: https://www.engineeringtoolbox.com/stress-thin-walled-tube-d_948.html [Accessed 1 Aug. 2022]

11. Mises, R. v.. "Mechanik der festen Körper im plastisch- deformablen Zustand." Nachrichten von der Gesellschaft der Wissenschaften zu Göttingen, Mathematisch-Physikalische Klasse, (1913): 582-592. http://eudml.org/doc/58894

12. Nagase, F., Fuketa, T., "Influence of Hydride Re-orientation on BWR Cladding Rupture under Accidental Conditions" *Journal of Nuclear Science and Technology* Vol 41 No 12 (2004)

13. Nagase, F., Fuketa, T., "Investigation of Hydride Rim Effect on Failure of Zircaloy-4 Cladding with Tube Burst Test" *Journal of Nuclear Science and Technology* Vol 42 No 1 (2005)

14. Lan, K-C., Chuang, C-P., Tung, H-M., Mo, K., Miao, Y., Liu, X., Lee, H., Park, J-S., Almer, J., Stubbins, J.F., "A study of the texture stability and the biaxial creep behavior of as-hydrided CWSR Zircaloy-4 cladding at the effective stresses from 55 MPa to 65 MPa and temperature from 300 °C to 400 °C" *Journal of Nuclear Materials* Vol. 564 (2022)

15. Seok, C-S., Bae, B-K., Koo, J-M., Murty, K.L., "The properties of the ring and burst creep of ZIRLO cladding" *Engineering Failure and Analysis* Vol 13 (2006)

16. Nguyen, D.V., Le Saux, M., Felebart, L., Brachet, J-C., Bonthonneau, J-C., Courcelle, A., Guillou, R., Rouesne, E., Urvoy, S., "Mechanical behavior of a chromium coating on a zirconium alloy substrate at room temperature" *Journal of Nuclear Materials* Vol 558 (2022)

17. Hill, R. "A theory of the yielding and plastic flow of anisotropic metals" *Proc R. Soc. Lond. A,* Vol. 193, (1948) http://doi.org/10/1098/rspa.1948.0045

18. *Standard Specification of Wrought Zirconium and Zirconium Alloy Seamless and Welded Tubes for Nuclar Service (Ecpet Nuclear Fuel Cladding)* ASTM B353-12(2022)e1

19. Paredes, M., and Wierzbicki, T. "On mechanical response of Zircaloy-4 under a wider range of stress states: From uniaxial tension to uniaxial compression." International Journal of Solids and Structures, Vol 206, (2020).

20. Geelhood, K. J., Beyer, C. E., and Luscher, W. G. *Stress/Strain Correlation for Zircaloy.* PNNL-17700. (2008).

21. Fisher E.S., Renken C.J. "Single-Crystal Elastic Moduli and the hcp -> bcc Transformation in Ti Zr and Hf" *Physical Review* Vol 135 (1964)

22. Lemaignan, C. "Zirconium alloys: Properties and characteristics," Comprehensive Nuclear Materials (2012).

23. Kim, H., Lee, Y., Kim, I., Kim, H., and Kim, D. "On the method to obtain the elastic properties using a pressurized thin tube," Engineering Failure Analysis, (2020).

24. MatWeb. Zircaloy-4 Zirconium Alloy. https://www.matweb.com/search/DataSheet.aspx?MatGUID=e36a9590eb5945de94d89a35097b7faa, (2022).

25. Rosinger, H., Ritchie, I., and Shillinglaw, A. "Young's Modulus of Crystal Bar Zirconium and Zirconium Alloys [Zircaloy-2, Zircaloy-4, Zirconium-2.5wt% Niobium] to 1000K." Whitesheil Nuclear Research Establishment, (1975).

26. Saller, H. A., Dickerson, R. F., and Foster, E. L. Induction-Melted Zirconium and Zirconium Alloys. BMI-908, (1954).

27. Mehan, R. L. Modulus of Elasticity of Zircaloy-2 Between Room Temperature and 1000°F. KAPL-M-RLM-16, (1958).

28. McGeary, R. K., and Lustman, B. "Preferred Orientation in Zirconium," Trans. AIMME, 191. (1959) 994-1002.

29. Zima, G. E. A Review of The Properties of Zircaloy-2, (1959).

30. Shober, F. R., Al, E., and Al., E. The Mechanical Properties of Zirconium and Zircaloy-2. BMI-1168 (1957).

31. Scott, P. B. Physical and Mechanical Properties of Zircaloy -2 and -4, Vol. 3269, (1965).

32. Garrison, B., Yan, Y., and TerMaath, S. "Determining failure properties of as-received and hydrided unirradiated Zircaloy-4 from ring compression tests." Engineering Failure Analysis, Vol. 125, (2021).

33. Bouffioux, P., and Rupa, N. "Impact of Hydrogen on Plasticity and Creep of Unirradiated Zircaloy-4 Cladding Tubes." Zirconium in the Nuclear Industry: Twelfth International Symposium, 399–420, (2000).

34. Pan, Z., Wang, N., and He, Z. "Measurements of Elastic Modulus in Zr Alloys for Candu Applications." 11th International Conference on CANDU Fuel, CW-128700-CONF-001, (2010).

35. Le Saux, M., Besson, J., Carassou, S., Poussard, C., and Averty, X. "A model to describe the anisotropic viscoplastic mechanical behavior of fresh and irradiated Zircaloy-4 fuel claddings under RIA loading conditions". Journal of Nuclear Materials, Vol 378, (2008).

36. Schwenk, E. B., Wheeler, K. R., Shearer, G. D., and Webster, R. T. "Poisson's ratio in zircaloy-4 between 24° and 316°C," Journal of Nuclear Materials, Vol 73, (1978).

37. Whitmarsh, C. L. Review of Zircaloy-2 and Zircaloy-4 Properties Relevant to N.S. Savannah Reactor Design. ORNL-3281, (1962).

38. Balourdet, M., and Bernaudat, C. Tensile Properties of Irradiated Zircaloy 4 Cladding Submitted to Fast Transient Loading. Proceedings of the CSNI Specialist Meeting, (1995).

39. Guo, W., Li, G., Yuan, F., Han, F., Zhang, Y., Ali, M., Ren, J., and Yuan, G. "Texture development and mechanical behavior of Zircaloy-4 alloy plates fabricated by cold rolling and annealing." Materials Science and Engineering, Vol. 807, (2021).

40. Deng, S., Song, H., Liu, H., and Zhang, S. H. "Effect of uniaxial loading direction on mechanical responses and texture evolution in cold pilgered Zircaloy-4 tube: Experiments and modeling." International Journal of Solids and Structures, vol. 213, (2021).

41. Mozzani, N., Auzoux, Q., Le Boulch, D., Andrieu, E., Blanc, C., Scott, C. P., and Barnel, N. "Mechanical behavior of recrystallized Zircaloy-4 under monotonic loading at room temperature: Tests and simplified anisotropic modeling." Journal of Nuclear Materials, Vol. 447, (2014).

42. AZOMaterials. Zircaloy-4(Alloy Zr4) (UNS R60804). https://www.azom.com/article.aspx?ArticleID=7644, (2022).

43. Daum, R. S., Majumdar, S., Tsai, H., Bray, T. S., Koss, D. A., Motta, A. T., and Billone, M. C. "Mechanical Property Testing of Irradiated Zircaloy Cladding Under Reactor Transient Conditions." ASTM Special Technical Publication, Small Spec, (2002).

44. Huang, J. H., and Huang, S. P. "Effect of hydrogen contents on the mechanical properties of Zircaloy-4." Journal of Nuclear Materials, Vol. 208, (1994).

45. Tung, H. M., Chen, T. C., and Tseng, C. C. "Effects of hydrogen contents on the mechanical properties of Zircaloy-4 sheets." Materials Science and Engineering, Vol 659, (2016).

46. Kamerman D., Cappia F., Wheeler K., Petersen P., Rosvall E., Dabney T., Yeom H., Sridharan K., Sevecek M., Schulthess J., "Development of axial and ring hoop tension testing methods for nuclear fuel cladding tubes" Nuclear Materials and Energy, Vol 31, (2022).

47. Hayes, T.A., Kassner, M.E. Creep of zirconium and zirconium alloys. Metal Mater Trans A, Vol 37, 2389–2396 (2006). https://doi.org/10.1007/BF02586213

48. Griffiths M. "A review of microstructure evolution in zirconium alloys during irradiation" *Journal of Nuclear Materials* Vol 159, (1988)

49. Daum R. S., Hydride-Induced Embrittlement of Zircaloy-4 Cladding Under Plane-Strain Tension A Thesis in Materials Science, The Pennsylvania State University (2007)

50. Raynaud P.A., Koss D.A., Motta A.T., "Crack growth in the through-thickness direction of hydrided thin-wall Zircaloy sheet" Journal of Nuclear Science and Engineering, Vol. 420 (2012)

Chapter 4: Formation and Characterization of Hydride Rim Structures in Zircaloy-4 Nuclear Fuel Cladding Tubes

David Kamerman, Mukesh Bachhav, Tiankai Yao, Xiaofei Pu, Jatuporn Burns

Abstract

Zirconium alloy tubes used as nuclear fuel cladding are subject to oxidation and subsequent hydrogen pickup during their long service in commercial light water reactors. The hydrogen picked up in the cladding can precipitate as a brittle hydride rim feature on the claddings outer surface. To better understand the effect of hydride rims on the fracture behavior of stress-relieved zirconium alloy cladding tubes, a procedure to produce these rim-like structures has been developed and is described herein. Extensive characterization of the 'as hydrided' tubes is performed.

The hydrogen charging apparatus consists of a tube furnace with a quartz chamber that is connected to a vacuum pump as well as a bottle of pure hydrogen gas. The charging station uses a static charge of hydrogen as opposed to a flowing gas. The chief advantage of this approach is the ability to monitor the pressure drop in the hydriding chamber and correlate this pressure drop to a known rate of hydrogen pickup in the cladding tube. It was found that the hydrogen partial pressure, metal temperature, and surface treatment all clearly played a role in whether a hydride rim was formed. Extensive characterization the hydride rims shows they consist of needle like platelets of phase hydrides (ZrH1.6) oriented in the circumferential direction with a radial spacing of several microns in a sandwich-like structure.

4.1 Background and Motivation

Zirconium alloy tubes used as nuclear fuel cladding are subject to oxidation and subsequent hydrogen pickup during their long service in commercial light water reactors. Hydrogen has low solid solubility in zirconium and usually precipitates as brittle zirconium hydride platelets in the cladding metal matrix. It is the precipitation of these hydride platelets that most influences the mechanical integrity of the cladding tubes, often to a much greater extent than the formation of the oxide layer [1] or even the irradiation damage of the cladding [2]. Due to temperature-driven diffusion (Soret effect) and the grain texture of stress-relieved zirconium metal tubes, hydrides often precipitate with a circumferential orientation near the outer surface of the cladding tubes forming a hydride rim, as depicted in Figure 4-1. It is these dense formations of hydrides near the cladding's outer diameter, which can serve as a site for crack initiation during tangential loadings of the cladding during pellet cladding interaction [3][4]. The dominate hydride phase present in these hydride rims is the δ-Hydride phase (face centered cubic $ZrH_{1.6-1.7}$) with other tetragonal phases only present at very high hydrogen concentrations [5]. To better understand the effect of hydride rims on the fracture behavior of stress-relieved zirconium alloy cladding tubes, a procedure to produce these rim-like structures has been developed and is described herein. Extensive characterization of the 'as hydrided' tubes is performed to determine variability in the hydriding method, verify the presence of a sandwich-like rim region, and identify the phase of the hydrides that formed.

The conditions under which hydride rim structures form in commercial light water reactors are difficult to replicate in a laboratory setting. Generating rim structures based on aqueous corrosion and Soret diffusion would require very long exposure times in autoclaves and a complex experimental setup with a heat source inside the cladding tubes. An alternative method using a gaseous diffusion technique for hydrogen charging has been employed previously by a variety of institutions. These methods generally involve exposing a cleaned cladding tube to partial pressures of hydrogen gas (often in the form of H/Ar mixtures) at elevated temperatures between 300°C and 400°C [6,7]. These hydrogen charging apparatuses generally employ a flowing gas at constant pressure and result in a uniform distribution of hydride platelets through the cladding thickness without any notable rim, which is shown in the left-hand side of Figure 4-1. Hellouin de Menibus, et al. developed a technique for forming a hydride blister on cladding tubes by bringing a cold finger into proximity with the cladding tube during hydrogen charging [8]. Hydride blisters are like hydride rims in that both are embrittling features in the metal cladding tubes. However, hydride rims are generally characterized by sandwich-like structures of alternating hydride and metal layers while hydride blisters consist of a thick, bulk hydride phase. Additionally, hydride blisters often have a sunburst pattern of hydrides

beneath the bulk formation. While hydride blisters can form in nuclear fuel cladding tubes after the spallation of heavy oxide layers, their presence is less common than hydride rims and is generally mitigated by limiting oxide layer thickness to less than 100 μm [9].

| Hydride Rim | Uniform Hydrides | Hydride Blister 'Sunburst' |
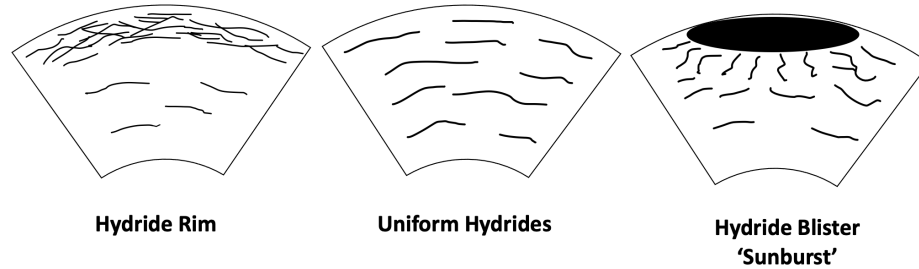
Figure 4-1 Hydride features which form in stress-relieved zirconium alloy cladding tubes.

To create a hydride rim via gaseous diffusion, a supersaturation of dissolved hydrogen would need to be present near the outer surface of the cladding so that the driving force for precipitation is as high as possible. The rate of hydride precipitation in zirconium was studied by Marino, et al. [10] who proposed that the rate of hydride formation could be described by the *Equation (1)*:

$$\frac{dC_{hydride}}{dt} = \alpha^2 (C_{disolved\ hydrogen} - TSS_p) \tag{4.1}$$

Where α is a kinetics parameter, C represents the concentration of hydrides and dissolved hydrogen, respectively, and TSSp is the terminal solid solubility (for precipitation) of hydrogen in zirconium. Both the kinetics parameter α and TSSp follow Arrhenius relationships, which have been developed by Kammenzind [11] and McMinn [12], respectively. The activation energy for TSSp is smaller than α; thus as temperature increases, the driving force for precipitation will decrease for a given concentration of dissolved hydrogen. The diffusion coefficient of hydrogen in zirconium also follows an Arrhenius relationship. These relationships indicate that as the metal temperatures increase, hydrogen will more readily diffuse through the thickness of the cladding, hindering rim formation [13].

Apart from increasing the cladding temperature, the rate of hydrogen uptake can theoretically be increased by increasing the partial pressure of the hydrogen gas surrounding the cladding, as done by Kudiiarov, et al [14]. The hydrogen concentration in the metal is related to the square root of the partial gas pressure, according to Sievert's law, which is valid for zirconium metals and hydrogen [15]. Additionally, increasing the rate of hydrogen uptake can be achieved by increasing sample

surface area via roughening of the surface, which has been shown by Shimskey, et al. [16] as a successful way to form hydride rims in stress-relieved zirconium metal cladding. An additional consideration in the preparation of zirconium metal cladding tubes for hydrogen charging is the presence of native oxide layers on the metal surface. Hydrogen is insoluble in zirconium oxide, making the oxide layer an effective barrier to hydrogen uptake. Even after careful cleaning of the zirconium tubes, thin oxide layers (5–10 nm) will be present on the surface. To break down these oxide layers in a reasonable time interval, the cladding surface temperature must be elevated in an oxygen-deprived environment [17]. The minimum temperature (and time at temperature) for oxide layer breakdown depends on the starting condition of the oxide layer, the concentration of oxidizing agents in the gas surrounding the cladding, and the surface conditions of the oxide metal interface [18].

4.2 Materials and Methods

To effectively create a hydride rim structure via gaseous diffusion, a sufficiently high metal temperature must be reached to promote native oxide layer breakdown and hydrogen absorption into the metal. However, as the physics described above suggest, too high of a temperature will promote a uniform distribution of hydrides in the cladding tubes and inhibit rim formation. Thus, it is expedient to conduct the hydrogen charging at as low of a temperature as possible to keep the rate of hydride formation as high as possible. It is also theorized that too high of a hydride formation rate will result in a hydride blister rather than a hydride rim, and this must be avoided also. In addition to temperature, it is beneficial to keep the concentration of oxidizing agents in the hydriding chamber as low as possible and to keep the concentration of hydrogen gas in the hydriding chamber as high as possible. Careful attention must be paid to the surface preparation of the cladding tubes prior to hydriding. Several such surface preparation strategies are explored as part of the present study.

The hydrogen charging apparatus consists of a 34-cm-long tube furnace with a quartz tube insert that is connected to a vacuum pump as well as a bottle of 99.9% pure hydrogen gas. A single feed through in the quartz tube on the opposite end of the furnace allows a thermocouple to track the temperature in the center of the cladding tube when positioned in the furnace. Nuclear grade stress-relieved Zircaloy-4 cladding tubes with standard 17x17 dimensions (i.e., 9.5 mm OD, 0.57 mm wall thickness) of 20 cm length are used in the present study. These tubes were commercially procured and conform to ASTM B353-12 [19]. Charging cladding tubes of 20 cm length will enable the generation of test specimens for more integral style mechanical tests, such as burst testing [20], expansion due to compression testing [21], modified burst testing [22], and even integral transient testing [23], to take place. Variation in the hydrogen concentration and rim thickness is expected across the length of the

cladding tube. However, it is beneficial for the center 10 cm section of the charged tube be relatively uniform. Figure 4-2 depicts a diagram of the hydrogen charging apparatus and a characterization of temperature uniformity across the length of the furnace at 290°C, 340°C, and 400°C. Temperature uniformity is important to maintain uniform hydriding conditions. Minimal temperature variation is present in the center 20 cm of the furnace (± 10°C). This variation is reduced even further in the center 10 cm zone of the furnace (± 3°C).
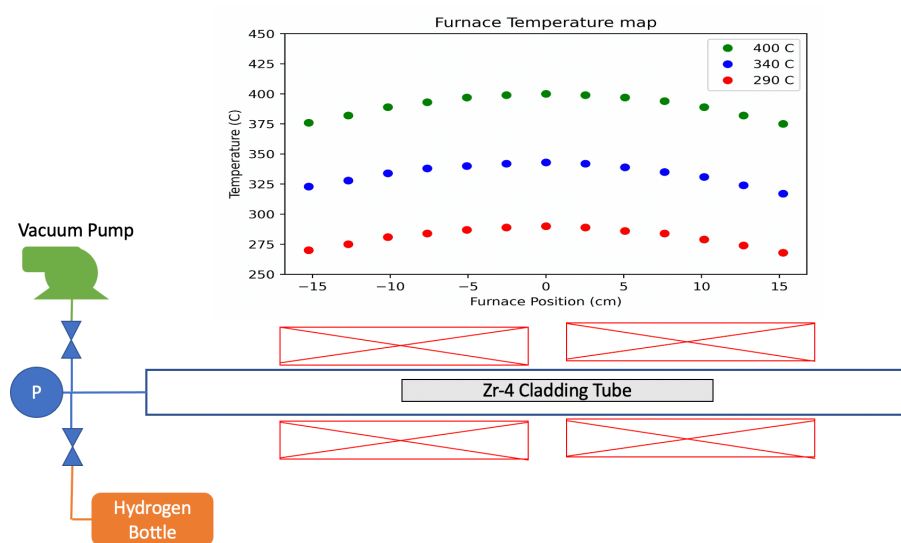
Figure 4-2 Schematic and temperature calibration of gaseous hydriding furnace.

The hydrogen charging procedure involves first placing the cladding sample in the quartz tube along with the temperature monitoring thermocouple. The vacuum pump is then turned on for a duration of 10–30 minutes until a vacuum pressure of 2e-9 psia is achieved in the system. Contrary to most hydrogen charging apparatuses described in the literature, this charging method uses a static charge of hydrogen in the quartz tube as opposed to a flowing gas. The hydrogen gas is an ultra-high purity, 99.99% gas. The chief advantage of this approach is the ability to monitor the pressure drop in the hydriding chamber and correlate this pressure drop to a known rate of hydrogen pickup in the cladding tube. A drawback of the static hydrogen charging approach is that as the hydrogen is absorbed into the cladding the hydrogen, partial pressure driving further hydrogen uptake is reduced, thus slowing the absorption rate. Initial hydrogen charges of 4–8 psia were used in the subject study. The hydriding chamber is then isolated from both the hydrogen supply and vacuum pump. The furnace performs a 4°C/s temperature ramp to a terminal temperature between 290°C and 400°C. Hydriding durations varied from 3 hours to over 120 hours, depending on the rate of hydrogen

uptake. A time-dependent cladding average hydrogen concentration was determined by using the time varying pressure and temperature of the hydriding chamber and applying the ideal gas law, assuming a constant volume of the hydriding chamber and conserving the hydrogen mass. The correlation assumes that a temperature-corrected change in pressure in the hydriding chamber corresponds to a change in the hydrogen concentration in the cladding tube. Figure 4-3 demonstrates how the cladding temperature (blue) and chamber pressure (red) change over the course of a successful hydriding run. Figure 4-3 also plots the evaluated cladding average hydrogen concentration (green).
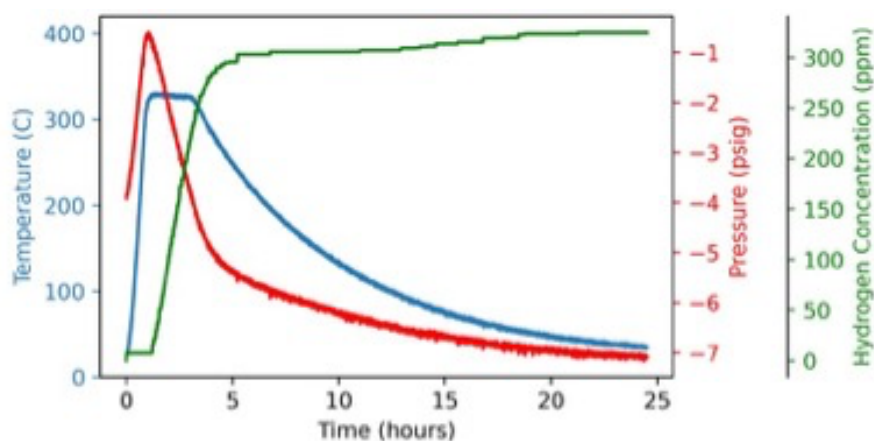
Figure 4-3 Temperature, pressure, and evaluated hydrogen concentration in a successful hydriding run.

An initial series of 16 tests were performed to identify the most promising conditions for further development (labeled 001–016). This test matrix is shown in Table 4-1. The initial series of tests explored different surface treatments, different initial hydrogen charges, and different hydriding temperatures. It was postulated that smooth surfaces with thick oxide layers would prohibit hydrogen uptake while rough surfaces with very thin oxide layers would promote hydrogen uptake. It was desired to only create hydride rims on the outer surface of the cladding so efforts, such as cleaning, manual grinding, and sandblasting, were used on the outer surface of the cladding only. The inner surface was either left alone or an oxide layer was grown on the cladding surface by exposing the sample to air in a 400°C oven for 24 hours before preparation of the outer surface and subsequent hydriding.

Following the hydrogen charging, the cladding tubes were sectioned into analytical chemistry specimens, metallographic specimens, and mechanical test specimens, according to the sectioning diagram shown in Figure 4-4. Analytical measurements of the total cladding hydrogen concentration

are made using an inert gas fusion technique. Metallography sections are used to confirm the presence and thickness of any hydride rim features present in the cladding. The hydride structures are characterized in optical microscopy via an etchant, which often does not provide enough resolution to confirm the presence of the sandwich-like structure in the rim region. To elucidate microstructure, chemistry, and hydride phases present in the rim structure, additional characterization was performed using scanning electron microscopy (SEM), X-ray diffraction (XRD), atom probe tomography (APT), and transmission electron microscopy (TEM). The mechanical testing specimens are saved for future testing.
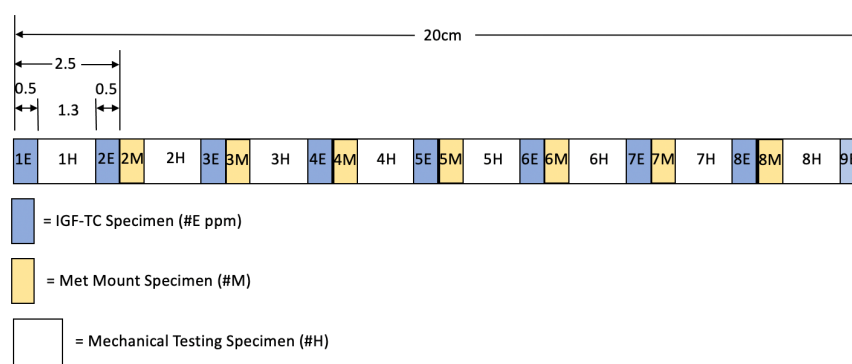
Figure 4-4 Sectioning diagram of hydrided cladding tubes.

Surface imaging on a sample from the middle of hydride Test E was performed using Tescan Lyra3 gallium focused ion SEM. Images were collected using a back scattered mode to reveal surface microstructure and capture z contrast. XRD analysis was conducted on a Panalytical Empyrean X-ray Diffractometer. The XRD analyses was conducted using the Bragg-Brentano geometry, with a Cu Kα X-ray beam at 45 kV and 40 mA, and a PIXEL-3D detector. The sample was loaded onto a zero-background plate to reduce the interference from the background. The measured 2-theta angle ranged from 10–140 degrees. The scanning step size was 0.026 degrees, with the counting time of 200 seconds per step, in continuous scan mode. The total scanning time was about 66 minutes for each sample. A smaller slit (with ~3mm width being diffracted from the sample) was used on the diffraction beam side to ensure the diffracted region was mostly focused on the sample, due to the presence of a prominent phase (calcium carbonate) in the epoxy.

APT needles were prepared using a conventional dual beam lift-out process in a Tescan Lyra3 instrument with a gallium (Ga) beam. A two-step method was used to make APT needles. The bulk lift-outs with wedge-shaped geometry were mounted, and platinum was welded on the silicon

post at room temperature. Final milling of tips with end radius less than 100 nm was performed at liquid nitrogen temperature to avoid H diffusion and artificial formation of hydrides. Lift-outs were prepared across dendrite structure to elucidate both hydride and matrix Zr-4 regions. Figure 4-5 shows a 3D reconstructed tip prepared from Zr 4 region along the grain boundary, indicating a slight segregation of Al impurities and depletion of Sn.
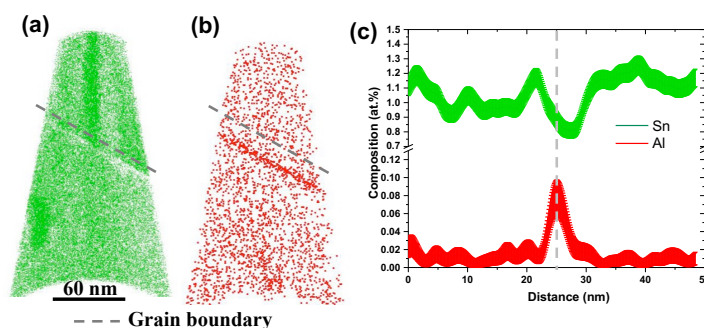
Figure 4-5 APT Specimen prepared from Zr-4 matrix along the grain boundary.

Specimen for TEM analysis were prepared on Tescan Lyra3 dual beam FIB using a Ga beam with a size ~10 by 10 μm2. To avoid hydride formation due to Ga ions, bulk lift was prepared at room temperature followed by thinning at liquid nitrogen temperature (-180°C), similar to the APT needles. Thinning samples at low temperatures has proven be an effective method to avoid H penetration and formation of ZrH. This approach allows the distinction between real ZrH due hydriding process and artifact ZrH. Scanning TEM (STEM) characterization was carried out on a ThermoFisher Titan Themis G2 200 probe corrected TEM. The STEM was operated at an acceleration voltage of 200 KeV. Energy-dispersive X-ray spectroscopy (EDS) signals were collected using a high-sensitivity SDD X-ray spectrometer (Super-X) system. Bright field (BF) image and high-angle annular dark field (ADF) imaging techniques were used to reveal the morphology of hydrides and selected area diffraction patterns indexing to reveal crystal structure.

4.3   Results and Discussion

Test 001 with inner and outer surfaces cleaned was hydrided at 290°C. The test resulted in evidence of hydride rim formation; however, this feature was on both the cladding inner surface and the cladding outer surface, as seen in Figure 4-6(a). Subsequent tests (002 and 003) at 400°C showed a uniform distribution of hydrides with no rim present on either the inner or outer diameter. Test 004 attempted to repeat the success of Test 001 but sought to inhibit the formation of the rim on the inner surface by not cleaning the inner surface. The test did not result in any hydrogen uptake. It was

theorized that the 290°C hydriding temperature was too low to achieve repeatable results and the hydriding temperature was increased to 350°C in Test 005. This test was also unsuccessful in forming a hydride rim as a uniform distribution of hydrides was formed instead Figure 4-6(b). It was speculated that the hydriding temperature was either too high or the cladding spent too long of a time at the elevated temperature. For Test 006 a sandblasting surface treatment was applied to the cladding outer surface to determine if a significant increase in surface roughness could improve the hydrogen absorption sufficiently on the outer surface to form a hydride rim. The surface treatment resulted in a very high hydrogen absorption rate; however, the observed feature in the metallographic image Figure 4-6(c) appeared to resemble a bulk hydride feature like a blister rather than a sandwich-like rim structure.
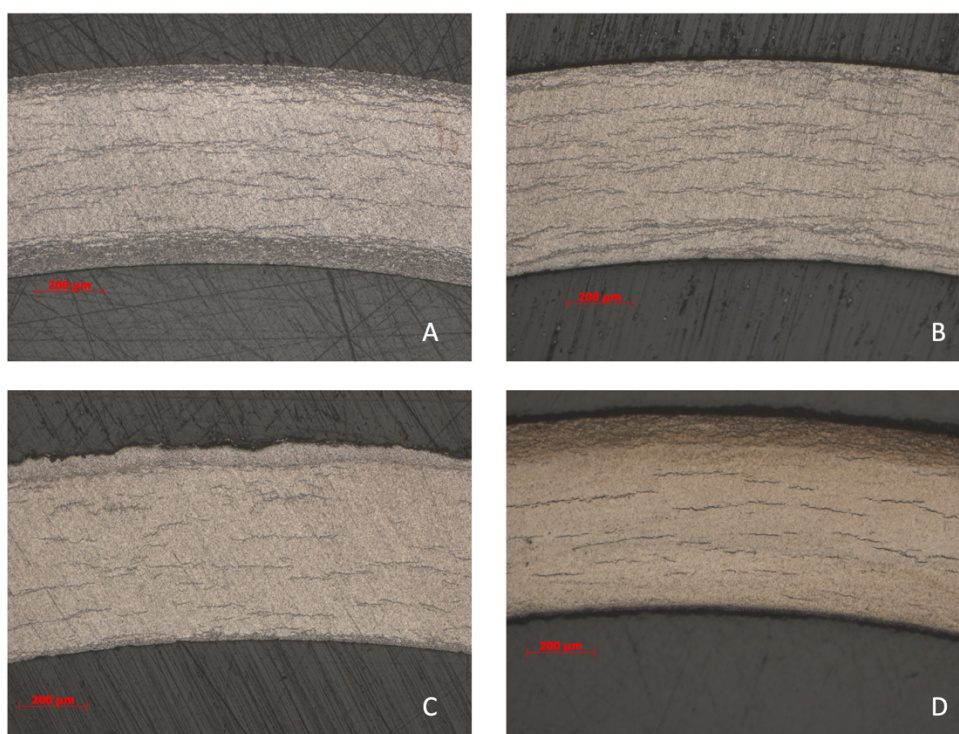
Figure 4-6 Optical micrograph showing hydride features on (a) Test 001, (b) Test 005, (c) Test 006, and (d) Test 012.

Test 007 was also sandblasted but the hydriding took place at the lower 290°C temperature. The hope was that this combination of surface roughness and temperature would slow the hydrogen absorption rate sufficiently to favor rim formation. However, no hydrogen was absorbed, and no hydride features were formed, again casting doubt on the viability of hydriding tubes at 290°C. Test 008 attempted to form a hydride rim by applying a second, fresh charge of hydrogen gas to the hydriding chamber in the middle of a 350°C hydriding run, which was unsuccessful and resulted in a

uniform distribution of hydrides. Test 009 explored the use of a chemical etch to the outer surface to promote hydrogen uptake; although, this had the opposite effect and resulted in a hydride feature forming on the inner diameter of the cladding but not the outer diameter. Test 010 and Test 011 again attempted to hydride tubes at 290°C; both tests resulted in negligible hydrogen pickup.

Starting with test 012, a new sample preparation treatment was deployed. This involved exposing the sample to air in a 400°C oven for 24 hours to grow oxide layers on both the inner and outer surfaces. The oxide layer on the outer surface was then removed by hand sanding, which results in a slightly rough surface on the outer surface yet significantly less rough than the sandblasted samples. Two tests (012 and 013) resulted in successful hydride rim formation when hydrided at 290°C with hydride rims present on the outer surface only, as shown in Figure 4-6(d). Test 014 attempted a third repeat of these success but after four hours, very little hydrogen was being absorbed. Thus, in this test, it was decided to raise the temperature briefly to 350°C before again cooling down to 290°C for most of the hydriding run. This procedure was repeated for tests 015 and 016. The procedure was successful in Tests 014 and 016 but not in Test 015.

Table 4-1 Summary results of initial hydriding trials.

Test Number	Outer Surface Preparation	Inner Surface Preparation	Hydrogen Charge (psig)	Hydriding Temperature (°C)	Result
001	Clean	Clean	-6.92	290	Rim Both Surfaces
002	Clean	Clean	-6.93	400	Uniform
003	Clean	Clean	-6.96	400	Uniform
004	Clean	Nothing	-6.91	290	No Absorption
005	Clean	Nothing	-7.08	350	Uniform
006	Sand Blast	Nothing	-6.84	350	Blister
007	Sand Blast	Nothing	-6.99	290	No Absorption
008	Clean	Nothing	-6.88, & -2.20	350	Uniform
009	Chemical Etch	Nothing	-6.93	350	Rim Inner Surface
010	Clean	Nothing	-6.97, & -1.97	290	No Absorption
011	Chemical Etch	Nothing	-6.84	290	No Absorption
012	Sandpaper	Oxidized	-6.95	290	Rim Outer Surface
013	Sandpaper	Oxidized	-3.96	290	Rim Outer Surface
014	Sandpaper	Oxidized	-3.88	350 & 290	Rim Outer Surface
015	Sandpaper	Oxidized	-3.90	350 & 290	No Absorption
016	Sandpaper	Oxidized	-3.90	350 & 290	Rim Outer Surface

Figure 4-7 shows the results of all the preliminary tests. The x-axis shows the hydriding temperature, and the y-axis shows the rate of hydrogen absorption (as determined by the time taken for a 4-psi pressure drop) and the total time at temperature. If the hydrogen absorption rate is slow or the sample spends too much time at temperature, rim formation is inhibited in favor of a more uniform hydrogen distribution. From these initial experiments, surface preparation was determined to be the key variable in controlling the rate of hydrogen absorption.
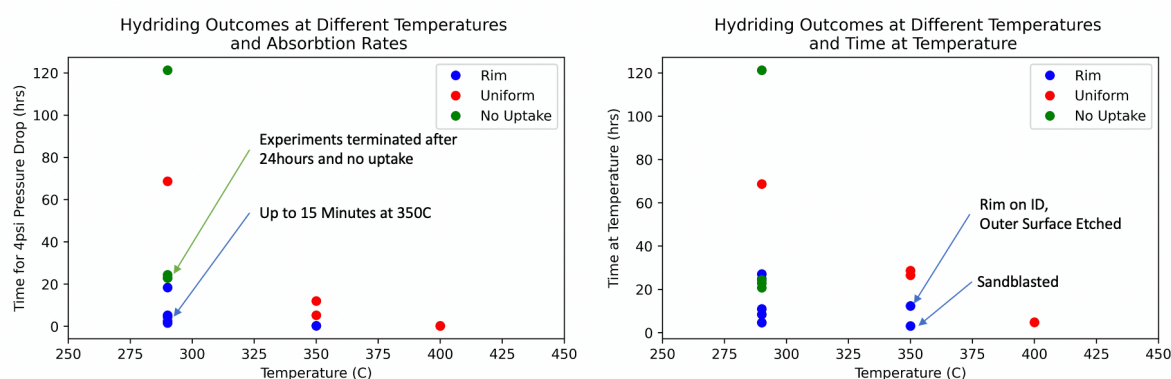
Figure 4-7 Initial results plotted against temperature and absorption rate (left). Initial results plotted against temperature and total time at temperature (right).

4.3.1 Variability in Hydride Rim Formation

From an evaluation of the initial results, it was decided to proceed with a standardized hydriding temperature of 330°C, which was theorized to be high enough to promote hydrogen absorption with the chosen sample preparation method but low enough to promote a sufficiently high driving potential for hydride precipitation and, thus, rim formation. Six successive cladding tubes (labeled A–F in Figure 4-8) were successfully hydrided with this procedure and all showed evidence of hydride rims on the outer surface of the cladding and none on the inner surface. The variability in observed rim thickness was determined by taking 16 measurements of the rim thickness at different azimuthal locations on the metallography samples. Error bars in Figure 4-8 indicate a mean and two standard deviations in rim thickness measurements for each axial location of the cladding tube for each of the six successful hydriding runs. In general, variation in rim thickness azimuthally bounds variation in rim thickness axially, particularly in the center 10 cm section of the cladding tube. Figure 4-8 also shows the hydrogen concentration results of the inert gas fusion measurements along with the evaluated cladding average amount from an analysis of the hydriding temperature pressure data.

Regions with higher hydrogen concentration generally also show a thicker hydride rim. Hydrogen concentrations tend to be between 300 wppm and 700 wppm, and rim thickness tends to be between 60 μm and 100 μm. The largest variations tend to be between different tubes. Even though the hydriding procedures were identical, some of the cladding tubes absorbed much more hydrogen gas more quickly than others. A general trend is that cladding tubes that absorbed more hydrogen quicker had higher rim thicknesses but also higher variability in rim thickness measurements, while tests with a slower and smaller hydrogen uptake had more stable values of hydrogen concentration and rim thickness across the cladding length.
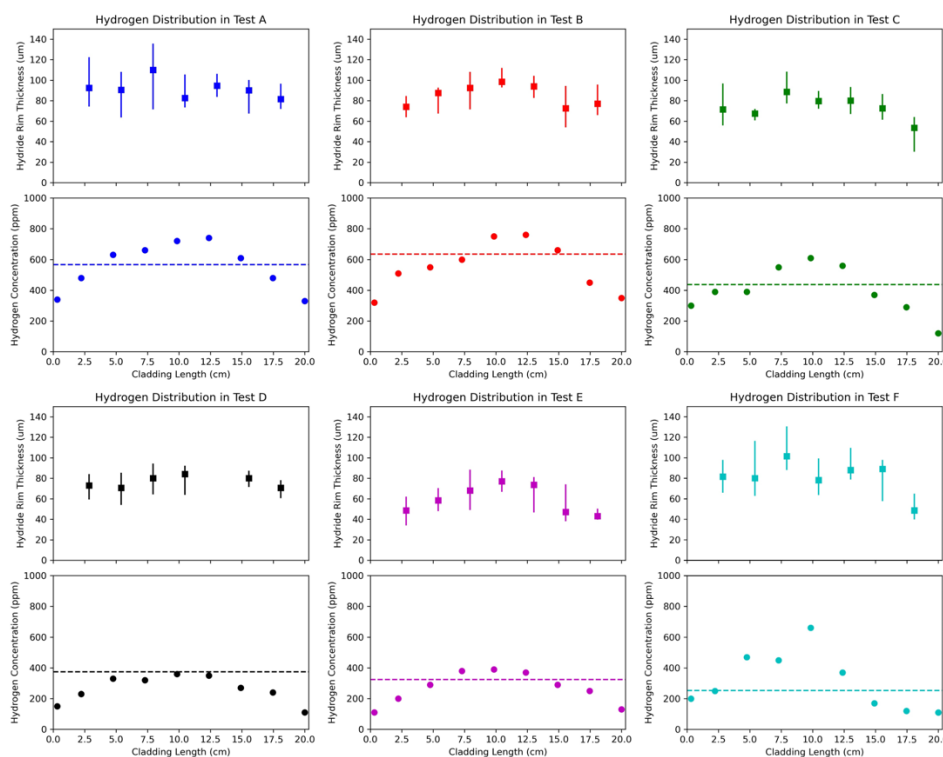
Figure 4-8 Variability in rim thickness and hydrogen concentration in six hydrided tubes with hydride rims.

4.3.2 Detailed Characterization of Hydride Rim Features

Backscatter SEM images of the rim region showed evidence of distinct hydride structures embedded in a metal matrix as indicated by the red arrows in Figure 4-9. Within the rim region, it was seen that the spacing between the hydride strings varied from just a few microns to ~10 μm, as seen in Figure 4-9.
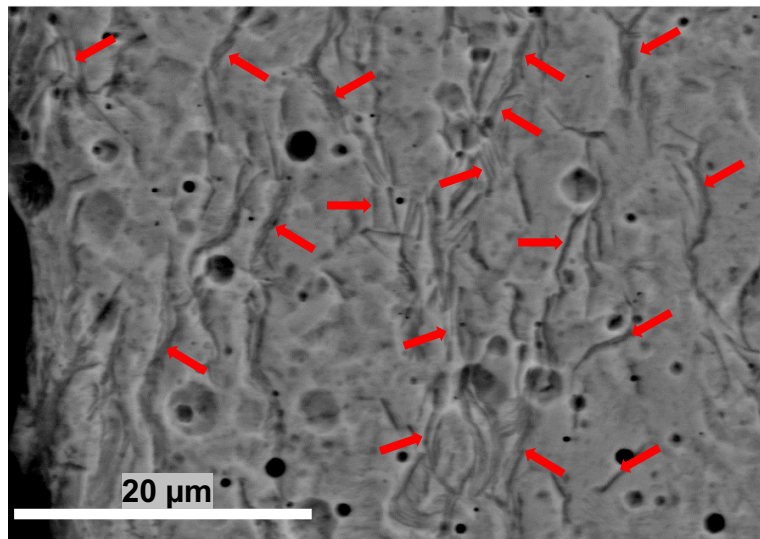
Figure 4-9 Backscatter SEM image of hydride spacing in the rim region of test sample E. Red arrows indicate dendrite-like structures of ZrHx phase.

XRD plot for E6 sample is shown in Figure 4-10. Rietveld analysis was conducted on the XRD data from both epoxy mount samples for the semi-quantitative phase analysis. In both cases, there was about 60–70% calcium carbonate ($CaCO_3$, calcite, rhombohedral in structure), which comes from the epoxy, and was verified by conducting an XRD analysis only on the epoxy part of the sample. When normalizing the remaining Zr-bearing phases that are from the sample itself, there are about 60% ZrO2 (orthorhombic), 40% Zr (hexagonal, hcp), and 1–2% total zirconium hydrides detected. There is evidence for the presence for either or both cubic and tetragonal ZrH_2 phases. It is inconclusive based on available data from the XRD, due to the small phase fraction and the overlap of some of their prominent phases.
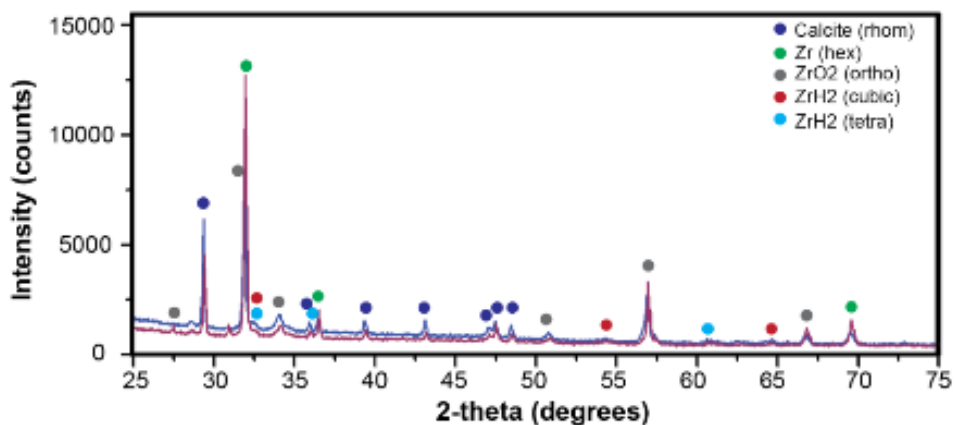
Figure 4-10. XRD plot of E6 mounted on epoxy mount.

Atom Probe Tomography (APT) analysis was performed to reaffirm chemistry and microstructure revealed by SEM and XRD. Figure 4-11 shows the 3D reconstructed tip prepared from the hydride and matrix interface. Concentration profiles were taken across the interface with peak deconvolution to confirm the presence of hydrogen. The average composition of four specimens prepared from the Zr-4 matrix and hydride region is shown inTable 4-2. Presence of H in the Zr-4 matrix is most likely from chamber or contamination due to milling in Focused Ion Beam (FIB) using Ga beam.
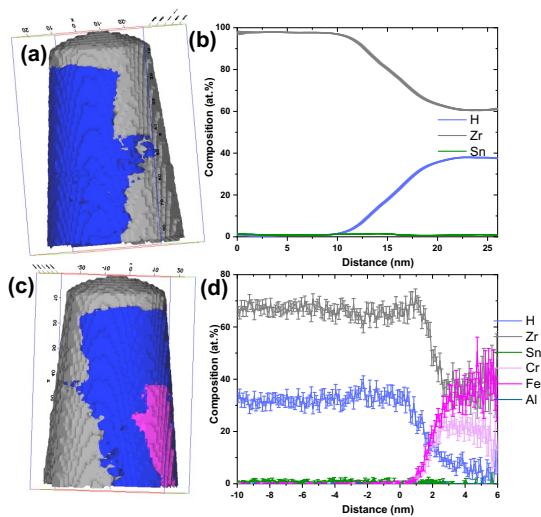
Figure 4-11 3D reconstruction of tip prepared from the ZrHx-Zr-4 interface. (a) isoconentration map of hydride (in blue) and Zr-5 (in grey), (b) 1D profile taken across the interface, (c) isocentration map showing secondary phase particle (SPP) (in pink), and (d) 1D profile taken across hydride and SPP.

Table 4-2 Measured composition of tips using APT from hydride and Zr-4 region

	ZrHx phase	Zr-4
Elements	At.%	At.%
Zr	55.56±2.2	95.63±1.2
H	43.75±3.4	2.83±1.2
Sn	0.64±0.4	1.22±0.2

Specimen for transmission electron microscopy (TEM) were prepared from the hydride region, as shown in Figure 4-12. The FIB lamella sample has several Zr grains with hydrides grown inside the grains (Figure 4-13). The hydride bundles have several hydride plates and are overall aligned. Area surrounding the hydride shows several nanosized precipitates. STEM-EDS mapping shows some of the precipitates are Si rich, while others are Fe and Cr rich, as would be expected for the cladding tubes.
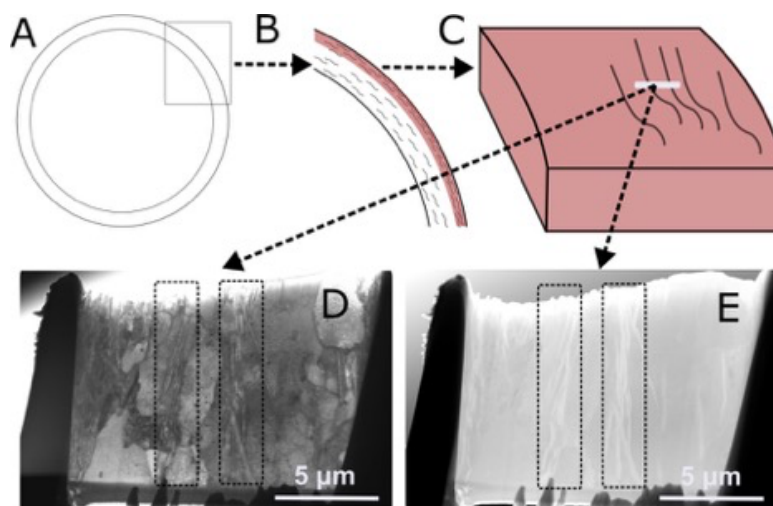
Figure 4-12 (A-E) Schematic of region from which TEM lamella is prepared capturing hydride structures.
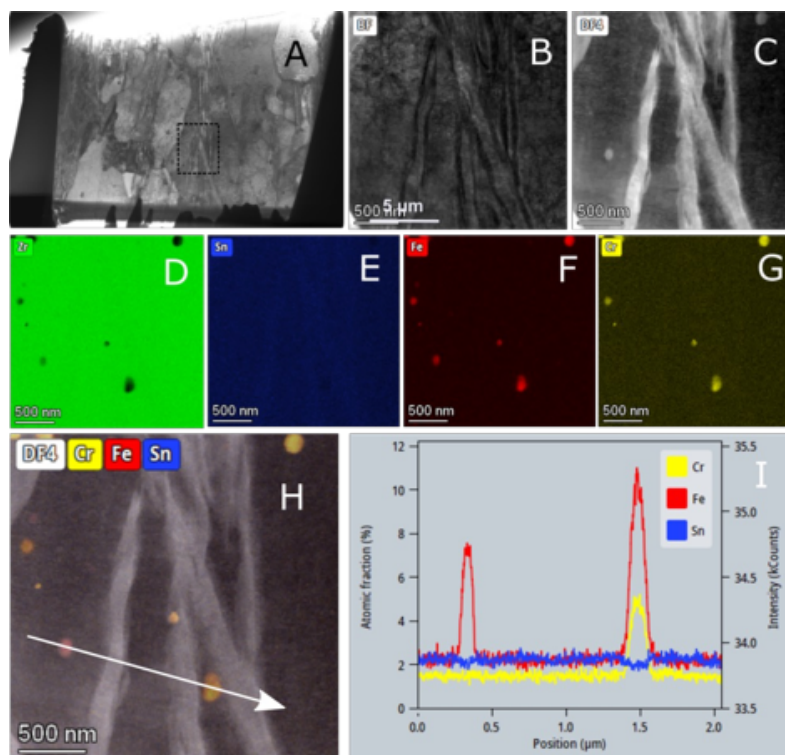
Figure 4-13 (A-C) FIB Lamella of Hydrided Zircaloy. (D-G) STEM-EDS mapping showing Fe and Cr Precipitates. (H,I) Line EDS Scan showing Sn depletion in both precipitate and hydride regions.

The hydride plates are better revealed by ADF images (Figure 4-14). The hydrides plates show white contrast in the images. The distribution of hydride has little preference over the grain boundary, at least for the two bundles as revealed in the TEM sample. Sharp interfaces are found between the hydride plates and Zr grain matrix. The hydride plate ends have a sharp needle shape and are mingled with neighbouring hydride plates.
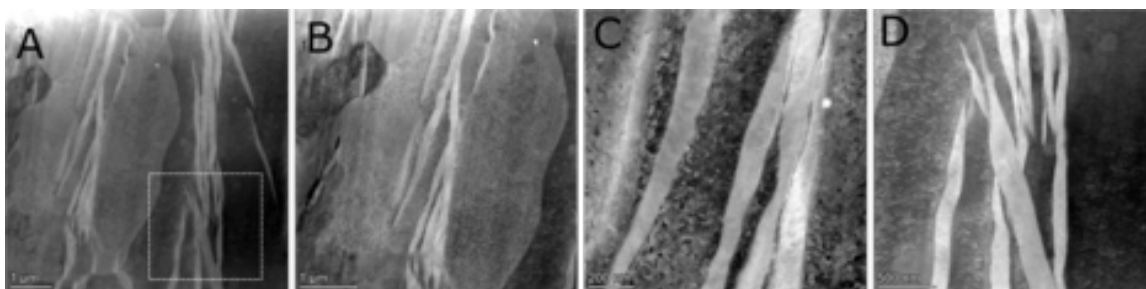
Figure 4-14 High-resolution images of hydride structures using TEM.

The TEM selected area electron diffraction (SAED) technique has a spatial resolution of ~100 nm to provide a characterization of phase nature of individual hydrides and/or surrounding Zr matrix. Figure 4-15 is a SAED study on one of the intragranular hydride bundles. The indexing of a pattern collected from the interfacial region between the Zr matrix and hydride plate shows the hydride plate has FCC crystal structure. Using the α-Zr matrix as an internal standard, the lattice parameter of hydride is measured to be 4.721 Å, which is close to the reported value of 4.77 Å for δ-ZrH$_{1.66}$ [24]. The diffraction pattern in Figure 4-15 also revealed the crystallographic relationships between α-Zr and δ-ZrH$_x$. The (0001) planes of α-Zr matrix crystal structure parallels with the (111) planes of FCC hydride structure. Furthermore, the [110] direction of δ-ZrH$_x$ parallels with [11$\overline{2}$0] of α-Zr matrix. Such a relationship has been identified previously in as fabricated Zr-2.5wt% niobium alloy pressure tubing [25].
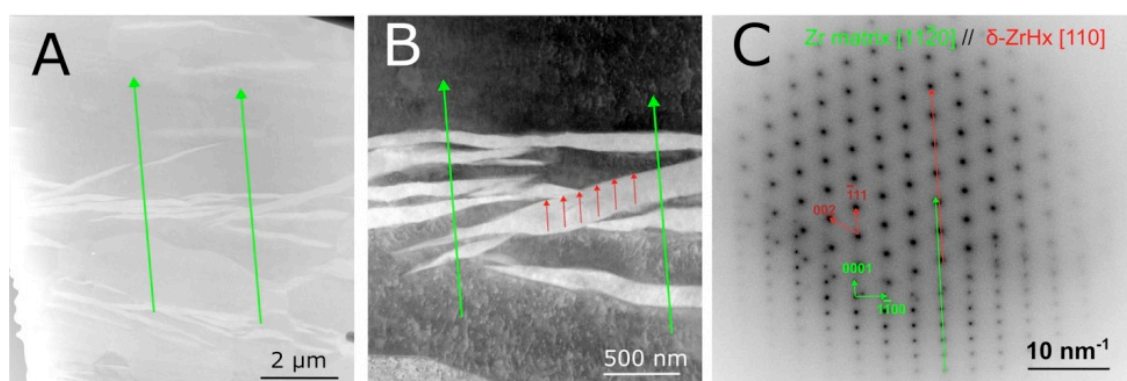
Figure 4-15 Crystallographic structure of Zr and ZrH$_{1.6}$ interface. (A) Direction of the [11$\overline{2}$0] α-Zr planes. (B,C) Direction of the [110] δ-ZrH$_x$ planes parallell to the [11$\overline{2}$0] α-Zr planes

4.4 Conclusion

The creation of representative hydride rim structures in nuclear grade, stress-relieved, zirconium alloy cladding tubes was achieved by applying the known physics driving hydrogen diffusion and precipitation in zirconium metal and a carefully designed experimental setup based on gaseous diffusion. The influence of hydrogen partial pressure, metal temperature, and surface treatment could all be clearly seen from the initial series of hydriding experiments. After the process for hydriding the tubes was standardized, more repeatable results were obtained; although, variability in the rate of hydrogen uptake in the cladding tubes still existed. During hydriding experiments with a fast pressure drop (fast hydrogen uptake), greater amounts of hydrogen were absorbed in the cladding tubes overall and thicker hydride rims were formed. A faster uptake rate also seemed to result in hydrided tubes with a much greater variability in the concentration and thickness of the hydride rims, which were

formed. A key feature of the experimental setup developed in this work is the ability to monitor the rate of hydrogen uptake in the cladding tubes by measuring the pressure drop in the hydriding chamber. This feature allows for a semi-quantitative determination of the hydride concentration and rim thickness in the hydrided tubes without the need to destructively examine them. Cladding tubes hydrided to evaluated concentrations of 200–400 wppm generally have rim thickness between 60–80 μm where, when the evaluated concentrations increase to between 400–600 wppm, the rim thickness increases to between 80–100 μm.

The nature and structure of the hydride rims was also confirmed via detailed characterization of hydrided specimens. SEM analysis showed a clear distinction between the metal and hydride phases in the rim region. The individual hydride phases were shown to be oriented in the circumferential direction, with radial spacing between them of 1–10 μm. This verifies that the hydride features formed using the standard method are sandwich-like rim features as opposed to bulk hydrides. XRD, APT, and TEM analysis provide evidence further evidence of this structure and show convincing evidence that the hydride platelets are the expected δ-Hydride phase (FCC cubic $ZrH_{1.6-1.7}$). The TEM results show that these hydride platelets are formed in the middle of the zirconium grains and verifies the circumferentially oriented needle like structure seen in the SEM. The results of the extensive characterization effort indicate that the hydrides formed via the gaseous diffusion experiments are representative of those structures and phases that form in water reactor conditions. This provides confidence that these hydrogen charging experiments can be used to produce hydrided cladding tubes for use in integral thermo-mechanical testing to aid in determining the effect that these hydrides have on the bulk deformation and fracture behavior of nuclear fuel cladding tubes.

4.5 References

1. Allen, T. R., R. J. M. Konings, and A. T. Motta. 2012. "Corrosion of Zirconium Alloys." *Comprehensive Nuclear Materials* 5: 49–68. https://doi.org/10.1016/B978-0-08-056033-5.00063-X.

2. Onimus. F., and J. L. Bechade. 2012. "4.01 – Radiation Effects in Zirconium Alloys" *Comprehensive Nuclear Materials* 4: 1–31. https://doi.org/10.1016/B978-0-08-056033-5.00064-1.

3. Georgenthum, V., et al. 2008. "Fracture Mechanics Approach for Failure Mode Analysis in CABRI and NSRR RIA Tests." Presented at *Water Reactor Fuel Performance Meeting*, Seoul Korea.

4. Kim J. S., et al. 2019. "Effects of hydride rim on the ductility of Zircaloy-4 cladding." *Journal of Nuclear Materials* 523: 383–390. https://doi.org/10.1016/j.jnucmat.2019.06.007.

5. Daum R. S., Y. S. Chu, and A. T. Motta. 2009. "Identification and quantification of hydride phases in Zircaloy-4 cladding using synchrotorin X-ray diffraction." *Journal of Nuclear Materials* 392(3): 453–463. https://doi.org/10.1016/j.jnucmat.2009.04.004.

6. Wang J. J., H. Wang, and Y. Yan. 2016. "ORNL Interim Progress Report on Hydride Reorientation CIRFT Tests." ORNL/TM-2016/660, Oak Ridge National Laboratory. https://info.ornl.gov/sites/publications/files/Pub71311.pdf.

7. Billone, M. C., T. A. Burtseva, and R. E. Einziger. 2013. "Ductile-to-brittle transition temperature for high-burnup cladding alloys exposed to simulated drying-storage conditions." *Journal of Nuclear Materials* 443(1–3): 431–448. https://doi.org/10.1016/j.jnucmat.2012.10.002.

8. Hellouin de Menibus, A., et al. 2014. "Formation and characterization of hydride blisters in Zircaloy-4 cladding tubes." *Journal of Nuclear Materials* 449(1–3): 132–147. https://doi.org/10.1016/j.jnucmat.2014.03.006.

9. Hong K., J.R., et al.. 2018. "Cracking and spalling of the oxide layer developed in high-burnup Zircaloy-4 cladding under normal operating conditions in a PWR." *Journal of Nuclear Materials* 512: 46–55. https://doi.org/10.1016/j.jnucmat.2018.10.003.

10. Marino G. P. 1971. "Hydrogen supercharging in Zircaloy." *Materials Science and Engineering* 7(6): 335–341. https://doi.org/10.1016/0025-5416(71)90016-4.

11. Kammenzind, B. F., et al. 1996. "Hydrogen pickup and redistribution in alpha-annealed Zircaloy-4." Presented at the Eleventh Annual Zirconium in the Nuclear Industry. Bettis Atomic Power Laboratory, West Mifflin, PA. https://doi.org/10.2172/10181237.

12. McMinn A., E. C. Darby, and J. S. Schofield. 2000. "The Terminal Solid Solubility of Hydrogen in Zirconium Alloys." Presented at the Twelfth Annual Zirconium in the Nuclear Industry. https://doi.org/10.1520/STP14300S.

13. Kearns, J. J. 1972. "Diffusion Coefficient of Hydrogen in Alpha Zirconium, Zircaloy-2, and Zircaloy-4." *Journal of Nuclear Materials* 43: 330–338. https://www.sciencedirect.com/science/article/pii/0022311572900657/pdf?md5=d3456fd044b865256a707401d7c7296d&pid=1-s2.0-0022311572900657-main.pdf

14. Kudiiarov, V., et al. 2020. "Hydride Rim Formation in E110 Zirconium Alloy during Gas-Phase Hydrogenation." *Metals* 10(2): 274. https://doi.org/10.3390/met10020247.

15. Puls, M. P. 2012. *The Effect of Hydrogen and Hydrides on the Integrity of Zirconium Alloy Components*. Springer, Oakville ON Canada. https://link.springer.com/book/10.1007/978-1-4471-4195-2.

16. Shimskey, R., B. Hanson, and P. MacFarlan. 2013. "Optimization of Hydride Rim Formation in Unirradiated Zr-4 Cladding." PNNL-22835, Pacific Northwest National Laboratory. https://www.pnnl.gov/main/publications/external/technical_reports/PNNL-22835.pdf.

17. Cox, B. 1984. "Mechanisms of Hydrogen Absorption by Zirconium Alloys." Presented at meeting of Materials Research Society. https://inis.iaea.org/search/search.aspx?orig_q=RN:17036758.

18. Natesan, K., and W. K. Soppet. 2004. "Hydrogen Effects on Air Oxidation of Zirlo Alloy." NUREG/CR-6851, U.S. Nuclear Regulatory Commission. https://www.nrc.gov/docs/ML0428/ML042870061.pdf.

19. Standard Specification of Wrought Zirconium and Zirconium Alloy Seamless and Welded Tubes for Nuclear Service (Except Nuclear Fuel Cladding) ASTM B353-12(2022). https://webstore.ansi.org/standards/astm/astmb35307

20. Nagase, F., and T. Fuketa. 2005. "Investigation of Hydride Rim Effect on Failure of Zircaloy-4 Cladding with Tube Burst Test." *Journal of Nuclear Science and Technology* 42(1): 58–65. https://doi.org/10.1080/18811248.2005.9726364.

21. Shinozaki, T., et al. 2016. "Improved-EDC Tests on the Zircaloy-4 Cladding Tube with an Outer Surface Pre-Crack." *Journal of Nuclear Science and Technology* 53: 1426–1434. https://doi.org/10.1080/00223131.2015.1123658.

22. Yueh, K., et al. 2016. "Fuel cladding behavior under rapid loading conditions." *Journal of Nuclear Materials* 469:177–186. https://doi.org/10.1016/j.jnucmat.2015.11.032.

23. Tomiyasu, K., T. Sugiyama, and R. Fuketa. 2007. "Influence of Cladding-Peripheral Hydride on Mechanical Fuel Failure under Reactivity-Initiated Accident Conditions." *Journal of Nuclear Science and Technology* 44(5): 733–742. https://doi.org/10.1080/18811248.2007.9711862.

24. Motta, A. T., Chen, LQ., "Hydride Formation in Zirconium Alloys" *JOM* 64: 1403-1408. https://doi.org/10.1007/s11837-012-0479-x

25. Northwood, D.O., Gilbert, R.W., "Hydrides in zirconium-2.5 wt% niobium alloy pressure tubing" *Journal of Nuclear Materials* 78(1) 112-116. https://doi.org/10.1016/0022-3115(78)90509-3

Chapter 5: The Deformation and Burst Behavior of Zircaloy-4 Cladding Tubes with Hydride Rim Features Subject to Internal Pressure Loads

David Kamerman

Abstract

This study is motivated by the desire to conduct a separate effects test replicating specific aspects of an in-pile pulse reactor test on high exposure light water reactor (LWR) fuel rods. The principal purpose of the tests was to determine whether temperature and or hydrogen concentration thresholds exist in assessing the vulnerability of a stress relieved zirconium alloy cladding tubes to low strain ruptures. A secondary objective was to determine whether observations of the cladding stress during deformation could aid in the understanding of the crack formation and propagation in cladding tubes with hydride rim features. The study utilized artificially hydrided Zircaloy-4 cladding tubes and an isothermal, internal pressure test that was controlled with an in-situ strain measurement. The test results show a clear transition in failure vulnerability between room temperature and 150 C. Below 150 C, cladding tubes rupture at very low uniform plastic strain—even at relatively modest cladding hydrogen levels. At and above 150°C, cladding tubes only rupture at low uniform plastic strain if the cladding hydrogen content is greater than 500 ppm and usually experience at least some modest amount of plastic deformation prior to rupture. Post-test metallographs from non-ruptured cladding tubes show numerous primary cracks forming in the hydride rim and arresting at the metal/hydride interface. This observation combined with the decrease in bulk yielding of hydrided cladding tubes when compared to fresh non-hydrided tubes leads to the conclusion that the fracture stress of the hydride rims is related to and bounded by the yield stress of the zirconium metal. Some evidence is presented for a change in crack propagation mechanism from one of void formation on hydride plates and linkage at temperatures below 150°C to more classical ductile shearing beneath the primary crack tip at temperatures above 150°C. This apparent change in crack propagation mechanism may help explain the observed temperature and hydrogen concentration thresholds.

5.1 Introduction

Reactivity Initiated Accidents (RIAs) are a design basis accident in nuclear power plants that are characterized by the loss or removal of a control element in the reactor core and the resulting power excursion as the result of a prompt reactivity increase. In pressurized water reactors (PWRs) and boiling water reactors (BWRs) these transients are referred to as control rod ejection accidents (CREAs) and control rod drop accidents (CRDAs). The resulting power increase is terminated due to broadening of the U-238 resonance capture cross-sections in the UO_2 fuel pellets as their temperature increases. The power pulses in CREAs and CRDAs are typically gaussian in shape during the prompt part of the transient with decaying exponential behavior following the prompt pulse. Pulse widths for CREAs and CRDAs are generally on the order of 20 ms – 80 ms when analyzed using point kinetic models of PWR and BWR cores [1]. As the transient power decays and heat is transferred to the coolant, the fuel temperature decreases from its peak radial average enthalpy. Light water reactor (LWR) fuel behavior during RIAs has been the subject of intense study since the inception of the LWR industry. The fuel rods experience a rapid temperature transient that results in rapid thermal expansion, cracking, and fission gas release in the fuel pellet. As heat is transferred from the fuel pellet to the cladding and eventually the coolant, a boiling crisis occurs on the surface of the cladding. These rapid self-heating conditions are extremely difficult to replicate and have motivated the construction and operation of dedicated pulse test reactors such as the Special Power Excursion Reactor Test (SPERT) [2], Power Burst Facility (PBF) [3], and Transient Test Reactor (TREAT) [4] reactors in the United States, the CABRI reactor in France [5] and the Nuclear Safety Research Reactor (NSRR) reactor in Japan [6].

While early pulse reactor tests showed the failure modes of LWR fuel rods to be the result of the boiling crisis which accelerates ballooning and rupture of the cladding as well as high temperature steam oxidation induced embrittlement, testing on higher burnup fuels which began in the CABRI and NSRR reactors in the early 1990s showed a different failure mode occurring at lower peak radial average enthalpies and which was independent of whether or not a boiling crisis occurred and resulted in long axial cracks the in the fuel rod test specimens [7]. It is the general consensus of the nuclear fuel research community that the loading mechanism during these lower enthalpy (pre-departure of nuclear boiling [DNB]) ruptures is due to a thermally expanding fuel pellet, resulting in a highly constrained and bi-axial pellet cladding mechanical interaction (PCMI) load [8]. While the low burst strains of most test rods support this hypothesis, the possibility of other loading mechanisms such as localized phase changes in the fuel pellet rim or transient fission gas release cannot be excluded.

The vulnerability of a fuel rod to pre-DNB failure is determined both by the condition of the fuel rod and by the nature of the pulse test. With respect to the fuel rod condition, the pellet cladding

gap that is present at the beginning of the fuel rod irradiation is closed by the middle of the irradiation due to fuel cladding creep down and fuel pellet swelling. The cladding mechanical properties are also degraded. Mechanical property changes due to irradiation damage saturate early in the life of a Zircaloy clad fuel rod [9]. However, continued exposure of the fuel rod to high temperature water coolant results in increasing oxidation behavior and hydrogen uptake and hydride precipitation. The precipitation and formation of brittle hydride features in Zircaloy cladding is thought to be the main environmental degradation mechanism for LWR cladding tubes at elevated exposures. For stress relieved zirconium alloy claddings, embrittling hydride features consist of 'rim'-like formations on the outer surface of the cladding. For recrystallized zirconium alloy claddings, embrittling hydride features consist of a high concentration of radially oriented hydrides [10]. With respect to the nature of the pulse tests, the loads imposed by PCMI would be uniform, bi-axial and displacement-controlled but with very high strain rates. If indeed the deformation is driven principally by thermal expansion the imposed strains would be limited to ~3% hoop strain for a perfectly bonded pellet and cladding with radial average enthalpies below 750 J/g [11]. Pulse tests with narrower pulse widths are assumed to be more severe as the imposed PCMI strain would occur at lower cladding temperature when the material is less ductile. The likelihood of PCMI failure is also increased because of the testing environment which in the case of CABRI consists of a sodium coolant with high heat transfer properties, and in the case of NSRR usually consists of a static water capsule at room temperature and atmospheric pressure.

At least 82 reactor pulse tests have been conducted on moderate to high burnup LWR fuel pins in the CABRI and NSRR test reactors [12]. Additionally, numerous out of pile separate effects tests have been conducted that replicate different aspects of the transient heating and loading conditions on the Zircaloy cladding [13][14][15][16]. Key to understanding whether a fuel rod is vulnerable to pre-DNB failure in an RIA transient pulse test is determining any thresholds for the low strain rupture of stress-relieved zirconium alloy cladding in terms of both the cladding temperature and cladding hydride concentration. To allow for a more mechanistic understanding of the failure mode it is also important to understand the cladding stress state evolution during its deformation.

This study is motivated by the desire to conduct a separate effects test replicating specific aspects of an in-pile pulse test. The principal purpose of the tests was to determine whether temperature and or hydrogen concentration thresholds exist in assessing the vulnerability of a stress-relieved zirconium alloy cladding tube to low strain rupture. A secondary objective was to determine whether observations of the cladding stress during deformation could aid in the understanding of the crack formation and propagation in cladding tubes with hydride rim features. Additional objectives will be to determine to what extent hydride features in the cladding affect the materials bulk

mechanical properties—particularly the cladding elastic modulus, yield stress, and ultimate tensile stress. Accurate bulk mechanical properties are necessary to predict the cladding stress state evolution during the transient and to predict the likelihood of crack formation and propagation in the cladding when subjected to a uniform, bi-axial deformation. An important component of this study was to conduct the testing under a uniform bi-axial load as previous studies conducted on ring specimens under uniaxial tension show that the hydrogen concentration or morphology do not affect the yield stress, and ultimate tensile stress of the cladding tubes [17][18]. However, Zhang et al showed a decrease in yield stress, and ultimate tensile stress was observed when testing hydrided zirconium alloy tubing in expansion due to compression testing that was not observed in ring testing [19].

5.2   Experimental Procedure

5.2.1 Materials

Stress-relieved Zircaloy-4 cladding tubes with an outer diameter of 9.5 mm and a wall thickness of 0.57 mm were used in the subject study. The cladding tubes were non-irradiated and thus exhibited no irradiation-hardening behaviors. It is acknowledged that the presence of irradiation damage in the zirconium metal will likely have the effect of increasing any derived transition temperature and decreasing any derived transitional hydrogen content. The cladding tubes are artificially hydrided using a static gaseous method. This method has been shown to reliably create a hydride rim feature on the outer surface of the cladding with fewer more widely dispersed circumferentially oriented hydride strings beneath the rim region toward the cladding inner surface. Volumetric expansion of the cladding tubes during hydriding resulted in thickness changes to the cladding tubes to approximately 0.65 mm with little to no changes in the cladding outer diameter. When charged to less than 250 ppm, the rim regions are small or nonexistent. Between 300 ppm and 400 ppm the rims tend to have thickness between 60 μm and 80 μm. Between 400 ppm and 500 ppm, the rims tend to have thicknesses between 80 μm and 110 μm. Above 500 ppm, thick hydride blisters start forming on the outer surface which can have depths as high as 200 μm or more. These blister features are less representative than the hydride rims formed at lower ppm levels but can still be found in LWR claddings with high exposure that have been subject to oxide spalling [20]. Cladding tubes ranging from 189 ppm to 838 ppm were used in this study and compared with data from fresh cladding tubes that were developed in a previous study [21].

5.2.2 Testing Procedure

To apply a uniform, bi-axial displacement-controlled load to the hydrided cladding tubes that is representative of those experienced during PCMI an internal pressurization test was utilized. The

testing apparatus uses a feedback signal from an in-situ strain measure to control a pneumatic pressure regulator between a high-pressure reservoir and the test specimen. A data acquisition system in conjunction with a control system is used to actuate the regulator based on signals from the hoop strain measurement to accomplish deformation that is displacement-controlled. A schematic of this testing apparatus is shown below in Figure 5-1.
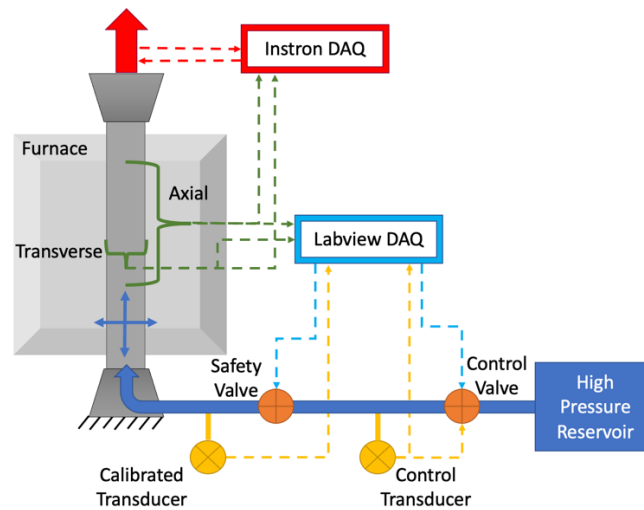
Figure 5-1 Schematic of the Internal Pressure Test System used in the present study..

Internal pressurization provides an axial to hoop stress ratio of 0.5 while, predicted PCMI stress ratios range from 0.7 to 0.8 [22]. In the development of the testing apparatus Kamerman et al. developed an anisotropic yield surface for non-hydrided Zircaloy-4 cladding tubes from the same batch as those used in this study and showed that the difference in yield behavior between a 0.5 and 0.8 stress ratio was small [21]. For simplicity, the tests took place under isothermal conditions with more modest strain rates while acknowledging the likelihood that under more realistic conditions the developed brittle to ductile temperature threshold would increase, and the hydrogen concentration threshold would decrease from those developed in this study. Testing was conducted at room temperature, 150 °C, 275 °C, and 400 °C. All tests took place at a hoop strain rate of 0.1% per minute. Approximately half of the tests used high temperature strain gauges mounted tangentially on the cladding surface. For the tests, that utilized the strain gauges they were run until cladding rupture with one exception where the strain gauge became detached from the cladding tube during the test, thus causing a false burst signal to the control system and prematurely ending the test. Following the depletion of the allotted supply of strain gauges, a high temperature transverse extensometer was used

to measure the cladding hoop strain during the tests. To prevent damage to the extensometer in the event of tube burst, tests were often terminated once 3-3.5% hoop strain was achieved. 3-3.5% hoop strain was considered a transition value as strain levels in this range could be caused entirely by a thermally expanding fuel pellet while hoop strains greater than this level would require an additional loading mechanism. However, in two tests with the extensometer the cladding tube burst during testing requiring minor repairs and recalibration of the extensometer. Following the internal pressure tests the cladding tubes or tube fragments were radially mounted, polished, and etched to confirm the existence of the expected hydride features, to discern the fracture surfaces and to observe the nature of any cracks in the cladding that did not penetrate through the cladding wall.

5.3   Results

5.3.1 Pressure Tests at Room Temperature

Five internal pressure tests were conducted at room temperature with evaluated hydrogen concentrations of 189 ppm, 398 ppm, 441 ppm, 621 ppm, and 838 ppm. All the tests resulted in early rupture with very little to no plastic flow. In fact, a yielding was only observed in the two tests with the lowest hydrogen concentration of 189 ppm and 398 ppm. Hoop stress - hoop strain curves for each of the five tests at room temperature along with a hoop stress - hoop strain curve from a non-hydrided tube are shown Figure 5-2.
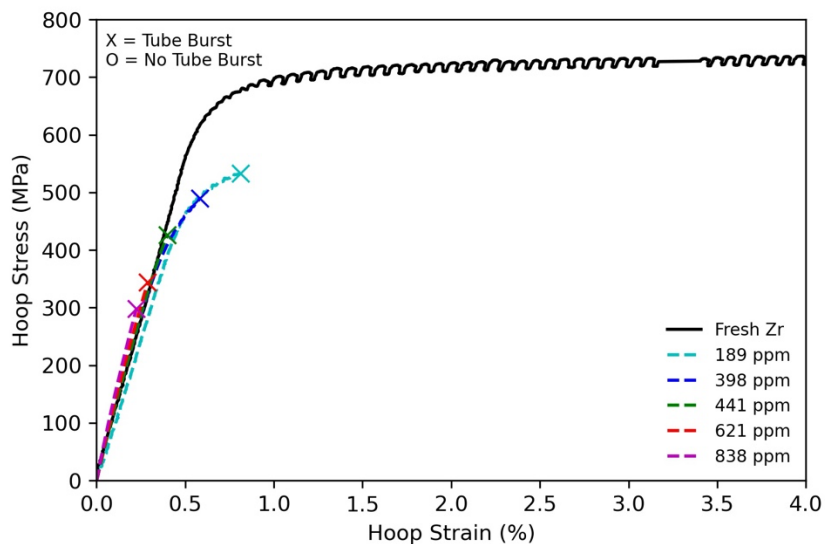

Figure 5-2 Hoop stress - hoop strain curves for cladding tubes tested at room temperature.

Fracture surfaces from the 398 ppm tube and 838 ppm cladding tube can also be seen below in Figure 5-3. While the rim feature in the 398 ppm tube appears to be representative of previously hydrided tubes in this range, the rim feature on the 838 ppm cladding tube appears to be somewhat smaller than what was seen in previous hydriding attempts at this very high level. The fracture surfaces appear to be a mix of fracture types. There is obvious cleavage type, mode-I, fracture surfaces in the rim region of the cladding and mixed mode-I and mode-II ductile shearing along a 45° band in regions of the cladding with fewer hydrides. There also appears to be sections of the cladding where the fracture surface is along the circumferential direction like a pure mode-II crack. However, these crack surfaces are along a circumferentially oriented hydride platelet and are thus unlikely to be a true mode-II shear-based crack; but they are more likely the result of a void forming along the hydride surface due to a strain incompatibility. A nonfailed region of the cladding tube from the 398 ppm sample shows what appears to be a large circumferentially oriented void forming on a hydride platelet directly in front of a propagating mode-I crack in the hydride rim. These observations support the theory of crack formation and propagation for hydrided Zircaloy developed by Raynaud et al [23].
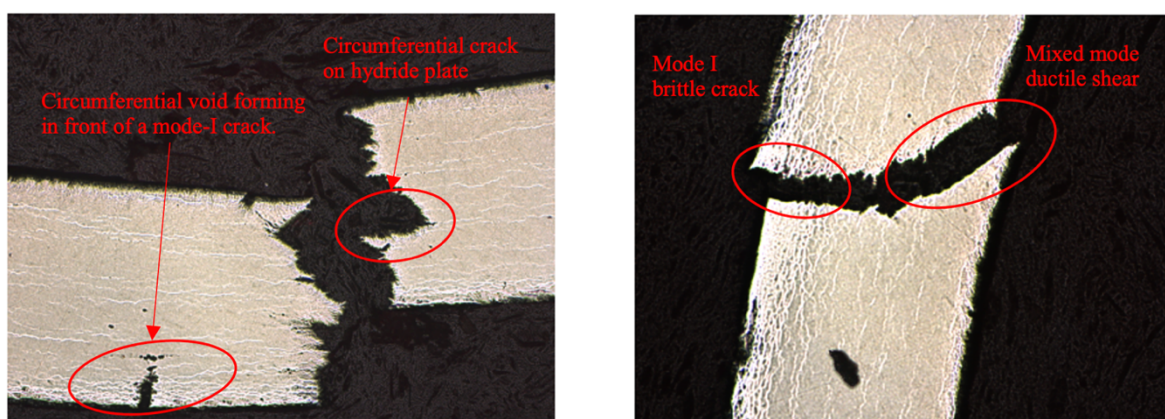
Figure 5-3 Fracture surface of 398 ppm burst tube after pressure testing at room temperature (left). Fracture surface of 838 ppm burst tube after pressure testing at room temperature (right).

5.3.2 Pressure Tests at 150 °C

Five tests were also conducted at 150 °C with evaluated hydrogen concentrations of 234 ppm, 338 ppm, 514 ppm, 595 ppm, and 629 ppm. The two tests with the highest evaluated hydrogen concentration (e.g., 595 ppm and 629 ppm) experienced early rupture in the same manner as the room temperature tests with limited yielding. For the cladding tubes with evaluated concentrations of 234 ppm and 514 ppm, yielding occurred at a much lower stress than the yield stress of the fresh cladding tubes tested at 150 °C. Following yield, these tubes experienced only a brief period of hardening

followed by what appeared to be nearly perfectly plastic behavior where the tubes reached terminal strain levels of slightly more than 3% hoop strain with only very little increase in the internal pressure or applied hoop stress. The pressure test with the cladding tube at 338 ppm was one of the most unusual tests conducted in the study. It was the only test to see a substantial load drop that occurred after yielding at ~1% hoop strain. The test continued to expand out to slightly greater than 2.5% hoop strain at a continually decreasing pressure before the test was manually terminated prior to tube rupture. Hoop stress - hoop strain curves for each of the five tests at 150 °C along with a hoop stress, hoop strain curve for a non-hydrided tube are shown in Figure 5-4.

Figure 5-4 Hoop stress - hoop strain curves for cladding tubes tested at 150 °C.

Post-test metallography images for the 234 ppm tube and the 595 ppm tube can be seen in Figure 5-5. In the cladding tubes with low hydrogen content only very small rims are present and they are intermittent. Images from the 338 ppm tube (not shown) show a slightly thicker and more persistent rim feature than the 234 ppm tube. Small mode-I cracks are seen in the post-test images of these non-ruptured cladding tubes, although they extend only the length of the rim feature. No circumferentially oriented voids could be seen in the images of the 234 ppm tube or the 338 ppm tube although in both of these tubes, the hydride features below the rim are smaller and less dense then in the other tubes hydrided to similar levels. For the cladding tubes that ruptured with hydrogen concentrations above 595 ppm, the fracture surfaces appeared to consist of zig-zag patterns of fracture like the room temperature tests with perhaps fewer circumferential voids and long mixed mode 45°

cracks. Many mode-I cracks can be seen in non-failure areas of the cladding outer surface which are arrested after reaching the softer metal.
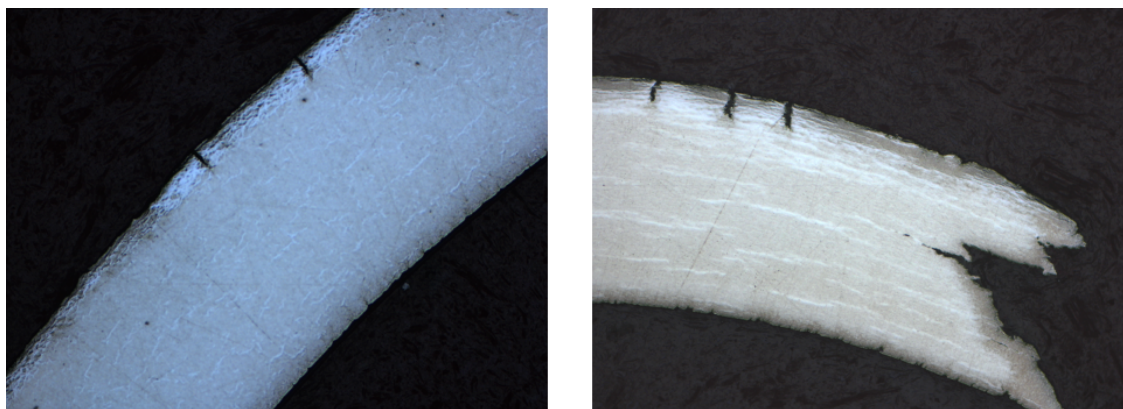
Figure 5-5. Metallography mount of cladding tube with 234 ppm hydrogen after pressure testing after pressure testing at 150 °C (left). Fracture surface of 595 ppm cladding tube after pressure testing at 150 °C (right).

5.3.3 Pressure Tests at 275 °C

Five tests were also conducted at 275 °C with evaluated hydrogen contents of 226 ppm, 380 ppm, 453 ppm, 491 ppm, and 641 ppm. Hoop stress, hoop strain curves for the five tests can be seen below in Figure 5-6. The test with the 226 ppm cladding tube follows the hoop stress hoop strain curve of the fresh Zircaloy-4 cladding tube more closely than any of the other tests. Tests with higher hydrogen concentrations also appeared to follow the stress strain curve of the fresh non-hydrided Zircaloy-4 tube closely, prior to termination or rupture. The cladding tubes with 226 ppm and 380 ppm hydrogen both deformed in a nearly perfectly plastic manner to greater than 3.5% hoop strain although at notably different internal pressures and hoop stresses. During the test with the 453 ppm cladding tube, the strain gauge became detached from the cladding early in the test just after yielding thus it is difficult to draw many conclusions from this test. The cladding tube with 491 ppm hydrogen was the first test to experience an intermediate amount of plastic deformation prior to rupturing at around 1.5% hoop strain. The cladding tube with 641 ppm hydrogen experienced an early rupture just after yielding.
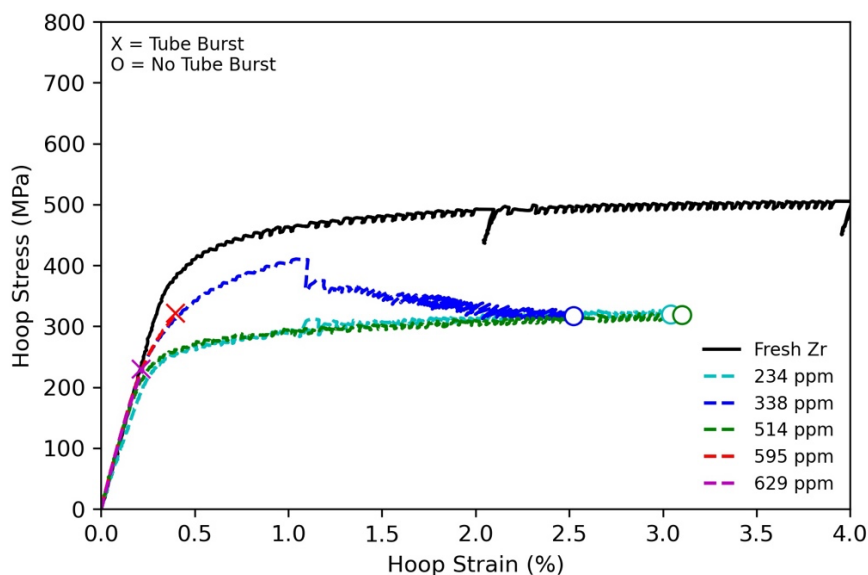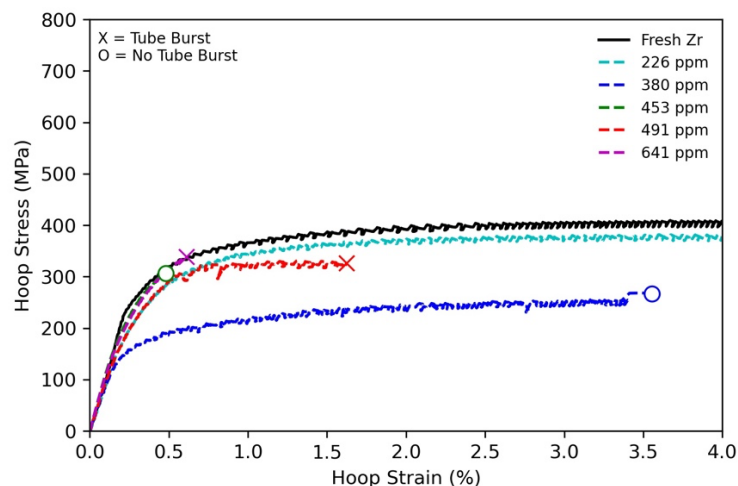
Figure 5-6. Hoop stress - hoop strain curves for cladding tubes tested at 275 °C.

Post-test metallography from the test at 226 ppm show a nearly uniform distribution of hydrides across the thickness of the cladding tube with no evidence of any cracks or voids forming along any of the hydride features. Images from the 380 ppm test are like nonfailure cases from the 150 °C tests with many mode-I cracks appearing in the rim region of the cladding and arresting at the metal hydride interface. Fracture surfaces in the 491 ppm cladding tube and the 641 ppm cladding tube show evidence of the brittle mode-I fracture surfaces in the rim region and 45° ductile shearing in the mixed metal and hydride regions below the rim. Little to no evidence is seen of circumferential voids along hydride plates aiding crack propagation at 275 °C in contrast to fracture surfaces seen at room temperature and 150 °C. Post-test metallography images for the 226 ppm cladding tube and the 641 ppm cladding tube are shown below in Figure 5-7.
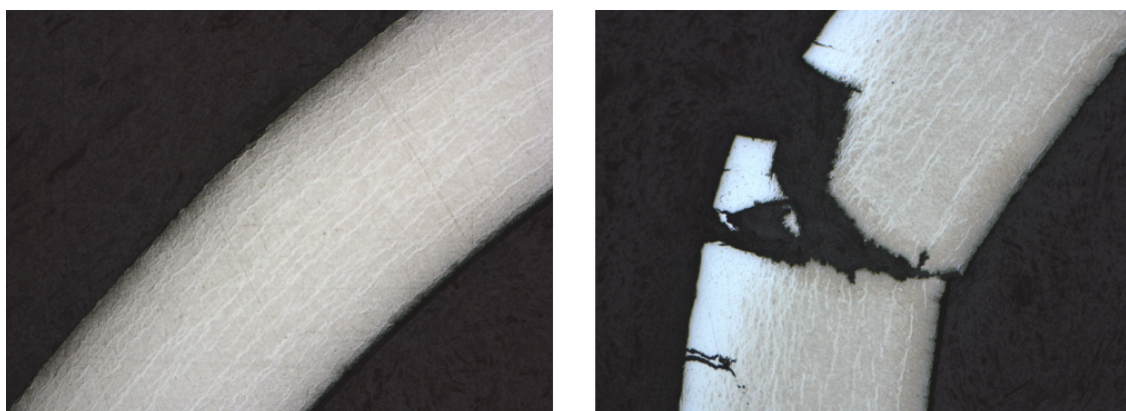
Figure 5-7. Metallographic image of the Zircaloy-4 cladding tube with 226 ppm hydrogen after pressure testing at 275 °C (left). Fracture surface of 641 ppm cladding tube after pressure testing at 275 °C (right).

5.3.4 Pressure Tests at 400 °C

Only two tubes were tested at 400 °C, both with higher hydrogen concentrations of 412 ppm and 569 ppm, respectively. Hoop stress, hoop strain curves for the two tests along with a fresh Zircaloy-4 tube are shown below in Figure 5-8. It was determined that there was sufficient evidence from the lower temperature tests that cladding tubes with lower cladding hydrogen contents had sufficient ductility at elevated temperatures to withstand typical PCMI strains of ~3% hoop strain. The test with the cladding tube at 412 ppm hydrogen followed a stress strain path that was consistent with the fresh, non-hydrided, cladding tube but with a flow stress ~50 MPa lower than the fresh tube. The test was terminated after reaching 3.5% hoop strain with no ruptures. During the test with the 569 ppm cladding tube, a sudden strain jump from 0.8% to ~1.5% occurred which caused the control system to depressurize the test specimen. However, there were no obvious indicators of cladding rupture. It was initially thought that a small cladding rupture occurred in this test but that the test system responded quickly enough and depressurized before gross ruptures and fragmentation of the cladding could occur. Numerous and relatively large axial cracks could be visibly seen on the surface of the 569 ppm cladding tube after testing as observed in Figure 5-9. However, no through wall cracks could be found either in a visual inspection or during metallography. Thus, while it may be that failure of this cladding tube was imminent, it cannot be said with certainty that failure occurred. In metallography images of both tubes, many mode-I cracks can be seen through the very dense hydride layer although the tips of these cracks are much more rounded than those in tests at lower temperatures. Figure 5-10 below shows a blunted crack from the pressure test on the 412 ppm hydrided tube.
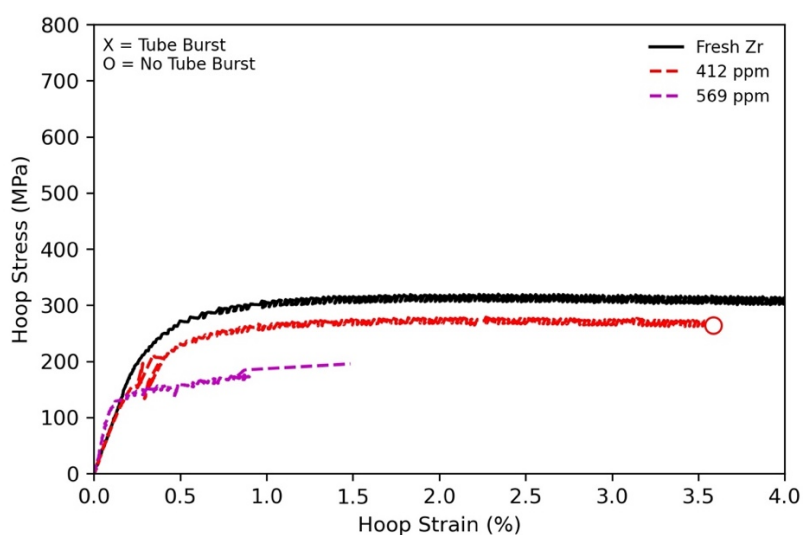
Figure 5-8. Hoop stress, hoop strain curves for cladding tubes tested at 400 °C.
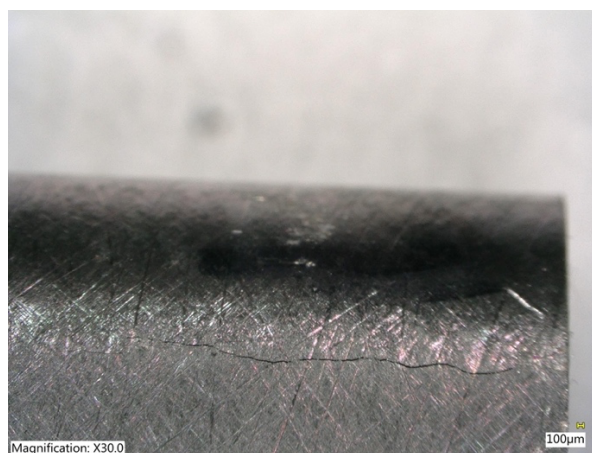
Figure 5-9. Visual cracking on the surface of cladding tube with 569 ppm hydrogen after pressure testing at 400 °C.

Figure 5-10. Metallographic image of a cladding tube with 412 ppm hydrogen after pressure testing at 400 °C.

5.4 Discussion

The results of the study strongly suggest that the embrittling effects of circumferentially oriented hydrides and hydride rim features in a stress-relieved zirconium alloy cladding tube are most prominent at temperatures below 150 °C. However, the study also suggests that hydride embrittlement can persist at least up to 275 °C—if not all the way to 400 °C for cladding tubes that are severely hydrided—with hydrogen concentrations greater than 500 ppm containing very thick rims and hydride blister features. Table 5-1shows the maximum uniform plastic hoop strains for all the cladding tubes tested in this study sorted by test temperature and evaluated hydrogen

concentration bins. The plastic strains reported in Table 5-1 are highlighted in red for cladding tubes that burst and in green for tubes that were manually terminated after exceeding at least 2% plastic strain with many of these tests reaching 3% plastic strain or more. Four of the tests ruptured prior to any apparent bulk yielding, these tests are highlighted in a darker shade of red. For the test at 275 °C which was prematurely ended due to strain gauge failure, no conclusion can be reached regarding its ductile or brittle behavior and thus it is not highlighted. The test at 400 °C with 569 ppm hydrogen is highlighted in yellow as this test may have been about to fail given the sudden strain increase it experienced prior to the test being prematurely terminated by the control system.

Table 5-1 Uniform plastic hoop strains of hydrided and pressure tested Zircaloy-4 cladding tubes.

Uniform Plastic Hoop Strains				
	RT	150 °C	275 °C	400 °C
<250 ppm	0.3%	>2.8%	>4.1%	
300-400 ppm	0.2%	>2.3%	>3.6%	
400-500 ppm	0%	>2.9%	>0.3%	>3.4%
500-625 ppm	0%	0.16%	1.6%	1.4%
>625 ppm	0%	0%	0.6%	

5.4.1 Stress Evolution During the Pressure Test

An interesting element of this study was the ability to capture the full stress strain behavior of the cladding tubes during deformation. No obvious or statistically significant changes in the modulus of elasticity are observed for the hydrided tubes relative to the tests with fresh cladding tubes. Work by Rico et al shows only a slight difference in the Young's modulus of zirconium hydrides in a metal matrix verses the modulus of the matrix [24]. Thus, the fact that the elastic part of the deformation is unaffected by the hydrides is not surprising. All the hydrided tubes show a decrease in both the hoop stress at yield and the maximum stress reached during the test when compared to fresh, non-hydrided tubes as shown in Figure 5-11. The trends in hoop stress at yield and maximum hoop stress generally tend to decrease with increasing temperature. In the room temperature data, there is a decreasing trend in the hoop stress at yield and maximum hoop stress with increasing hydrogen concentration although at elevated temperature tests this trend does not appear to be present acknowledging the amount of variability in the data. The shapes of the hoop stress - hoop strain curves were often quite similar to those of fresh, non-hydrided Zircaloy-4 which experience a very sharp yield shoulder followed by a nearly perfectly plastic deformation at a constant flow stress.
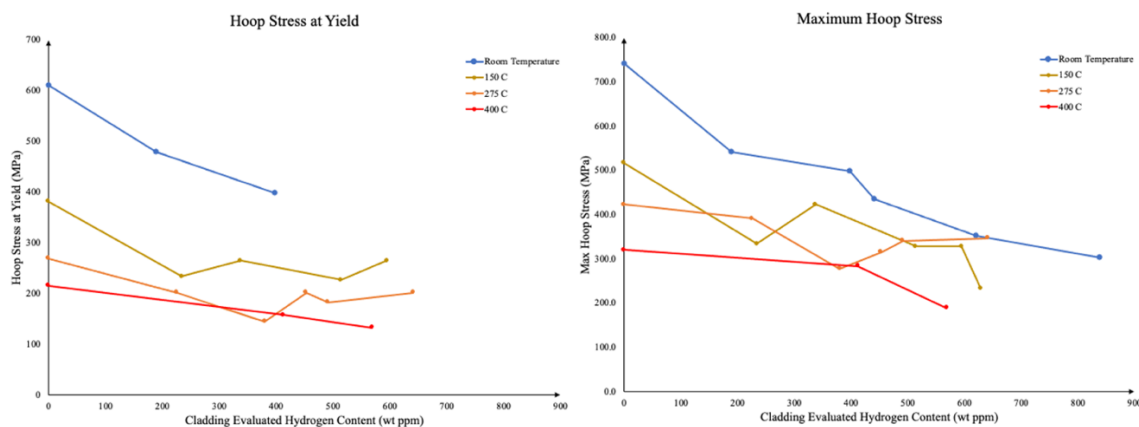
Figure 5-11 Hoop stress at yield (left) and maximum hoop stress (right) as a function of test temperature and evaluated hydride concentration.

With a single exception, metallography of the cladding tubes showed evidence of many mode-I cracks through the hydride rim region and arresting at the metal / hydride interface regardless of whether the cladding tube burst or not—the exception being a 275 °C test involving a cladding tube with an evaluated hydride concentration of 226 ppm and no evidence of a hydride rim in the metallographs. It is also this test that most closely follows the stress strain behavior of a fresh, non-hydrided cladding tube. The evidence strongly suggests that what appears to be a bulk yielding of the cladding tube is in fact the hoop stress at which the hydride rim begins to fracture. Work by Barraclough et al showed that the fracture stress of pure zirconium hydrides in tension is around 200 MPa at room temperature and decreases to less than 100 MPa by 500 °C [25]. This finding was supported by Lanin et al [26] and Zhang et al [19]. The fracture stress of zirconium hydrides embedded in a zirconium metal matrix has not been extensively studied although a review and study by Kubo et al suggested this value could be much higher around 700 MPa [27]. The data from the experiments described herein would suggest fracture strengths that decrease with temperature and are related to—or at least bounded by—the yield stress of the metal. Evidence of circumferential voids forming on or near hydride plates is observed in cladding tubes tested at room temperature and 150 °C. However, it is not obvious from this study if these voids form before or after the principal mode-I cracks in the rim regions. It may be that many such voids forming in the rim region is the method of the mode-I crack formation, although this cannot be stated conclusively. In the three tests at room temperature, and one test at 150 °C where the heavily hydrided tube ruptured prior to any observed bulk yielding—the rupture stress is always bounded by the hoop stress at yield for cladding tubes tested at the same temperature with lower hydrogen concentrations that do experience yield. It is clear

from this study that the hydrides are not strong enough to provide a constraining effect on the cladding and that in addition to decreasing the ductility of the tubes, the presence of hydrides also serves to weaken them.

5.4.2 Observed Modes of Fracture Propagation

The fracture of the hydride rim leads to stress concentrations at the crack tips and a concentration of plastic flow around the crack tips. At room temperature, the stress intensity factor at these crack tips would be much higher due to the higher hoop stresses in the cladding when the cracks form. These stress concentrations in front of the crack tips are likely contributing to the formation of the voids on the hydrides deeper in the metal in front of the propagating crack. This mechanism is what is most likely leading to crack propagation and early failure in the room temperature cases. Molecular dynamic simulations by Ghaffarian et al show that the formation of these voids is governed by the amount of stress concentration at the metal hydride interface [28]. This would explain the existence of these features in the lower temperature tests when the flow stress is higher. The fracture surfaces of cladding tubes that burst at low temperature consistently have a zig-zag pattern with short 45° ductile shear bands connecting the circumferential voids that appear to have formed on the hydrides. The nonfailure of the 514 ppm cladding tube at 150 °C was particularly perplexing given that it did not burst and accommodated >3% strain in spite of its high hydrogen content. The metallography of this sample showed a thick but very consistent rim region with many mode-I cracks, but a surprising lack of hydride features below the rim region (Figure 5-12). The resilience of this cladding tube maybe explained by the larger number of relatively uniform cracks distributing the stress more uniformly across the cladding circumference, or by the lack of hydrides beneath the crack tips to aid in crack propagation via the above-described void formation mechanism.
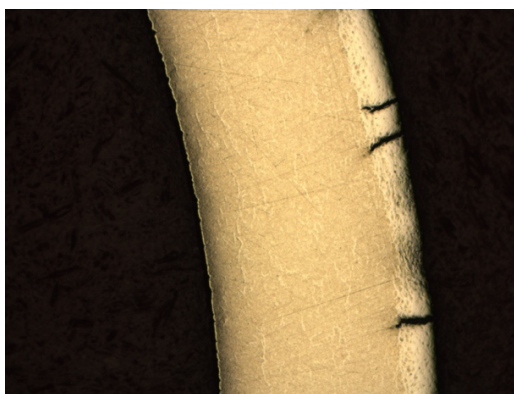

Figure 5-12 Post-test metallograph of a 514 ppm cladding tube tested at 150 °C.

At higher temperatures, the role of the hydrides in a metal matrix beneath the rim region in aiding crack propagation appears to decrease in favor of a longer and more prominent 45° mixed mode-I and mode-II ductile shear band. This theory would suggest that at lower temperatures of 150 °C and below, the thickness of the hydride rim may not be as important of a factor in the determining the vulnerability of the metal to low strain rupture as compared to the overall density of hydrides in the metal throughout its thickness. However, at elevated temperatures of 275 °C and above the hydride rim thickness will be a much more important factor as thicker rim regions would create a much greater stress intensity factor in the material that is also weaker and more vulnerable to classic ductile failure. This theory is also supported by the greater sensitivity of the strength parameters to hydrogen concentration in the room temperature tests than in the elevated temperature tests. The observed transition points also support this theory as below 150 °C the cladding tubes rupture with little to no uniform plastic strain even at modest hydrogen concentrations. However, above 150 °C a sufficiently thick and non-uniform rim or blister region is required to cause failure at low uniform plastic strain. In cladding tubes that rupture at low temperature (e.g., < 150°C) where crack propagation is aided by a void formation mechanism very low to nonexistent uniform plastic strains are developed in the metal, while in cladding tubes which rupture at higher temperature (e.g., > 150 °C) at least a minimal amount of uniform plastic strain is required to propagate the cracks that form in the hydride rim.

5.4.3 Implications to Pulse Test Failure Vulnerability

The implications of this study to understanding the vulnerability of high exposure LWR fuel rods to 'pre-DNB' failure in pulse tests are somewhat complex. While the tests in this study take place at constant temperature, the cladding tubes in a pulse test are increasing in temperature concurrent with their loading. If the pulse width of the transient is short enough, the heating while loading effect is minimized, and the results of this study would strongly suggest that fuel rods with a closed pellet cladding gap, which have a notable concentration of hydrogen and are tested in room temperature water, are highly vulnerable to rupture. However, if the pulse width is longer and the cladding temperature is dramatically increasing during the PCMI loading, or if the test takes place at an initially elevated temperature, the vulnerability of the cladding to rupture is significantly decreased. However, the risk of failure at higher cladding temperatures is not eliminated entirely. In fact, there are some additional, if perhaps more subtle, vulnerabilities for the cladding at elevated temperature. The yield stress and ultimate strength of the cladding decreases remarkably with increasing temperature. The results of this study suggest that the fracture of the hydride rim region is related to and bounded by the yield stress of the metal. Thus, even if the cladding temperature is

relatively high, mode-I fractures in the hydride rim are highly likely to occur creating a stress concentration at this crack tip. As the cladding temperature increases its strength and toughness decreases making propagation of this crack from ductile shearing more likely. The cladding will likely survive if the strain is limited to that caused by a thermally expanding fuel pellet. However, if other loading mechanisms—such as local fission gas release and impaired axial gas transport—cause additional stress to the cladding it is likely that rupture can still occur given the weakened state of the cladding near these crack tips. An initial hydrogen concentration threshold of 500 ppm is supported in this study as being the requisite level to create a hydride feature large enough to generate a crack of sufficient depth to cause a low strain failure. It is acknowledged, however, that much more data and testing are required to support this threshold and that the effects of strain rate and irradiation damage should be included in future studies before such thresholds could be used in the analysis of actual LWR fuel rod pulse test vulnerability assessments.

5.5 Conclusion

It was observed that cladding tubes pressure tested at room temperature were highly vulnerable to rupture at low hoop strain. At 150 °C and higher temperatures, the cladding tubes seemed to only rupture at low hoop strain with hydrogen concentrations above 500 ppm and with the required strain to rupture increasing with increasing temperature. In all cases, the hoop stress at yield, or maximum hoop stress in the test was always bounded by the values for the fresh, non-hydrided Zircaloy-4. Evidence of mode-I fractures in the hydride rim regions of the pressure tested cladding tubes was observed in all but one test. An important outcome of this study is that the formation of these primary fractures in the hydride rim is related to and bounded by the yield stress of the zirconium metal.

The apparent mode of crack propagation at room temperature and perhaps up to 150 °C appeared to be the formation of circumferential voids on hydrides in front of the mode-I crack tip while the mode of crack propagation for cladding tubes that ruptured above 150 °C was a pure 45° ductile shearing of the metal beneath the crack tip. The apparent transition in failure mode around 150 °C supports this as a temperature threshold. The observation of 45° ductile fractures beneath the primary cracks on cladding tubes that ruptured at higher temperatures with high hydrogen concentrations supports the theory that large non-uniform hydride features are required to cause failure with low uniform plastic strain in cladding tubes deformed at elevated temperature. While increasing temperature dramatically improves the resilience of the cladding tubes to failure at low uniform plastic strain it does not eliminate its vulnerability to these kinds of failures. In fact, the low

strength and toughness of cladding tubes at elevated temperatures with large primary cracks from outer surface flaws may be more vulnerable to rupture from loading mechanisms that are not displacement-controlled, such as the release and trapping of local fission gases.

5.6 References

1.   Clifford P.M., *Technical and Regulatory Basis for the Reactivity-Initiated Accident Acceptance Criteria and Guidance Revision 1,* U.S. Nuclear Regulatory Commission Office of Nuclear Reactor Regulation (2015) https://www.nrc.gov/docs/ML1418/ML14188C423.pdf.

2.   Fujishiro T., MacDonald P.E., Johnson R.L., McCardell R.K., *Light Water Reactor Fuel Response During Reactivity Initiated Accident Experiments* NUREG/CR-0269 TREE 1237, Idaho National Engineering Laboratory (1978) https://inis.iaea.org/search/search.aspx?orig_q=RN:10437309.

3.   McCardell R.K., MacDonald P.E., "Safety and licensing issues that are being are being addressed by the Power Burst Facility Test Programs" *Proceedings from CSNI Specialist Meeting on Safety Aspects of Fuel Behavior in Off-Normal and Accident Conditions*, Helsinki Finland (1980) *https://inis.iaea.org/collection/NCLCollectionStore/_Public/12/581/12581573.pdf?r=1.*

4.   Jensen C.B., Woolstenhulme N.E., Wachs D.M., "The TREAT Experiment Legacy Supporting LWR Fuel Technology" *Proceedings TopFuel 2018* (2018) Prague CZ. https://www.euronuclear.org/archiv/topfuel2018/fullpapers/TopFuel2018-A0168-fullpaper.pdf.

5.   Papin J., Cazalis B., Frizonnet M., Desquines J., Lemoine F., Georgenthum V., Lamare F., Petit M., "Summary and Interpretation of the CABRI REP-Na Program" *Nuclear Technology* Vol 157 (2007) pp 230-250. https://doi.org/10.13182/NT07-A3815.

6.   Udagawa Y., Sugiyama T., Amaya M., "Thresholds for failure of high-burnup LWR fuels by Pellet Cladding mechanical interaction under reactivity-initiated accident conditions" *Journal of Nuclear Science and Technology* Vol 56 (2019) pp 1063-1072. https://doi.org/10.1080/00223131.2019.1637795.

7.   Fuketa T., "Transient Response of LWR Fuels (RIA)" *Comprehensive Nuclear Materials* 2.22 (2012) pp 322-388 https://doi.org/10.1080/00223131.2019.1637795.

8.   *Nuclear Fuel Behavior Under Reactivity-Initiated Accident Conditions State of the Art Report,* NEA No. 6847 (2010) Organization for Economic Co-operation and Development Nuclear Energy Agency. https://www.oecd-nea.org/jcms/pl_14526/nuclear-fuel-behaviour-under-reactivity-initiated-accident-ria-conditions?details=true.

9.   Onimus F. Bechade J.L., "Radiation Effects in Zirconium Alloys" *Comprehensive Nuclear Materials* 4.01 (2012) pp 1-31. https://doi.org/10.1016/B978-0-08-056033-5.00064-1.

10.   Allen T.R., Konings R.J.M., Motta A.T., "Corrosion of Zirconium Alloys" *Comprehensive Nuclear Materials* 5.03 (2012) pp 49-68. https://www.nuce.psu.edu/Motta/Publications/2012_Allen_CNM.pdf.

11.   *Thermophysical properties database of materials for light water reactors and heavy water reactors* IAEA-TECDOC-1496 (2006) International Atomic Energy Agency. https://www.iaea.org/publications/7489/thermophysical-properties-database-of-materials-for-light-water-reactors-and-heavy-water-reactors.

12.   Kamerman D., Jensen C., Folsom C., Woolstenhulme N., Wachs D., "A review of cladding failure thresholds in RIA conditions based on transient reactor test data and the need for continued testing" *Proceedings from Topfuel 2022* (2022) Raleigh NC. https://www.ans.org/meetings/topfuel2022/session/view-1381/.

13.   Daum R.S., Majumdar S., Bates D.W., Motta A.T., Koss D.A., Billone M.C. "On the Embrittlement of Zircaloy-4 Under RIA Relevant Conditions" *Zirconium in the Nuclear Industry: Thirteenth International Symposium, ASTM STP 1423* (2002) pp 702-719. https://doi.org/10.1520/STP11412S.

14.   Hellouin de Menibus A., Auzoux Q., Monagabure P., Macdonald V., Le Jolu T., Besson J., Crepin J., "Fracture of Zircaloy-4 cladding tubes with or without hydride blisters in uniaxial to plane strain conditions with standard and optimized expansion due to compression tests" *Materials Science and Engineering* Vol 604 (2014). https://doi.org/10.1016/j.msea.2014.02.075.

15.   Nagase F., Toyoshi F., "Investigation of Hydride Rim Effect on Failure of Zircaloy-4 Cladding with Tube Burst Test" Journal of Nuclear Science and Technology Vol 42 (2005). pp 58-65 https://doi.org/10.1016/j.msea.2014.02.075.

16.   Yueh K., Karlsson J., Stjarnsater J., Schirire D., Ledergerber G., Munoz-reja C., Hallstadius L., "Fuel cladding behavior under rapid loading conditions" *Journal of Nuclear Materials* Vol. 469 (2016) pp 177-186. https://doi.org/10.1016/j.jnucmat.2015.11.032.

17.   Rengel-Martin M.A., Gomez Sanchez F.J., Ruiz-Hervias J., Caballero L., Valiente A., "Revisiting the method to obtain the mechanical properties of hydrided fuel cladding in the hoop direction" *Journal of Nuclear Materials* Vol 429 (2012) pp 276-283. https://doi.org/10.1016/j.jnucmat.2012.06.003.

18.   Kamerman D., Cappia F., Wheeler K., Petersen P., Rosvall E., Dabney T., Yeom H., Sridharan K., Sevecek M., Schulthess J., "Development of axial and ring hoop tension testing methods for nuclear fuel cladding tubes" *Nuclear Materials and Energy* Vol 31 (2021) https://doi.org/10.1016/j.nme.2022.101175.

19.   Zhang Y., Qi H., Song X., "Expansion deformation behavior of zirconium alloy claddings with different hydrogen concentrations" *Journal of Nuclear Materials* Vol 554 (2021)

20.   Hong, K., Barber J.R., Thouless M.D., Lu W., "Cracking and spalling of the oxide layer developed in high-burnup Zircaloy-4 cladding under normal operating conditions in a PWR" *Journal of Nuclear Materials* Vol 512 (2018) pp 46-55. https://doi.org/10.1016/j.jnucmat.2018.10.003.

21.   Kamerman D., Nelson M., "Multiaxial Plastic Deformation of Zircaloy-4 Nuclear Fuel Cladding Tubes" *Nuclear Technology* Vol 209 (2023) pp 872-886. https://doi.org/10.1080/00295450.2022.2160174.

22.   Udagawa Y, Sugiyama T, Suzuki M, et al. "Stress biaxiality in high-burnup PWR fuel cladding under reactivity initiated accident conditions." *Journal of Nuclear Science and Technology* Vol 50. (2013) pp 645–653. https://doi.org/10.1080/00223131.2013.787030.

23. Raynaud P.A., Koss D.A., Motta A.T., "Crack growth in the through-thickness direction of hydrided thin-wall Zircaloy sheet" *Journal of Nuclear Materials* Vol 420 (2012) pp 69-82. https://doi.org/10.1080/00223131.2013.787030.

24. Rico A., Martin-Rengel M.A., Ruiz-Hervias J., Rodriguez J., Gomez-Sanchez F.J., "Nanoindentation measurements of the mechanical properties of zirconium matrix and hydrides in unirradiated pre-hydrided nuclear fuel cladding" *Journal of Nuclear Materials* Vol 452 (2014) pp 69-76. https://doi.org/10.1016/j.jnucmat.2014.04.045.

25. Barraclough K.G., Beevers C.J., "Some Observations on the Deformation Characteristics of Bulk Polycrystalline Zirconium Hydrides, part 1 The Deformation and Fracture of Hydrides Based on the δ-phase" *Journal of Materials Science* Vol. 4 (1969) pp 518-525. https://link.springer.com/article/10.1007/BF00550212.

26. Lanin A.G., Zalivin I.M., Turchin V.N., Boiko E.B., "Mechanical properties of zirconium, titanium, and yttrium hydride alloys" *Strength of Materials* Vol 16 (1984) pp 869-876. https://inis.iaea.org/search/search.aspx?orig_q=RN:16013125.

27. Kubo T., Kobayashi Y., Uchikoshi H., "Determination of fracture strength of δ-zirconium hydrides embedded in zirconium matrix at high temperatures" *Journal of Nuclear Materials* Vol 435 (2013) pp 222-230. https://doi.org/10.1016/j.jnucmat.2012.12.045.

28. Ghaffarian H., Jang D., "Deformation mechanism of embedded hydride within the polycrystalline zirconium matrix" *Journal of Nuclear Materials* Volume 565 (2022). https://doi.org/10.1016/j.jnucmat.2022.153736.

Chapter 6: Summary and Recommendations for Future Work

This dissertation work set out to better quantify the role of circumferential hydrides and hydride rim structures in causing low strain ruptures in stress relieved zirconium alloy cladding tubes in transient reactor pulse tests. A careful review of the publicly available transient reactor pulse test database showed that the prevalence of these kinds of low strain failures is certainly related to the concentration and distribution of circumferential hydrides in the metal matrix. For the stress relieved family of alloys low strain failures are most prevalent in the room temperature static water capsule environment used for testing in the NSRR reactor in Japan. The cold initial condition of the metal combined with the rapidness of the NSRR pulse which prevents the cladding from heating prior to measurable PCMI loads are likely contributors to the prevalence of low strain failures in this kind of pulse reactor test. Low strain cladding failures in this kind of pulse test begin at relatively low cladding hydrogen concentrations of 132 ppm. While the database is certainly more limited for pulsed reactor tests which have more prototypic initial cladding temperatures, data that does exist from a hot version of the NSRR static water capsule and the CABRI sodium loop, both with initial cladding temperatures in the 250 °C – 280 °C range suggest that this hydrogen threshold increases to at least 400 ppm and is more than likely above 500 ppm.

A review of previous separate effects studies seems to suggest similar hydrogen concentration thresholds only when the tests involve cladding materials with a prototypic distribution or morphology of circumferential hydrides in the metal cladding tubes. The key features of this prototypic distribution are a high concentration of hydrides on the cladding outer surface, known as the rim region, and a more sparse distribution of hydrides beneath the rim. Rim thickness ranges between 30 μm at low hydrogen concentrations to greater than 100 μm at higher hydrogen concentrations. A novel way of artificially creating these prototypic hydride structures was developed which allowed for a determination of an evaluated cladding average hydride concentration by monitoring the pressure drop of a static charge of hydrogen gas in the hydriding chamber. It was shown that through careful control of the cladding inner and outer surface preparation and finding the ideal hydriding temperature that hydride rim structures would form on the outer surface of the cladding tubes with a less dense population of circumferential hydrides beneath the rim feature. Characterization of the artificially created hydrides showed that they were indeed of the phase, size, shape, and distribution of those found in high exposure stress relieved cladding tubes.

Even with a prototypic hydride structure it is often difficult to compare or interpret separate effects test data with transient pulse reactor data. Key separate effects test features that were chosen to focus on in this study included the ability to create a uniform bi-axial load in the cladding tube that would be strain controlled such the flow stresses during plastic deformation could be determined. These separate effects tests were achieved by programming an in-situ cladding hoop strain measurement system into a feedback loop with a high-pressure pneumatic regulator. Validation of this test stand with fresh nuclear grade Zircaloy-4 cladding tubes show cased its ability to reliably reproduce known mechanical properties of the metal with high accuracy and precision. It was also shown how the bi-axial nature of this test allowed for the determination of Hill yield coefficients. These Hill coefficients allowed for the construction of an anisotropic yield surface. The Hill yield loci showed that much higher hoop stresses are required to initiate yielding when the cladding is loaded in a bi-axial manner due to the texture of the cladding but that these effects begin to diminish after the cladding temperature exceeds 150 °C. Another important finding from the strain-controlled pressure testing of fresh cladding tubes was the quick hardening followed by nearly perfectly plastic flow of the material under the bi-axial load.

When the strain-controlled pressure tests were applied to cladding with representative hydride rim features, failure thresholds were suggested similar to those predicted by evaluation of the pulse test database. That at low cladding temperatures, less than 150 °C, the stress relieved zirconium alloy cladding tubes begin rupturing at very low strain with even modest concentrations of cladding hydrogen, less than 189ppm in the present study. However, at higher temperatures of 150 °C and above cladding ductility is remarkably improved and only cladding tubes with ~500 ppm of hydrogen of higher experience low strain ruptures. Given the low strain rates and lack of irradiation damage in the cladding tubes the recreation of these thresholds in these separate effects test is rather remarkable and confirms that the primary variables effecting cladding rupture are the quantity and distribution of the hydrides, the temperature of the cladding, and the bi-axial nature of the cladding loading path. Another significant finding from the strain-controlled pressure testing has to do with the mechanisms of cladding rupture. Rather than providing a constraining effect on the cladding tubes during loading the hydride rims always fractured at hoop stress levels below that which would have caused cladding yielding in a non hydrided sample. This observation is not seen in cladding mechanical tests that are uniaxial in nature.

The fracture that forms in the rim region of the cladding tube is a Mode-1 crack that is arrested at the metal hydride interface. Following formation of these Mode-1 cracks in the hydride rim the bulk stress-strain behavior of the cladding tubes follow a path that is often similar to fresh

cladding tubes with a quick hardening shoulder and the nearly perfectly plastic deformation albeit at a typically much lower flow stress. The lower flow stress is because the stress and strain are more concentrated at the tips of the Mode-1 cracks which have formed. In cladding tubes which are undergoing deformation at low temperature the hoop stress fields and thus stress intensity factor at these crack tips is quite high and is likely causing the formation of circumferential voids on the circumferential hydrides beneath the rim in front of the crack tips. The formation and linkage of these voids to the primary mode-I crack and each other via 45° shear bands in the metal between the hydrides causes a zig-zag pattern of fracture at low overall cladding hoop strain. Above 150 °C no evidence of these circumferential voids are seen, and the cladding tubes which rupture at low overall hoop strain only do so when a very large Mode-I crack is formed in a very thick hydride rim or blister and the stress intensity factors are sufficiently high in this region to propagate the crack through the thickness by a ductile shearing mechanism alone.

It is often difficult to obtain good metallographic images of the fractured cladding surfaces as upon rupture the cladding tubes are fragmented and distorted due to the high stored energy in the compressed gas, pressurizing the tube. The pneumatic nature of the pressure test leads to other limitations such as the inability of the test stand to perform testing at prototypic strain rates. Additionally, while much time was spent fine tuning the control settings of the test stand unavoidable oscillations in the pressure / strain data occurred which often led to the premature termination of tests. The need to attach expensive instrumentation in the form of either high temperature strain gauges or high temperature extensometers also limited the number of tests which could be performed and in the case of tests with the extensometer invoked an additional level of caution to the testing so as not to damage the instrument beyond repair by exposing it to a high number of violent ruptures.

In the future it is expected to improve upon these limitations by constructing a test stand that will utilize a hydraulic fluid as the pressurizing media. The use of a hydraulic pressurizing media immediately eliminates many of the challenges described above allowing for more controlled ruptures of the cladding tubes as well as the ability to replicate high strain rates. After correcting for compliance knowledge of the piston stroke length can also be used to infer inner volume changes in the cladding tube via a conservation of volume principle with an incompressible fluid. Separation of this volume change into diameter and length strains would require the use of some instrumentation. While a hydraulic system like the one shown in Figure 6-1 is somewhat more limited in terms of the maximum strain it can impose, the principal challenge with a hydraulic pressure test is the inherent temperature limitations of most hydraulic fluids. It is for this reason that a pneumatic system was chosen for the test stand described in this dissertation. However, several high temperature heat

transfer fluids or high-performance breaking fluids may allow for testing up to 330 °C provided the test durations are short. If rupture can be precluded slightly higher temperatures could be achieved although this introduces another undesirable limitation on the test stand. To truly unlock higher temperature testing the use of a liquid metal is required. Liquid metals often have the drawback of being either corrosive or embrittling (e.g. lead, gallium eutectics) or highly reactive to air/water environments (e.g. sodium - potassium eutectics). For testing in a laboratory setting where parts can easily be interchanged or replaced but exothermic reactions with air must be avoided it is likely preferable to use a liquid metal made from a gallium alloy. However, for implementation of the test stand in a radioactive, but inert hotcell environment for use in testing irradiated cladding tubes the use of the non-corrosive sodium alloys may be preferable.
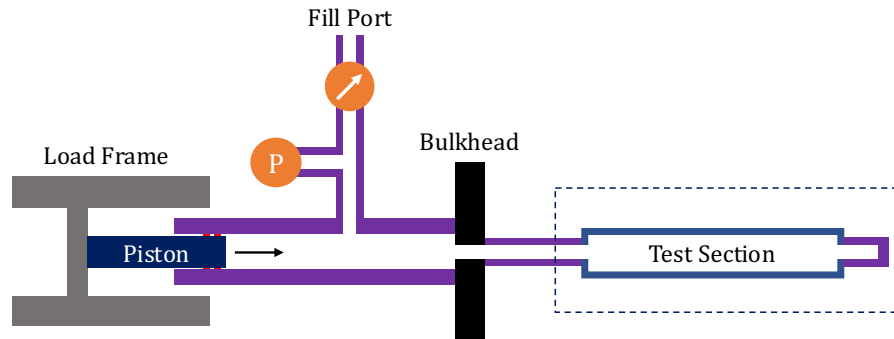

Figure 6-1 Schematic of a hydraulic strain-controlled pressure test.